Exploring the effect of doping on the piezoelectric properties of bismuth ferrite

Siddharth Joshi

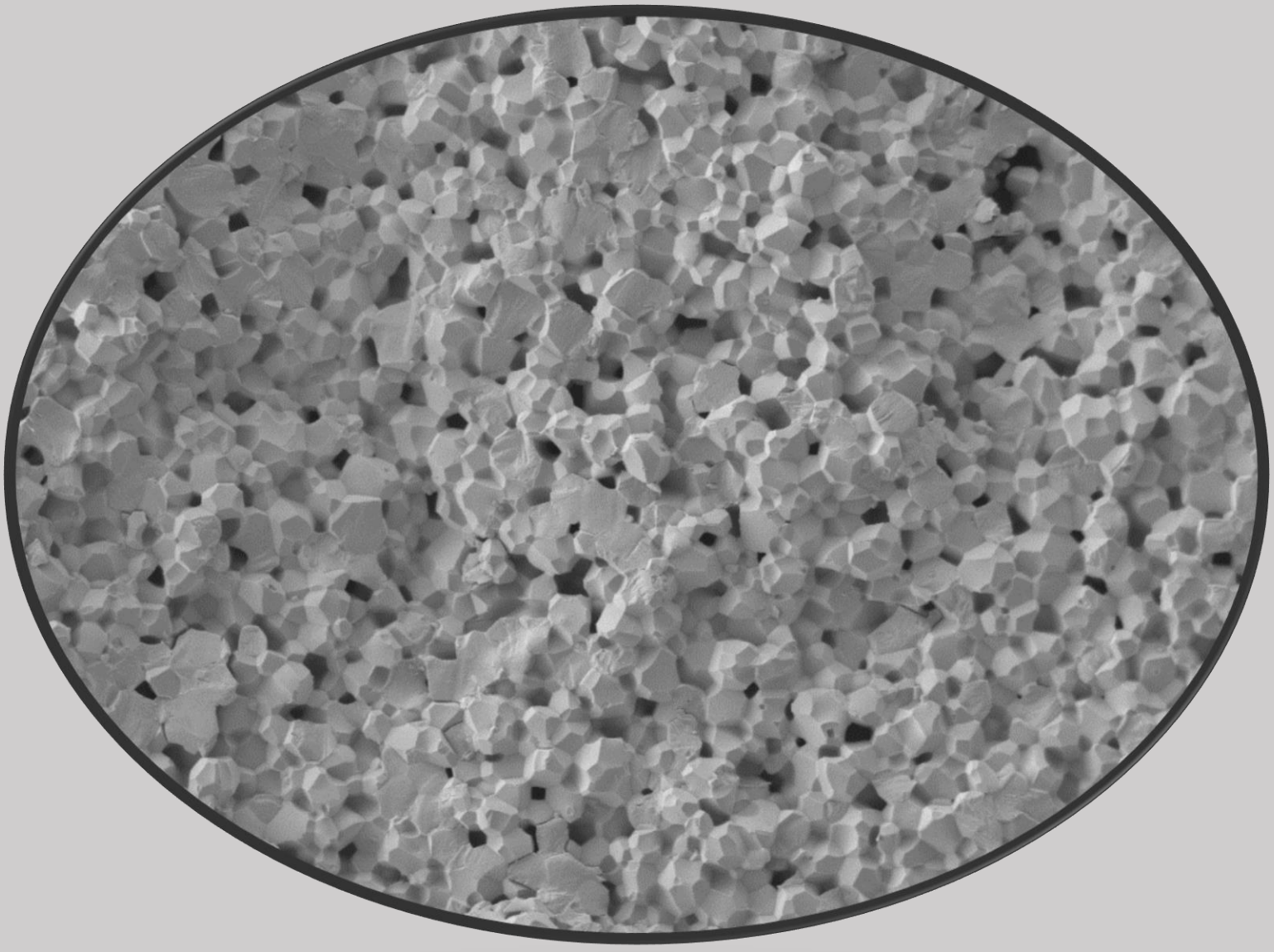

Exploring the effect of doping on the piezoelectric properties of bismuth ferrite

By

Siddharth Joshi

(5033233)

in partial fulfillment of the requirements for the degree of

Master of Science

in Aerospace Structures and Materials

at the Delft University of Technology,

to be defended publicly on Monday July 26, 2021 at 03:00 PM.

Thesis Supervisors:	Dr. T. Mahon	
	MSc A. Tuluk	
Thesis committee:	Prof. Dr. Sybrand van der Zwaag,	TU Delft
	Dr. R.M. Groves,	TU Delft
	Dr. M. Nijemeisland,	TU Delft

TU Delft

Acknowledgements

The completion of this thesis would not have been possible without the continuous support of my supervisors and peers.

First and foremost, I would like to thank my thesis supervisor, Dr. Tadhg Mahon for his guidance and for providing me with the opportunity to work on such an interesting and novel thesis topic. Tadhg has always been super accessible and very easy to approach. I sincerely thank him for his excellent and timely feedback on my thesis drafts. I would also like to thank my daily supervisor, Anton Tuluk for sharing his immense knowledge of piezoceramics and for making me a better experimental researcher. Working with Tadhg and Anton for the past year has been a genuine pleasure. I express my utmost gratitude to both of them for their expertise, valuable feedback, and their constant words of encouragement.

I would like to thank Dr. Sybrand van der Zwaag for providing me crucial feedback during our monthly meetings. His suggestions have improved the quality of my work and have made me a more competent researcher. I would also like to express my gratitude to Prof. Pim Groen for his work with the SMART materials research group at NovAM. His book, “An Introduction to Piezoceramic Materials and Components” has been crucial for developing my understanding of this project.

I express my gratitude to Kees Kwakernaak from the Department of Materials Science and Engineering (MSE) for the quick and timely provision of the high-resolution EDS data of our doped BFO samples. The data procured by him provided valuable insights into our system. I also want to thank Yasir Khan for his aid with the high-temperature measurements. Yasir provided great help for the last-minute high-temperature experiments. I want to thank Ir. Durga Mainali for his help in the labs with multiple types of equipment. Lastly, I want to thank Shanta Visser for answering any of my administrative queries and for setting up my monthly progress meetings with my supervisors.

I thank all the NovAM members who are a super awesome bunch. I enjoyed all the lunch and coffee break conversations; they helped me relax and were the highlight of my work-day. I am also grateful for the support of all my fellow Masters students. I especially want to thank Krishna, Nikhil, Anuj, Mark, and Caspar; for being the greatest of friends and for making the last year more wonderful and memorable for me. They have been my pillars of support and I consider myself very lucky to have made such genuine human connections.

Finally, I want to thank my parents (Sharat and Kalpana) and my sister (Shruti). Thank you for being so wonderful and for understanding and supporting my decisions. I love all of you and am grateful for your constant presence in my life.

Abstract

Piezoelectric materials are capable of converting mechanical energy into electrical energy and *vice versa*. These materials have been at the forefront of technological innovations ever since their emergence in the late 19th century. Piezoelectrics have found their niche in communication, automobile, aerospace, and several other industries relying on electromechanical systems. The excellent piezoelectric properties of materials like lead zirconium titanate (PZT) have made them a popular candidate in the production of actuators, sensors, and transducers. However, PZT was classified as a hazardous material in 2003 by the European Union due to the toxic nature of its lead oxide precursor. Efforts have been made by the scientific community to shift to more environmentally friendly, lead free, piezoelectric systems. Bismuth, sodium, and potassium have garnered much attention as substitutes for lead due to their non-toxic nature. Piezoceramics such as barium titanate (BT), bismuth ferrite (BFO), potassium sodium niobate (KNN), and potassium sodium lithium niobate (KNLN) have become increasingly popular.

Bismuth ferrite's (BFOs) high piezoelectric Curie temperature (825 °C) coupled with its lead-free nature makes it one of the more interesting PZT alternatives. However, the synthesis of phase pure BFO is difficult due to the presence of parasitic iron and bismuth-rich secondary phases. The electrical conductivity of BFO, which is considerably higher than that of PZT, is also an issue. The presence of a high electrical leakage current is generally attributed to the defects and oxygen vacancies in bismuth ferrite. Through doping, it is possible to control the density of these free moving charges and oxygen vacancies. In this thesis, we use the method of solid-state reaction synthesis with subsequent sintering for the preparation of doped BFO samples. This work aims to develop highly polarizable doped BFO systems with low leakage characteristics which could potentially be utilized for high-temperature sensing applications.

An enhancement in polarization was observed by doping BFO with trace amounts of cobalt. The incorporation of titanium into BFO led to the reduction of conductivity and caused an improvement in the leakage characteristics. A co-doped system of cobalt and titanium was further explored to combine the positive characteristics of both individual dopants. The result was a highly polarizable system (0.25-0.25 at% Co-Ti) with low conductivity and excellent leakage characteristics. A solid solution system of BFO with strontium titanate (STO) was also explored. The 30 at% STO system showed extremely large values of piezoelectric charge constant. The thesis was concluded by performing some high-temperature measurements on the 0.25-0.25 at% Co-Ti and 30 at% STO systems.

Table of contents

List of figures

List of tables

Chapter 1.

Introduction

1.1 Basics of piezoelectricity

The word piezoelectricity has its origins in Greek and roughly translates in English to 'Pressure electricity'. The piezoelectric phenomenon is thus the creation of an electrical charge from applied mechanical stress or *vice versa*. The direct piezoelectric effect involves the generation of a charge as a result of stressing the piezoelectric material while the inverse effect involves developing a strain in the piezoelectric material by exposing it to an appropriate electric field (1). Figure 1 shows the direct and inverse piezoelectric effects in working

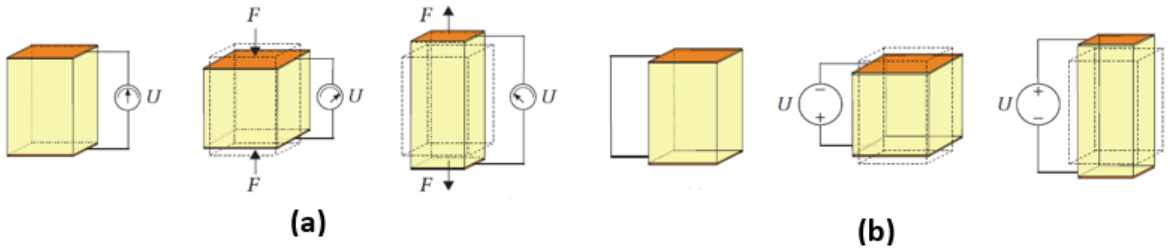

Figure 1 (a) Direct piezoelectric effect (b) Inverse piezoelectric effect (1)

1.1.1 The piezoelectric equations

The mathematical description of piezoelectricity in matrix notation can be described by the following equation:

$$\begin{pmatrix} \vec{S} \\ \vec{D} \end{pmatrix} = \begin{bmatrix} S^E & d^{tr} \\ d & \varepsilon^T \end{bmatrix} \begin{pmatrix} \vec{T} \\ \vec{E} \end{pmatrix} \quad (1)$$

Where S is the strain or the relative deformation vector, D is the electrical displacement vector, S^E is the material compliance at a constant electric field, d and d^{tr} represent the piezoelectric charge constant and its transpose, ε^T is the dielectric constant at constant stress, T is the applied stress vector and E is the electric field vector. The T and S vectors consist of six elements representing the shear and normal stress (or deformations) about the x, y, and z-axis. Meanwhile, the D and E matrix consists of three elements denoting the electrical properties (displacement and charge) along the three axes.

Piezoelectric materials are anisotropic, i.e., the electrical and mechanical components are not uniform in all directions (2) and are, in fact, determined by the crystallography of the system. The direction of deformations is generally expressed via an orthogonal coordinate system, which is demonstrated in Figure 2(a). By convention, the principal polarisation direction is denoted as direction 3 and the sheer axes around each of the three primary orthogonal directions also forming distinct directions. Piezoelectric materials can allow for four primary modes of operation (longitudinal, transverse, shear, and hydrostatic). For this study, only the longitudinal

mode of operation is important. However, a basic representation of the various modes of operations is presented in Figure 2(b).

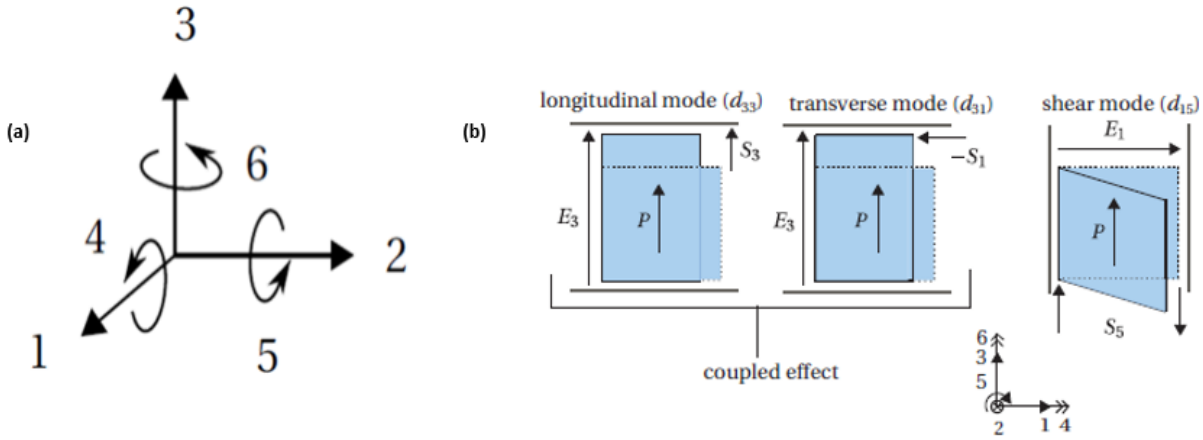

Figure 2 (a) Convention for axes and direction of deformations (b) Modes of operation for piezoelectric materials (1)

Considering the available variations of the different mechanical and electrical terms, as well as accounting for anisotropy, the uncondensed mathematical description of piezoelectricity in matrix notation is generally described by the equation given below:

$$\begin{pmatrix} S_1 \\ S_2 \\ S_3 \\ S_4 \\ S_5 \\ S_6 \\ D_1 \\ D_2 \\ D_3 \end{pmatrix} = \begin{bmatrix} S_{11}^E & S_{12}^E & S_{13}^E & S_{14}^E & S_{15}^E & S_{16}^E & d_{11} & d_{21} & d_{31} \\ S_{21}^E & S_{22}^E & S_{23}^E & S_{24}^E & S_{25}^E & S_{26}^E & d_{12} & d_{22} & d_{32} \\ S_{31}^E & S_{32}^E & S_{33}^E & S_{34}^E & S_{35}^E & S_{36}^E & d_{13} & d_{23} & d_{33} \\ S_{41}^E & S_{42}^E & S_{43}^E & S_{44}^E & S_{45}^E & S_{46}^E & d_{14} & d_{24} & d_{34} \\ S_{51}^E & S_{52}^E & S_{53}^E & S_{54}^E & S_{55}^E & S_{56}^E & d_{15} & d_{25} & d_{35} \\ S_{61}^E & S_{62}^E & S_{63}^E & S_{64}^E & S_{65}^E & S_{66}^E & d_{16} & d_{26} & d_{36} \\ d_{11} & d_{12} & d_{13} & d_{14} & d_{15} & d_{16} & \varepsilon_{11}^T & \varepsilon_{12}^T & \varepsilon_{13}^T \\ d_{21} & d_{22} & d_{23} & d_{24} & d_{25} & d_{26} & \varepsilon_{21}^T & \varepsilon_{22}^T & \varepsilon_{23}^T \\ d_{31} & d_{32} & d_{33} & d_{34} & d_{35} & d_{36} & \varepsilon_{31}^T & \varepsilon_{32}^T & \varepsilon_{33}^T \end{bmatrix} \begin{pmatrix} T_1 \\ T_2 \\ T_3 \\ T_4 \\ T_5 \\ T_6 \\ E_1 \\ E_2 \\ E_3 \end{pmatrix} \quad (2)$$

Fortunately, as several of these directions are crystallographically identical, this matrix can usually be reduced by condensing identical terms through the crystal symmetry.

1.1.2 Piezoelectric constants and dielectric parameters

The electromechanical interactions in a piezoelectric material are generally described by piezoelectric constants. This section will deal with these piezoelectric constants and some dielectric parameters.

Piezoelectric constants are generally expressed with subscripts that describe the state of the mechanical and electrical components. For example, for the piezoelectric charge constant d_{ij},

the first subscript (i) denotes the direction of the electrical component (the electric field or the electrical displacement) while the second subscript (j) denotes the direction of the mechanical component (the stress or strain)

1.1.2.1 Piezoelectric charge constant (d)

The piezoelectric charge constant can be defined as the polarization (P) induced as a result of the mechanical stress applied to the material in a short circuit condition (Zero electric field)

$$D_{E=0} = \vec{P} = d\vec{T} \tag{3}$$

The piezoelectric constant can also be described as the strain generated on the material due to an electrical field in an unloaded condition (Zero mechanical stress)

$$\overrightarrow{S_{T=0}} = d\vec{E} \tag{4}$$

The piezoelectric charge constant can be expressed in two units, derived from the direct piezoelectric effect (C/N) and the inverse piezoelectric effect (m/V). As evident from these equations, the strain induced on the material is dependent on the charge constant, making it a suitable indicator for how the material will behave in actuator based piezoelectric applications (1,3).

1.1.2.2 Piezoelectric voltage constant (g)

The piezoelectric voltage constant can mathematically be defined as the electric field per unit applied stress acting on the material (1,3). The relationship between the piezoelectric charge constant and the voltage constant is given below:

$$g = \frac{d}{\epsilon} \tag{5}$$

The piezoelectric voltage constant is a suitable indicator for sensing and its product with the charge constant (d*g) is a measure of energy harvesting applications.

1.1.2.3 Dielectric constant (ε_r)

The absolute permittivity (ε) of the material can be described as the dielectric displacement per unit electric field (described in equation 6). Permittivity is a measure of the amount of charge a piezoelectric material can store (1,3).

$$\varepsilon = \frac{\vec{D}}{\vec{E}} \tag{6}$$

The dielectric constant or relative permittivity (ε_r) is defined as the ratio of the absolute permittivity of the material to the permittivity of free space ($\varepsilon_o = 8.854 \times 10^{-12}$ F/m).

$$\varepsilon_r = \frac{\varepsilon}{\varepsilon_0} \tag{7}$$

1.1.2.4 Capacitance (C)

The capacitance is mathematically described as the ratio of the charge stored by the material to the potential difference between the two electrodes (1,4)

$$C = \frac{q}{\Delta V} \tag{8}$$

The capacitance for a piezoelectric material sandwiched between two electrodes can be described via the parallel plate capacitance, given by the equation below:

$$C = \frac{\varepsilon A}{T} \tag{9}$$

Where A is the area of the electrode and T is the thickness of the parallel plate configuration.

1.1.2.5 Loss tangent or Dielectric loss (tan δ)

The loss tangent or the dissipation factor is a measure of the dielectric losses of the material. These dielectric losses occur due to dielectric hysteresis, wherein a part of the electrical energy is dissipated away as heat (1).

The loss tangent is mathematically defined as the ratio between the imaginary part of the dielectric constant to the real part of the dielectric constant (as described in the equation below).

$$\mathrm{Tan}\,\delta = \frac{\varepsilon''}{\varepsilon'} \tag{10}$$

1.2 Bismuth ferrite (BFO)

The lead-free nature of BFO, along with its room temperature ferroelectric and magnetic behaviour, makes it one of the more interesting piezoelectric materials (5–7). Apart from its multiferroic nature, BFO possesses a high piezoelectric Curie temperature (825 °C) which makes it an outstanding candidate for high-temperature piezoelectric applications (8).

Apart from its usage for piezoelectric applications, BFO has been utilized in photovoltaic solar cells (9), metal-ferroelectric-insulator-silicon (MFIS) systems, field-effect transistors (10), and non-volatile memory devices (11). Despite its excellent properties; the presence of parasitic secondary phases, its large conductivity, and high coercive field limit the application of BFO.

1.2.1 Crystal structure

At room temperature, BFO exhibits a distorted rhombohedral perovskite (ABO_3) structure with a unit cell angle of 89.3° and a lattice parameter of 3.965 Å. The distorted structure is attributed to the buckling of oxygen octahedra to fit into the small unit cell (8). The hexagonal representation of the BFO perovskite structure is depicted in Figure 3 below,

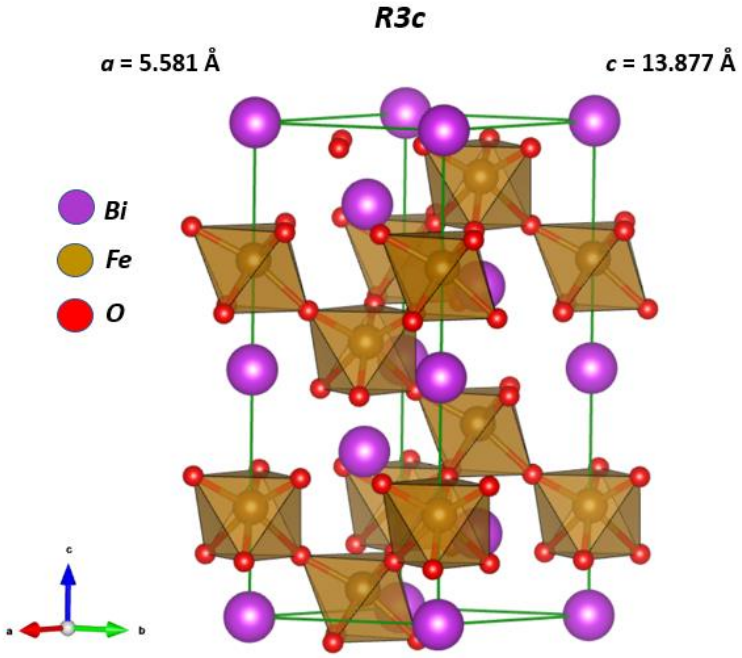

Figure 3 The perovskite structure of BFO

1.2.2 Phase diagram and existence of secondary phases

The secondary iron ($Bi_2Fe_4O_9$) and bismuth ($Bi_{25}FeO_{39}$) rich phases formed during the synthesis of BFO have always been a hindrance to the large-scale operation of BFO. The bismuth-rich secondary phase easily nucleates at grain boundaries to cause degradation of BFOs functional properties.

Figure 4 (a) shows the phase diagram for the Bi_2O_3-Fe_2O_3 system. Three distinct phases of $BiFeO_3$ can be identified, these are the rhombohedral or α phase, the orthorhombic or β phase, and a cubic or γ phase. The rhombohedral to orthorhombic transition occurs at 825 °C. At temperatures higher than 925 °C, the orthorhombic phase transitions to the cubic γ phase (12). The rhombohedral to orthorhombic transition occurring at 825 °C is further confirmed by high-temperature x-ray studies, as shown in Figure 4 (b).

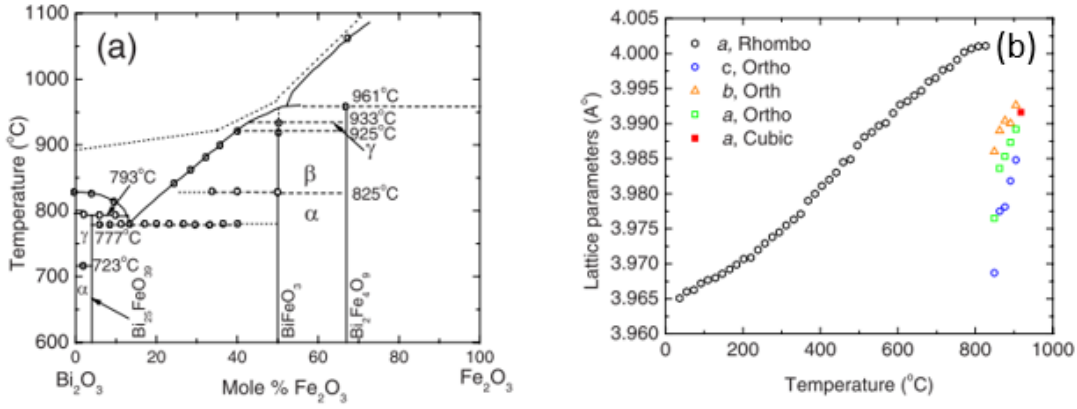

Figure 4 (a) BFO phase diagram and (b) Variation of lattice parameter with temperature (reproduced from (12))

Figure 5 shows the formation of different phases of BFO with rising temperatures. The perovskite ($BiFeO_3$) and the bismuth-rich sillenite ($Bi_{25}FeO_{39}$) phase are the first ones to be formed at a temperature around 600 °C. Further increase in temperature leads to a decrease in the sillenite phase, with it disappearing entirely at 750-800 °C to form a prominent single-phase perovskite structure. At temperatures higher than 900 °C the decomposition of the perovskite phase into the iron-rich mullite phase ($Bi_2Fe_4O_9$) occurs (13). The metastability of BFO has also been linked to its low Goldschmidt tolerance factor (t=0.88). Efforts to further stabilize BFO has led to it being incorporating with other perovskites to form a solid solution (8).

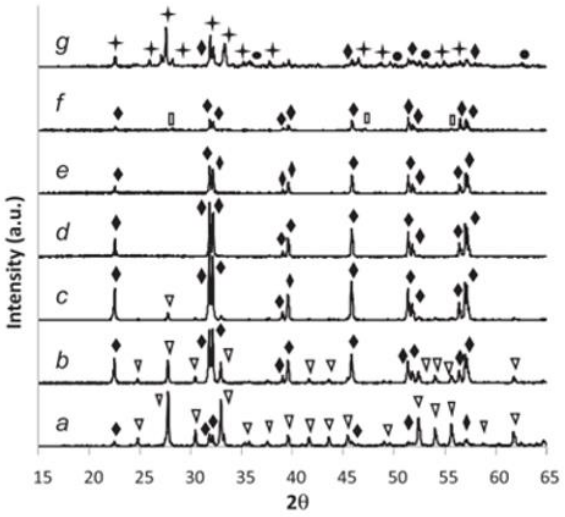

(a) 600 °C, (b) 650 °C, (c) 700 °C, (d) 750 °C, (e) 800 °C, (f) 900 °C and (g) 1000 °C. (♦) $BiFeO_3$, (▽) $Bi_{25}FeO_{39}$, (□) $Bi_2Fe_4O_9$, (+) Bi_2O_3 and (●) Fe_2O_3.

Figure 5 BFO phase formation (13)

A basic understanding of the reaction kinetics for the formation of BFO is also important as it helps to determine how the perovskite formation occurs. The reaction kinetics are controlled by the diffusion of bismuth ions (Bi^{3+}) into iron oxide and not vice-versa. The higher magnitude of tracer diffusion coefficient of Bi^{3+} ions (6.8×10^{-20} m^2/s at 700 °C) as compared to Fe^{3+} (2.8×10^{-25} m^2/s at 700 °C)) corroborates the previous statement (14). This is also consistent with common microstructural details in BFO, wherein, small and dark iron-rich regions can be seen inside BFO grains with the bismuth-rich phase occurring at the grain boundaries.

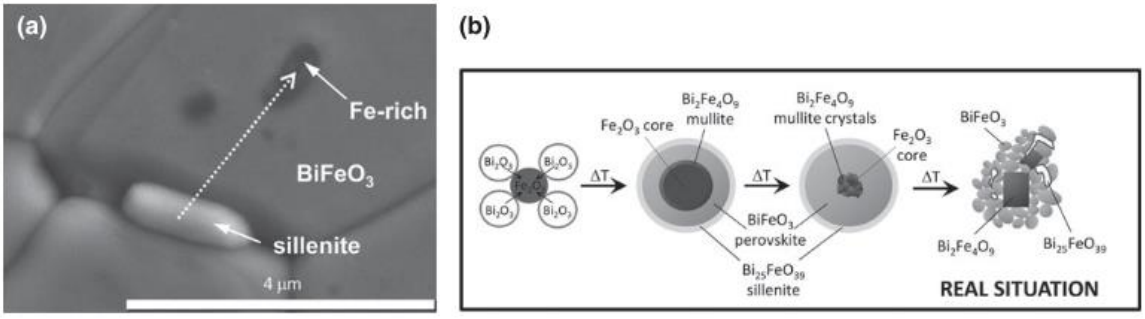

Figure 6 (a) Characteristic SEM image of BFO, showing the iron and bismuth rich phases (b) Reaction pathways for synthesis of BFO (13,14)

The commonly accepted reaction pathway for the formation of BFO is displayed in Figure 6(b). First, the formation of the sillenite phase ($Bi_{25}FeO_{39}$) takes place on the outer surface, followed by the development of perovskite ($BiFeO_3$) deeper inside. Further deeper the mullite phase ($Bi_2Fe_4O_9$) forms the closest to the iron oxide core. At the end of the reaction apart from the perovskite, some sillenite and mullite are also left in the BFO sample (13).

1.2.3 Problem of electrical conductivity

For the determination of the conductivity of a ceramic-like BFO, the contribution from the electrons, ions, defects, potential dopants, and grain boundaries have to be considered (15). The electronic conduction is based upon the thermal activation of electrons from the valence band to the conduction band. The ionic conduction takes into account the contribution of the hopping of ions within the lattice. The defects created due to doping or during the synthesis of the ceramic can also contribute to conductivity.

Multiple studies have reported the synthesis of BFO with large conductivity values. The large conductivity of BFO has been attributed to oxygen vacancies, the presence of secondary phases, and the reduction of Fe^{3+} into Fe^{2+} ions (14). Varying conduction mechanisms like Ohmic conduction, space-charge-limited bulk conduction (SCLC), Poole-Frankel emission, and Schottky emission have been attributed to BFO (16). The mathematical expressions for these four mechanisms are represented by the equations given below:

$$J_{ohmic} = \frac{nq\mu V}{d} = nq\mu E \tag{11}$$

$$J_{SCLC} = \frac{9\mu \in_0 \in_r E^2}{8d} \tag{12}$$

$$J_{PF} = BE exp\left(- \frac{E_1 - \sqrt{\frac{q^3 E}{\pi \epsilon_0}} \in}{k_b T} \right) \tag{13}$$

$$J_{schottky} = AT^2 exp\left(- \frac{\varphi - \sqrt{\frac{q^3 E}{4\pi \epsilon_0}} \in}{k_b T} \right) \tag{14}$$

Where n is charge carrier concentration, q is the charge, V is applied potential, d is film thickness, E is applied electrical field, μ is charge carrier mobility, ε_r is relative permittivity, ε_0 is the permittivity of free space, A is the Richardson constant, k_b is the Boltzmann constant, T is the thermodynamic temperature, φ is Schottky barrier height, ε is the dynamic dielectric constant, E_i is the ionization energy of trapped carriers and B is a general constant.

In SCLC, the current density is dependent on the charges injected into the system. SCLC becomes the dominant mechanism if the density of the charge carriers injected into the system becomes greater than the charge carriers generated within the volume of the material (17). In ohmic conduction, the current density solely depends on the intrinsic charge carriers of the materials. There is no contribution of the charges injected into the system from the electrodes. It is evident from equations 11 and 12 that both ohmic and SCLC can be characterized by a linear log(J) vs log(E) relationship. The difference is in the slopes, with Ohmic characterized by slopes less than 1.5 while SCLC has slopes in the 1.5-3 range (16).

A large variation in the magnitude of the dielectric permittivity of BFO has been reported in the literature (18,19). Dielectric relaxation mechanisms can be used to ascertain the frequency and temperature-dependent variation of permittivity. Dielectric constants with magnitudes as high as 10^4 have been recorded at low frequencies and high temperatures (8). This large dielectric constant has been attributed to the impact of electrical conductivity through Maxwell-Wagner or hopping relaxation (14).

The Maxwell-Wagner mechanism accounts for the accumulation of charges at the interface of a two-material system. This accumulation of charges is dependent on the difference in the relaxation time at the interface. Mathematically, the relaxation time is the ratio of the dielectric constant to the electrical conductivity. It is indicative of the time required for the charge carriers to spread across said interface (20). The dielectric response can also be attributed to the hopping relaxation mechanism, which accounts for the movement of charge carriers across the system. In essence, the hopping system will behave as a dc conductor however carrier interactions, hopping probabilities, and transitions make the mechanism more complex (21).

Selecting the dominant relaxation mechanism is pretty complicated and varies throughout the literature (14,22,23). The choice of the dispersion mechanism is often speculative and depends on the frequency range in which the measurements are done. The dispersion mechanism is assigned to just a part of the spectrum, and the choice for the dominant mechanism may change at higher frequency ranges.

1.2.4 Problems associated with poling

As previously mentioned, BFO has a naturally high coercive field for ferroelectric domain switching (8,14,24) which presents a major problem for poling BFO ceramics. As a result of this, most of the PE loops reported for BFO in the literature are not saturated. The defects produced in the system during synthesis also influence the switching behavior exhibited by BFO. Different processing conditions will induce a different number of defects, which will change the nature of the loop (pinched or unpinched), the breakdown voltage, and the polarization values (see Figure 7).

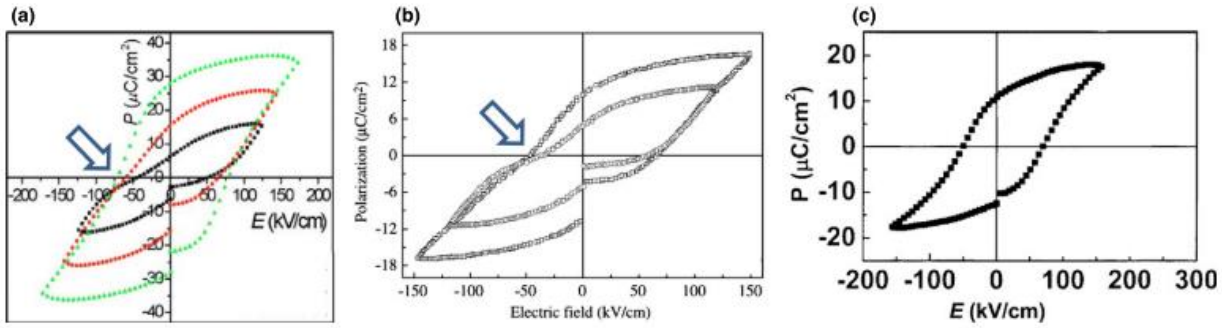

Figure 7 shows three sets of PE loops for three different processing conditions (a) for sol-gel processing, (b) for rapid liquid phase sintering, and (c) for solid-state reaction along with quenching (14)

The influence of defect geometry on the PE loops is corroborated by Figure 8 where different loops are generated by variation of quenching temperature and cooling rates. Reduction of cooling rates leads to pinching of the loops which can be attributed to reordering of defects due to slow cooling of the samples. These defects induced during synthesis may cause irreversible changes in the polarization, as evident from the unique PE loop for the non-quenched sample.

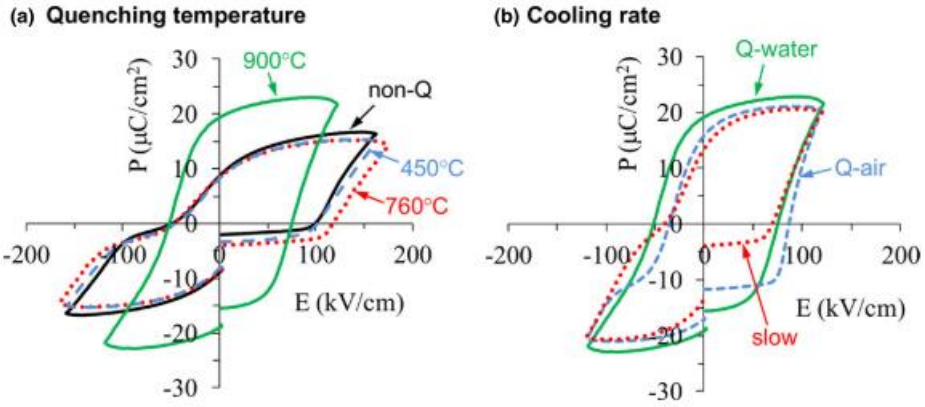

Figure 8 shows BFO PE loops for (a) different quenching temperatures, (b) different cooling rates (14)

1.3 Doping of BFO

Doping involves replacing the lattice sites with a dopant to enhance a particular characteristic of the parent perovskites (ABO_3). Doping of perovskites can involve replacing the lattice sites with ions of similar charge, which is known as isolvalent doping. Isovalent doping of Ba^{2+} in barium titanate by Pb^{2+} leads to a considerable increase in the Curie temperature (and by association, the operating temperature) of the system (1). Sometimes doping is done to account for charge compensation (25). The A and B site ions can also be replaced by ions of smaller (Acceptor doping) and larger (Donor doping) valence. As a result of doping and charge compensation, cationic or anionic vacancies can be created which can further influence the properties of the perovskite system

A site substitution of Bi^{3+} in BFO has been shown to predominantly affect the magnetic properties of the system (26–28). These changes in the magnetic properties are caused by the buckling of the Fe-O-Fe bond angle (29). In some A-site doping cases (samarium), doping with rare earth elements has shown an increase in the piezoelectric charge constant. This has been attributed to the presence of a triclinic-orthorhombic morphotropic phase boundary (30).

B site substitution of Fe^{3+} in BFO strongly influences the magnetic and electrical properties of the system (31,32). B-site donor doping with titanium reduces the leakage current of BFO through a reduction of Fe^{3+} to Fe^{2+} ions and a corresponding overall decrease in the number of oxygen vacancies (16,33,34).

To get the synergistic effects of two types of dopants, co-doping systems can be explored. For example, the co-doped BFO system of lanthanum and niobium shows enhanced magnetization and reduced dielectric losses (35) While the lanthanum and neodymium co-doped system improves the magnetization and the ferroelectric polarization (36,37).

In this section we will present an overview of the literature on BFO doping, focusing on the dopants that are to be used in this thesis work. We will discuss these dopants with respect to their effects on microstructure, vacancy formation, leakage characteristics, polarization, and conductivity. The focus will be on cobalt, titanium, and bismuth ferrite- strontium titanate solid solution.

1.3.1 Cobalt doping

The effects of cobalt doping on BFO remains a source of some disagreement throughout the literature. Some studies show an increase in conductivity with cobalt doping while other studies show cobalt doping having an opposite effect (38–40). It is important to note that different results are observed (and expected) for thin films and bulk cobalt-doped BFO materials. For this study, the emphasis is solely on bulk systems. If results for thin-films are discussed, then it is explicitly stated in the text.

As evident from Figure 9(a-b), the addition of cobalt in BFO causes a reduction in the particle size due to partial substitution of Fe by Co on the B-site. The reduction of the particle size is related to the shrinkage of the unit cell as the ionic radii of Co^{3+} (61 pm) is slightly less than Fe^{3+} (64.5 pm) (41). The X-ray photoelectron spectroscopy of the cobalt (Co_3O_4 parent oxide) doped samples shown in Figure 9(c) shows that Co^{3+} ions are present in larger concentrations than Co^{2+} ions. 5 at% doping (Sol-gel synthesized system) of BFO with cobalt, $BiFe_{0.95}Co_{0.05}O_3$, shows an increase in the number of oxygen vacancies (42). Cobalt dopant acts as an acceptor which is responsible for the increased amount of oxygen vacancies. The XPS oxygen spectra presented in Figure 9(d-e), show an increase in the number of oxygen vacancies (O_v) and reduction in the oxygen ions in the lattice (O_L) due to cobalt substitution.

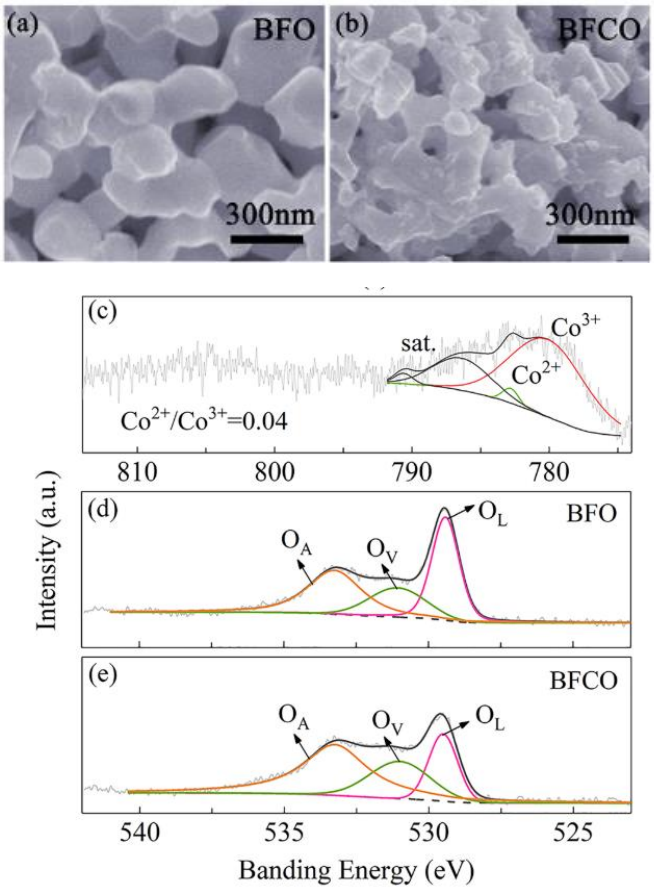

Figure 9 (a) SEM images for BFO (b) SEM image for sol-gel synthesized $BiFe_{0.95}Co_{0.05}$ (c) XPS cobalt spectra (d) XPS oxygen spectra in BFO (e) XPS oxygen spectra in $BiFe_{0.95}Co_{0.05}O_3$ (43)

Studies conducted on cobalt-doped BFO thin films show that cobalt doping at large doses (>15 at%) causes an increase in leakage current while doping at lower concentrations (<5 at%) decreases the leakage current (38). $BiFe_{0.90}Co_{0.10}O_3$ doped films show an extreme enhancement of conductance (up to 200 times) which is accompanied by a reduction in the bandgap. $BiFe_{0.95}Co_{0.05}O_3$ thin films showed a reduction in leakage current at high electric field regions. The substitution of cobalt also helped in the reduction of the coercive field while keeping the magnitude of remnant polarization the same (40). Figure 10 shows the leakage current reduction, the coercive field, and remnant polarization variation.

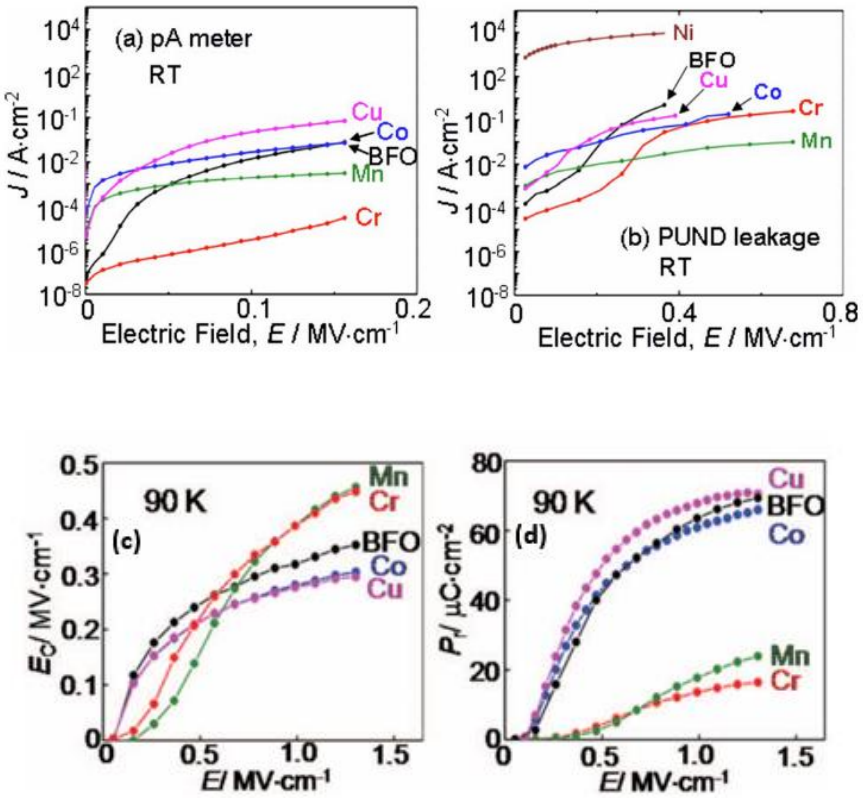

Figure 10 (a) Leakage characteristics at low electric field region (<0.2 MV/cm) (b) Leakage characteristics at high electric field region (>0.2 MV/cm) (c) Variation of the coercive field at 90K (d) Variation of remnant polarization at 90K (40)

BFO samples doped with small amounts of cobalt (0.25,0.5,1 and 1.5 at%) show a pinched P-E loop (Figure 11 (a)), with the pinched nature of the loops becoming more prominent with higher cobalt loadings (39). The pinched nature is attributed to domain wall pinning caused by charged defects (44). From Figure 11(b), the fields at which domain pinning occurs also increase with increasing cobalt concentration, with the 1.5 at% Co-doped samples showing switching at fields as high as 150 kV/cm.

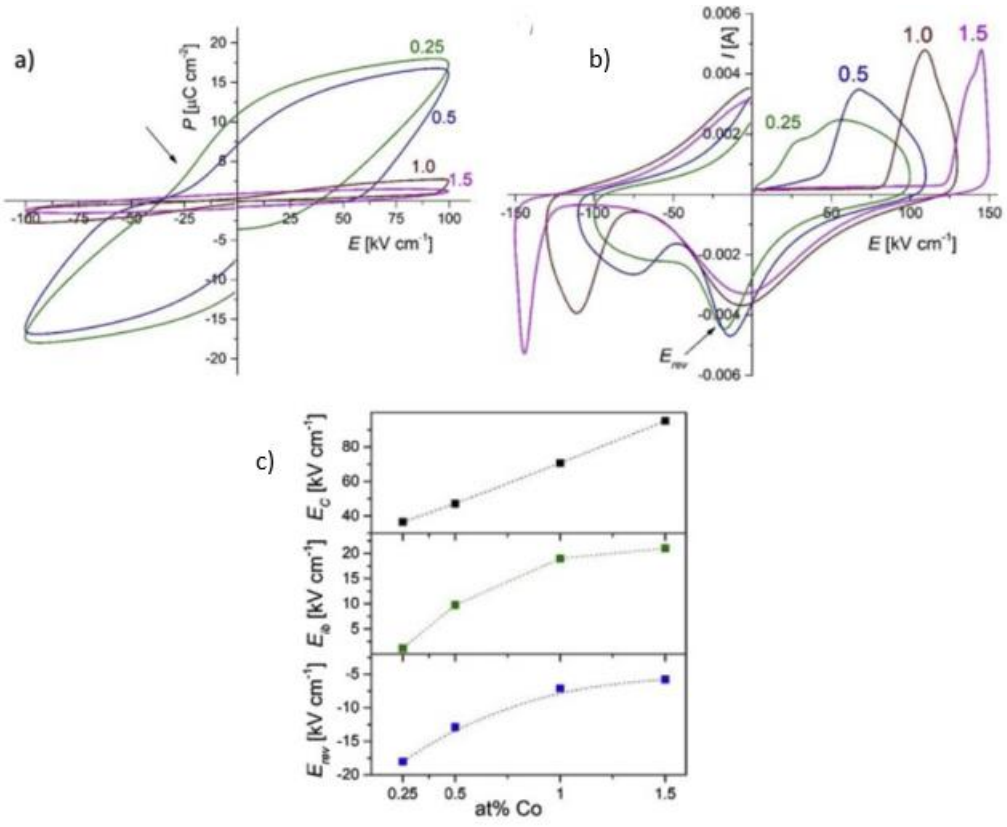

Figure 11 (a) PE loops for cobalt doped BFO samples (b) I-E loops for cobalt doped BFO samples (c) Variation of coercive field (Ec), internal bias(Eib), and reverse electric field (Erev) (39)

Figure 11(c) shows the variation of the coercive field (E_c), internal bias (E_{ib}), and reverse electric field (E_{rev}) with increasing cobalt concentration. The internal bias field, E_{ib}, represents the asymmetrical displacement of the P-E loops from the origin due to the defects in the system (45). The reverse electric field, E_{rev}, represents the field at which domain switching (I-E peak for the negative polarity, represented by an arrow in Figure 11(b)) occurs when the poling field is reversed. From Figure 11(c), there is a clear increase in all the three aforementioned parameters with increasing cobalt concentration. The enhanced pinching of PE loops indicates a hardening effect caused by the cobalt dopant.

Figure 12(a-c) shows the variation of permittivity (real and imaginary parts) and real AC conductivity with frequency. The permittivity (both real and imaginary parts) decreases with increasing frequency. The imaginary part of permittivity is very high at low frequencies for all cobalt loadings, indicating an electrical conduction-dominated response at lower frequencies. The dispersion of real and imaginary permittivity at lower frequencies indicates that the electrical conduction dissipates energy as well as causes some dielectric polarization. The AC conductivity is also shown to increase with doping concentration, further confirming the hardening effect of the cobalt dopant. It can thus be hypothesized that cobalt, acting as an acceptor dopant, gets substituted on the B sites thereby promoting the formation of oxygen vacancies and Fe^{4+} defects (p-type defects).

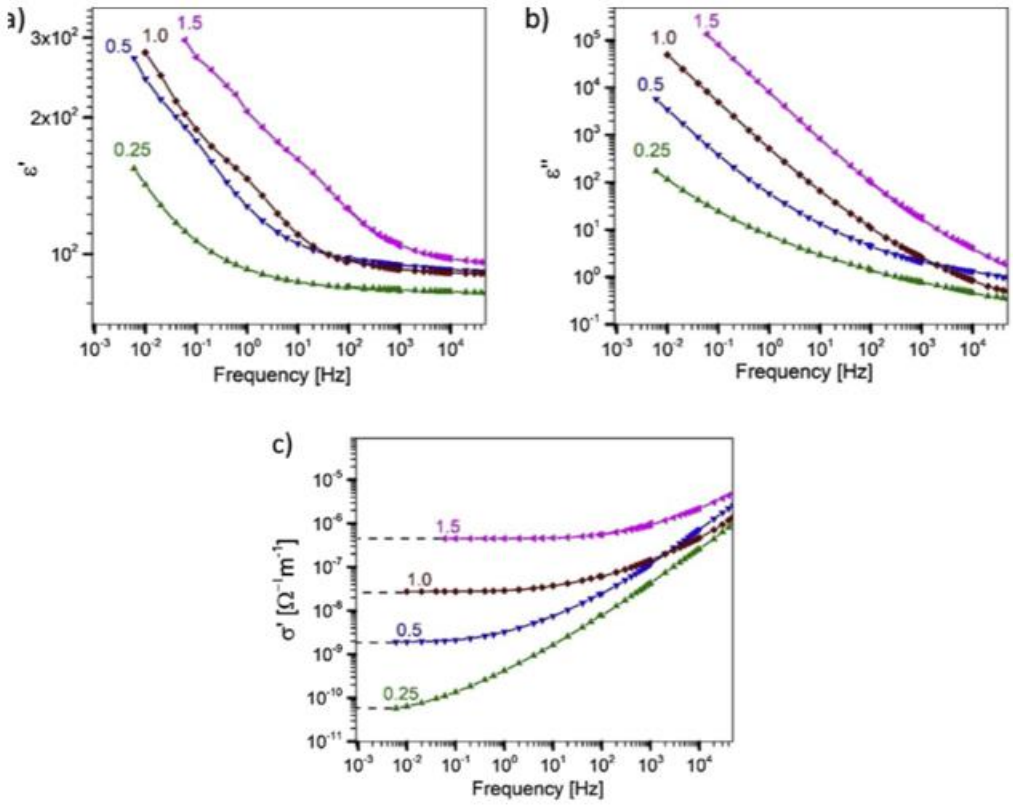

Figure 12 Variation of (a) real part of permittivity (b) Imaginary part of permittivity (c) real part of AC conductivity, with changing frequency (39)

1.3.2 Titanium doping

The ease of formation of oxygen vacancies in BFO due to factors such as bismuth evaporation means that a large portion of the most attractive dopants for reducing the leakage of the system are those with access to highly positive valence states such as titanium. Studies on titanium doping of BFO do indeed show a significant change in the leakage characteristics (46,47). Thin titanium doped BFO films (BFTO) developed via sol-gel (16,33,34) and pulsed laser deposition (17) techniques show greatly reduced leakage current due to B site substitution of Ti^{4+} and the consequent reduction of Fe^{3+} to Fe^{2+} ions as well as the reduction in the number of oxygen vacancies (16). Bulk studies of titanium doped BFO exhibit similar changes in the leakage characteristics (46,47).

The reduction in grain size induced by titanium doping can be seen in Figure 13. The reduction in grain growth is often attributed to the reduced oxygen vacancies as a result of titanium doping. The lower concentration of oxygen vacancies implies an overall slower oxygen ion motion which leads to lower grain growth (46).

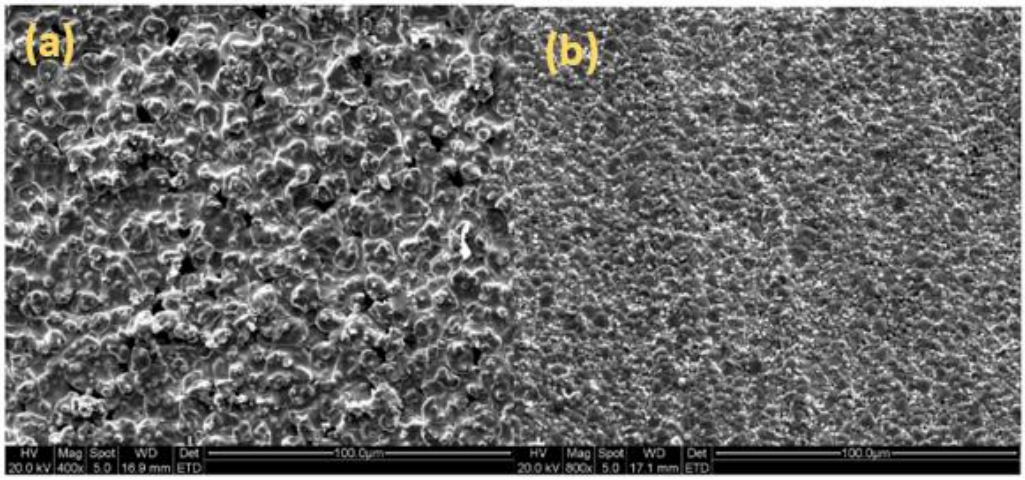

Figure 13 SEM micrographs of (a) phase pure BFO (b) 10 at% doped Ti BFO (46)

High-resolution TEM and EDS studies show the distribution of titanium in $BiFe_{0.95}Ti_{0.05}O_3$ samples. Rather than being homogeneously distributed, titanium concentration was found to be 50 % higher at the intersection of three nanograins (triple junction point), 10-25 % higher at the nanograin boundaries, and 10-25 % lower inside the nanograins (47). The reduction in grain size along with the inhibition of grain growth with titanium doping suggests that Ti ions segregate at the grain boundaries thereby further impeding grain growth on top of the impact of oxygen ion vacancy reduction. Figure 14 shows a visualization of this along with the actual distribution of titanium at three points (grain interior, triple point, and grain intersection)

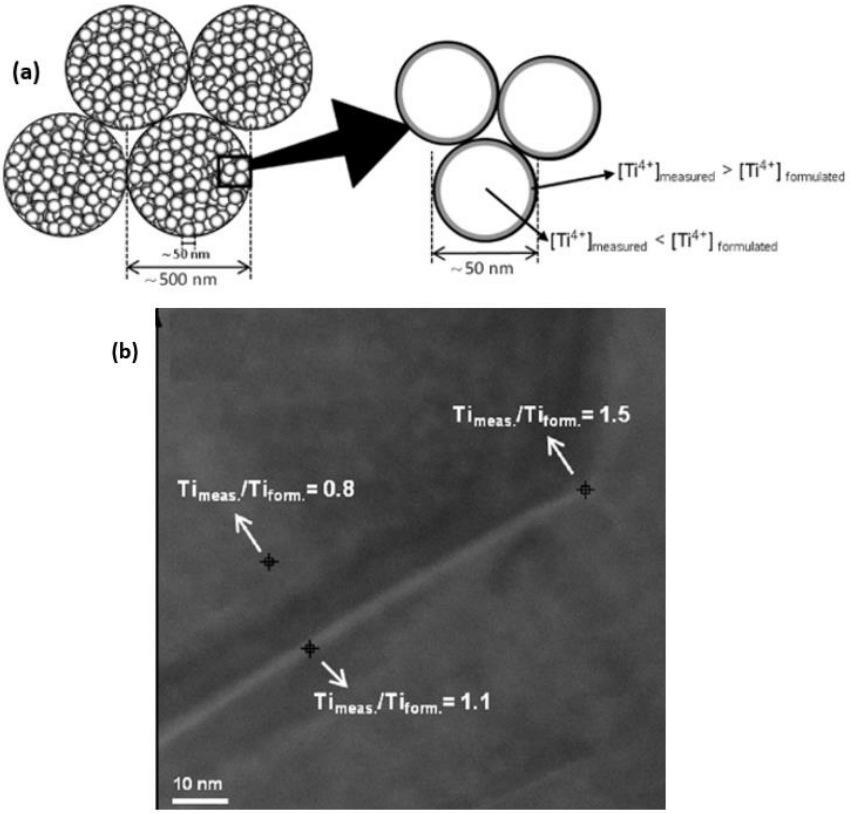

Figure 14 (a) Visualization of Ti distribution in $BiFe_{0.95}Ti_{0.05}O_3$ samples (b) Actual titanium concentration at different points in the $BiFe_{0.95}Ti_{0.05}O_3$ samples (47)

The density of BFTO samples also does not seem to follow any particular trend with increasing titanium doping concentration. From Figure 15 given below, it can be seen that titanium samples (sintered using similar sintering profiles) show an increasing relative density up to 10 at% (x=0.1) but then show a decreasing trend. This could be attributed to pore formations at higher doping which could lead to lower relative densities (46).

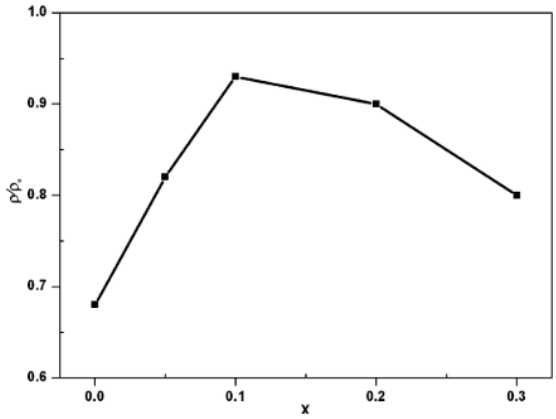

Figure 15 Variation of the density of BFTO samples with increasing titanium concentration (x) (46).

Figure 16 shows the characteristic PE loops for titanium doped bulk BFO. The hysteresis loops for titanium doped samples do not show saturation and the hysteresis loop does not even open at room and sub-zero temperatures. There is also a development of a non-appreciable remnant polarization (0.081 µC/cm2) and maximum polarization (0.658 µC/cm2) (48). This behavior is not replicated in BFTO thin films, wherein doping with 5 to 10% titanium has been shown to significantly enhance the polarization as well as decrease the leakage characteristics (34).

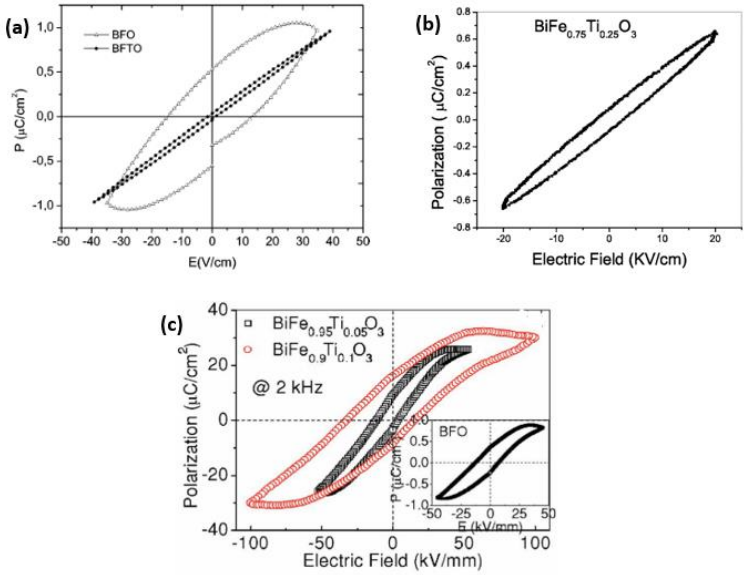

Figure 16 P-E loops for (a) BFO and $BiFe_{0.95}Ti_{0.05}O_3$ (b) $BiFe_{0.75}Ti_{0.25}O_3$ and (c) BFTO thin films (34,47,48)

The high resistivity of titanium doped $BiFe_{0.95}Ti_{0.05}O_3$ samples can be attributed to the non-homogenous distribution of titanium. As explained previously, there is a larger distribution of titanium at the grain boundaries and triple junction points. These titanium-rich regions can act as resistive and insulating layers (47)

A study of dielectric constant and dielectric losses for $BiFe_{0.75}Ti_{0.25}O_3$ with varying frequencies and temperature showed that the addition of titanium increased the dielectric constant and decreased the dielectric losses (48). A clear peak or anomaly can be observed from Figure 17 at around 350 °C. Since BFOs Neel temperature (369 °C) (49) is near where this anomaly occurs, it can be hypothesized that the reduced magnetic order affects the electrical characteristics.

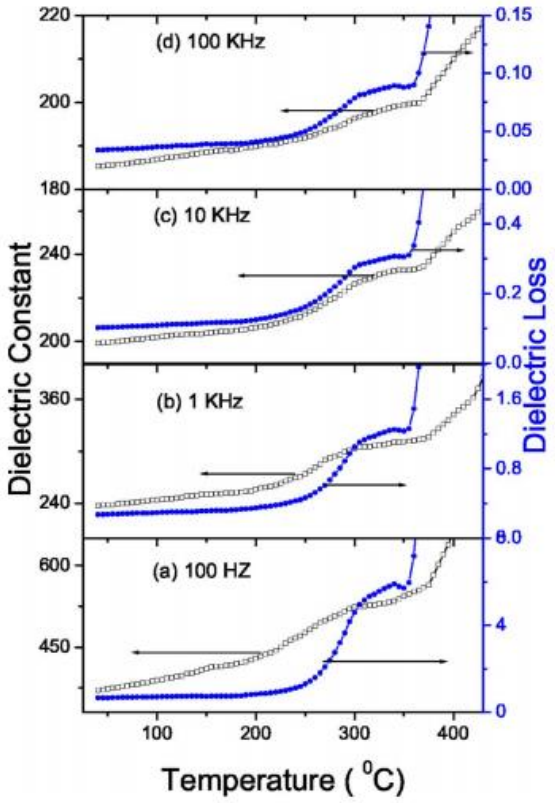

Figure 17 Variation of dielectric constant and loss tangent for $BiFe_{0.75}Ti_{0.25}O_3$ with varying temperatures at a range of frequencies (a-100Hz, b-1Khz, c-10khz, and d-100Khz) (48)

1.3.3 Cobalt-Titanium doping

Even though titanium doping for bulk BFO ceramics has not shown much promise in terms of achieving high polarization, from the previous section, it is quite certain that titanium doping is very successful in reducing the leakage current. BFO co-doped systems having titanium as one of their constituents have shown significantly better leakage characteristics and dielectric losses. Figure 18(a-b) shows one such system wherein Eu-Ti co-doped BFO exhibits much less leaky and lossy characteristics than the parent system

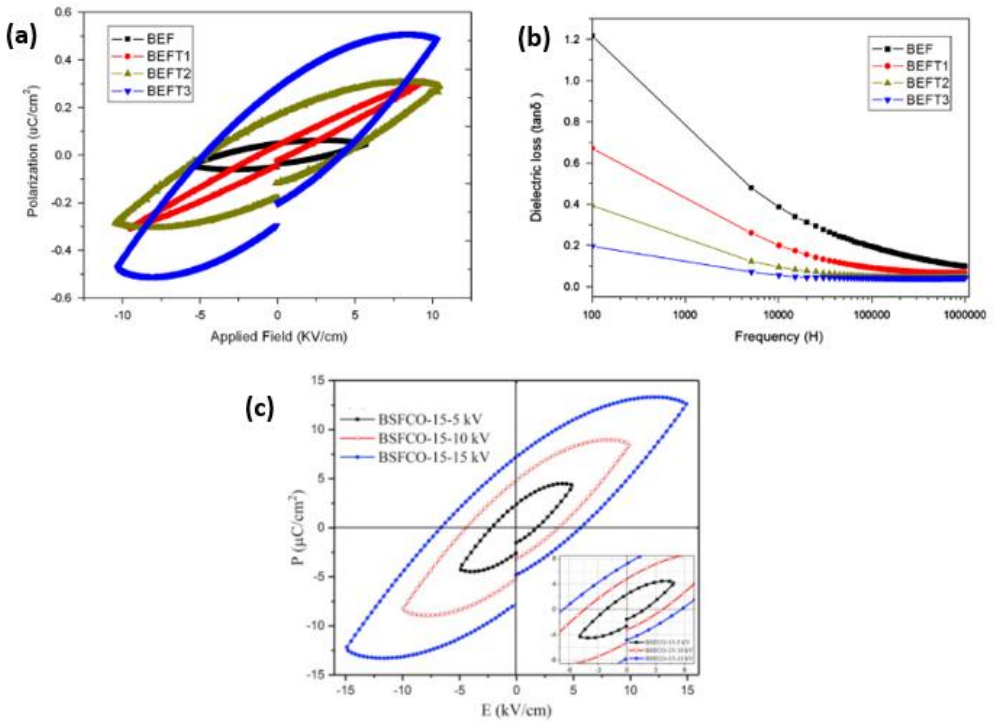

Figure 18 (a) P-E loops and (b) Tan delta, for Eu-Ti co-doped BFO system (c) P-E loops for Sm-Co systems (50,51)

As mentioned previously (Chapter 1.3.1 Cobalt doping), doping with cobalt has shown to enhance the polarization in BFO. As evident from Figure 18(c), BFO co-doped systems with cobalt as one of their constituents shows the increased maximum and remnant polarization. Samarium-cobalt co-doped BFO along with showing enhanced polarization exhibits an increase in conductivity (52). The increase in conductivity can be ascribed to the substitution of Sm^{3+} at the A site and Co^{2+} at the B site.

From this section, it is apparent that the individual effect of titanium and cobalt dopants on BFO has produced desirable results in terms of achieving low leakage and enhanced polarization respectively. These results necessitate further exploration of a co-doped cobalt-titanium BFO system.

1.4 Bismuth ferrite- Strontium titanate (BFO-STO) system

The perovskite strontium titanate (STO) is an important material. The uniqueness of STO is in its high piezoelectric response at sub-zero temperatures. STO exhibits high piezoelectric properties at temperatures as low as 50 kelvin, which makes it an ideal candidate for ultralow temperature piezo systems (53). STO has a Goldschmidt tolerance factor (t) value of 1, making it a highly ideal perovskite (54). An extensive amount of research has been dedicated to doping of STO, to further improve its properties and make it more useful at higher temperatures (54,55).

Introducing other perovskites into BFO has recently garnered attention due to the incorporation of a morphotropic phase boundary (MPB). The enhancement of piezoelectric properties due to the presence of a MPB separating two polar phases was reported as early as 1958, where, PZT ceramics with high coupling coefficients were synthesized by inducing a tetragonal-rhombohedral phase boundary (56). This increase in piezoelectric properties by incorporation

of a polar MPB is attributed to the polarization rotation mechanism. The presence of a MPB causes a reduction or tilting of the spontaneous polarization vector (P_s), leading to an increase in anisotropy and a subsequent flattening of the domain potential (57). This leads to polarization rotation along easier paths which allows poling of the ceramic to higher levels of polarization.

MPBs can also separate regions containing polar and non-polar phases. An enhancement in properties is also observed here, however, this is not due to polarization rotation but is attributed to a polarization extension mechanism. The extension mechanism is also related to the flattening of the domain potential to open up pathways for easy polarization. However, it is a temperature dependant enhancement mechanism (58). Some common polar- non-polar MPB based BFO systems include BFO-STO (59–61), BFO-CTO (62–64), BFO-KBT (65).

An example of this MPB induced piezoelectric enhancement can be seen in Figure 19, which shows the variation in the room temperature piezoelectric properties of xBFO-(1-x)STO system. It shows an increase in d_{33} with increasing BFO content up to x=0.625. This enhancement is attributed to the presence of a rhombohedral-pseudo cubic MPB at that particular BFO concentration (61).

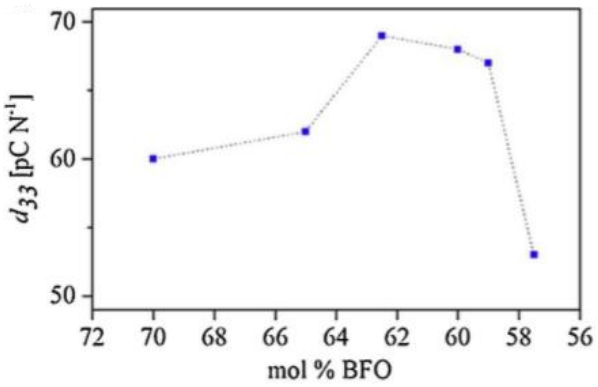

Figure 19 Variation of room temperature d33 for (x)BFO-(1-x)STO for different concentrations (61)

With increasing concentration of STO, the BFO-STO transitions from a distorted rhombohedral structure with space group R3c (characteristic of BFO) to a cubic Pm-3m structure (characteristic of STO) (59). As evident from Figure 20, the twin peaks in BFO reduce in intensity with increasing STO concentration, finally forming single peaks at x=0.8 (80 at% STO). This point denotes the transition of the solid-solution crystal structure to a dominant cubic phase. There is also a shift in the peaks to higher angles which denotes a reduction in the lattice constant. This is expected, as more and more Ti^{4+} is substituted for Fe^{3+} in the B-site leading to unit cell contraction

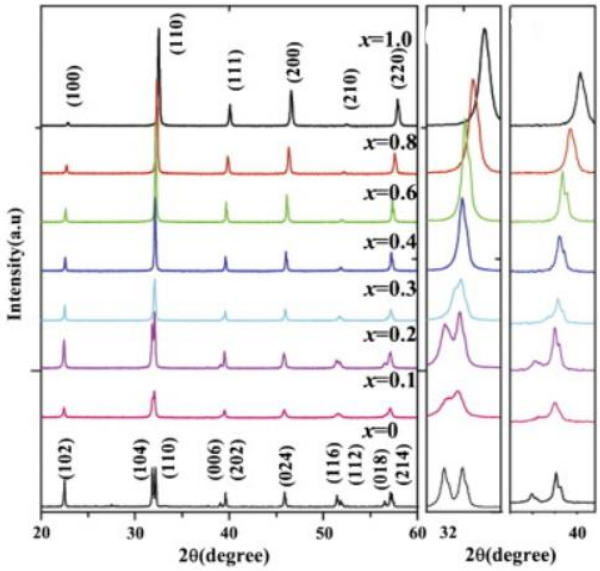

Figure 20 XRD patterns for (1-x)BFO-xSTO for varying x value (59)

Figure 21 (a-e) shows the P-E loops for the (1-x)BFO-xSTO system for x=0 to 0.6. Increasing the concentration of STO, leads to improved polarization, with x=0.6 having much better ferroelectric properties than the virgin BFO. The P-E loops are not saturated and start exhibiting lossy nature at x>0.4. Fig tt (f) shows the increase in remnant polarization up to x=0.4 (40 at% STO) and then a subsequent decrease in its magnitude. This decrease at x=0.4 could be attributed to a structural transformation from rhombohedral to cubic phase (59).

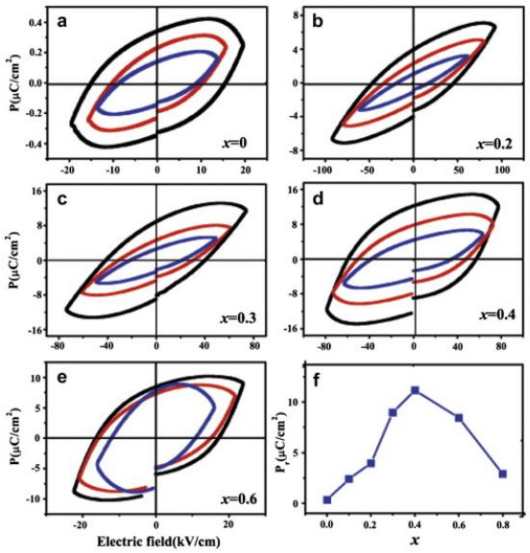

Figure 21 P-E loops for (1-x)BFO-xSTO for varying x value (59)

Dielectric studies of xBFO-(1-x)STO have been done to establish the frequency and temperature dependencies. From Figure 22(a), the real part of permittivity (ε') decreases with increasing frequency. The 60 at% STO system exhibits the largest variation of permittivity with frequency (60). Figure 22(b) shows the increasing ε' value with rising temperature.

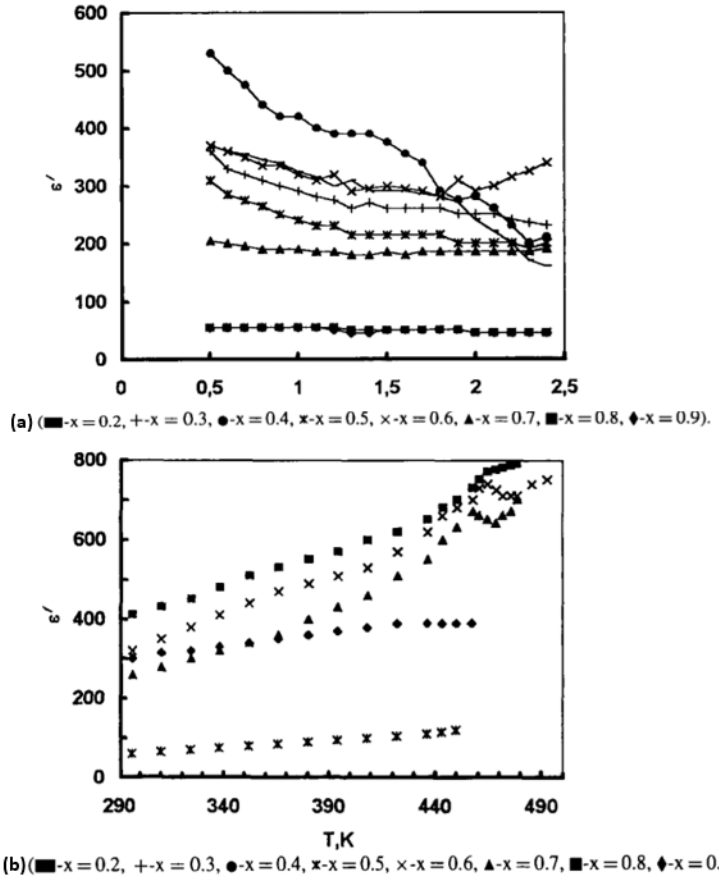

Figure 22 Variation of real permittivity (ε′) for (x)BFO-(1-x)STO for different concentrations with (a) frequency and (b) Temperature (60)

Chapter 2.

Experimental methods

2.1 Sample preparation

2.1.1 Mixing precursors

The preparation of virgin bismuth ferrite starts with the mixing of the raw materials, which in this case consists of bismuth and iron oxides. Bismuth oxide (325 mesh, 44 micron-sized powder) is milled for 24 hours before mixing. The bismuth and iron precursors are stored in an oven at high temperatures to avoid the absorption of moisture and to make the precursor measurement more precise. Depending on the system, a dopant precursor is added along with zirconia balls and isopropanol (which acts as the milling lubricant). The mixture is then milled in the ball mill for 5 hours at a speed of 200 rpm. After the completion of milling, the mixture is sieved and dried overnight.

2.1.2 Calcination and second milling

The dried precursor is collected and subsequently calcined at 775 °C in a sintering oven. The calcination was done for an hour with a ramp rate of 600 °C/hr. Once the calcined powder has cooled down freely inside the oven, it is put for another round of 5-hour milling to further reduce its size. The sintering ovens along with the milling machine are shown in Figure 23

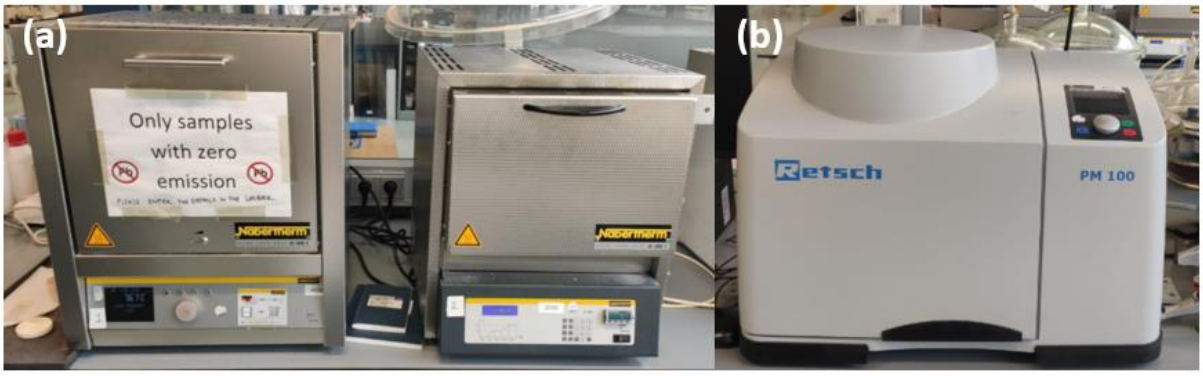

Figure 23 (a) Sintering ovens (b) Milling machine

2.1.3 Powder pelletizing

The next step in the preparation cycle involves preparing pellets from the calcined and milled powder. A 10 wt% solution of QPAC40 poly(propylene carbonate) in methyl ethyl ketone (MEK) is used as a binder. The dried powder binder is passed through a 250-micron sieve and the fine powder is then used for the pellet production. The amount of added binder and the applied pressure are initially optimized for a pure bismuth ferrite system. The details of the optimization are explained in Chapter 3.

2.1.4 Sintering and polishing

The sintering process involves heating the pelletized samples at a high temperature just below the melting point. The pellets densify and shrink to a more compact form as a result of the sintering. The choice of the sintering temperature and the sintering time depends on the bismuth ferrite system. For virgin bismuth ferrite, this temperature is taken as 775 °C. The choice is based on the work of Tuluk *et al.* which indicates the formation of phase pure bismuth ferrite samples with the highest average density at 775 °C (66). For other doped bismuth ferrite systems, the choice of sintering temperature varies depending on the density of the obtained samples and the occurrence of secondary phases. These individual choices will be explained in Chapter 3.3.

After the sintering is done, the pellets are polished on a grinding machine using a range of sandpapers (P320 [45 µm], P1000 [15 µm], P1200 [15 µm] and P4000 [5 µm]). Flat samples with high surface quality obtained after polishing are kept for drying at 100 °C, after which they can be used for further measurements.

2.2 Density measurement

The density of the samples was measured using the Archimedes method. The Archimedes principle gives a measure of the buoyancy which is experienced by the sample when it is immersed in a liquid. In theory, calculating the geometrical density of the sample should give a good indication of its density. However, density measurement using the Archimedes method is preferred as it accounts for surface irregularities that may get incorporated into the sample during sintering. Archimedes will also account for inconsistencies due to closed pores (non-interconnected pores) in the samples. The measurement is temperature-sensitive, as the density of the immersion liquid can change with temperature fluctuations. The density of the samples (ρ) immersed in liquid (here, distilled water) can be described as:

$$\boldsymbol{\rho = \frac{A}{A - B}(\rho_o - \rho_L) + \rho_L} \tag{15}$$

Where A is the weight of the sample in air, B is the sample weight in the immersion liquid, ρ_o is the temperature dependant density of the immersion liquid and ρ_L is the density of air (0.0012 g/cm^3).

2.3 Dielectric measurements

The first step for any dielectric measurement is metallization which involves applying some form of electrodes on the sample surface. The samples are sputtered using a gold magnetron sputterer (Balzers Union SCD-040). The setup uses argon as the sputter gas to create plasma at sufficiently high voltages. The plasma strikes the gold target which causes gold atoms to get sputtered on the sample, creating a thin electrode layer on its surface.

After the sputtering, the room temperature capacitance and dielectric losses of the samples are measured at a frequency of 1 kHz using an LCR meter (Agilent 4263B). The dielectric loss or tan(δ) is a measure of the dissipated electric energy and indicates ease of poling the samples. Figure 24 shows the gold magnetron sputterer and the LCR meter

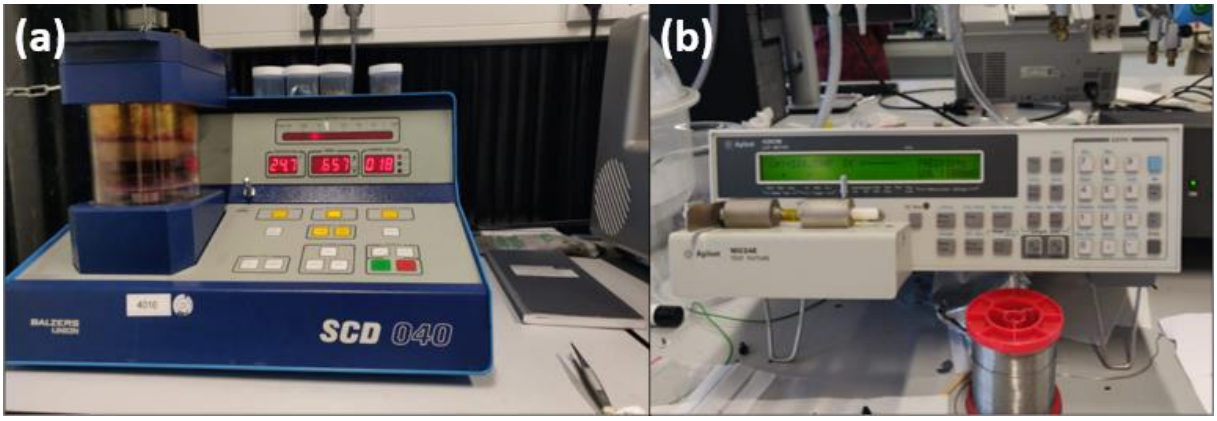

Figure 24 (a) Magnetron sputterer (b) LCR meter

2.4 X-ray diffraction

In X-Ray diffraction (XRD), electrons expelled from a heated filament are made to accelerate through vacuum to hit a metal target. The collision with the metal plate can cause some inner electrons to be knocked out, leaving outer electrons to fill in the energy gap. The X-rays produced as a result of this can then be used for characterization. Upon collision with the sample powder, X-rays will get diffracted and be subsequently detected by the diffractometer.

To understand X-ray diffraction it is essential to first understand Bragg's law. Bragg's law is a simple model for X-ray diffraction formulated by W.L Bragg and W.H Bragg in 1913. It states that constructive interference will occur when the path difference (interplanar spacing) is a simple function of the incident wavelength. For diffraction to occur, the incident X-ray will get scattered with the same angle as the incident angle. To put it mathematically,

$$n\lambda = 2dsin\theta \tag{16}$$

Where n is the order of interference, λ is the wavelength, d is the path difference and θ is the Bragg angle. The peak shape, height, position, area, and width of the XRD pattern can give useful information about the crystal size and structure, phase amount, defects, or even some induced strain. The XRD pattern obtained can be further refined and analyzed with softwares such as FullProf, TOPAS, or MAUD (Material analysis using diffraction). For this study, the FullProf crystallographic suite has been used to analyze the XRD patterns.

A Rigaku XRD-Miniflex 600 X-ray diffraction setup was used for the identification of the unit cell parameters and the phase purity of the sintered samples. The XRD was generally performed with a 2θ scan range of 20-60°, a scan speed of 1 °/min, and step width of 0.01°. The XRD setup is shown below in Figure 25.

Figure 25 Rigaku XRD-miniflex 600

2.5 Scanning electron microscope

A scanning electron microscope (SEM) uses a focused electron beam to scan the sample surface for microstructural analysis. As a result of the collision of the electron beam with the sample, a range of electron and X-ray emissions are generated. These electron emissions are detected and can be further analyzed for information about the microstructure, sample topography, and regions of secondary phases. The JEOL JSM-7500F scanning electron microscope used for this study is shown below in Figure 26.

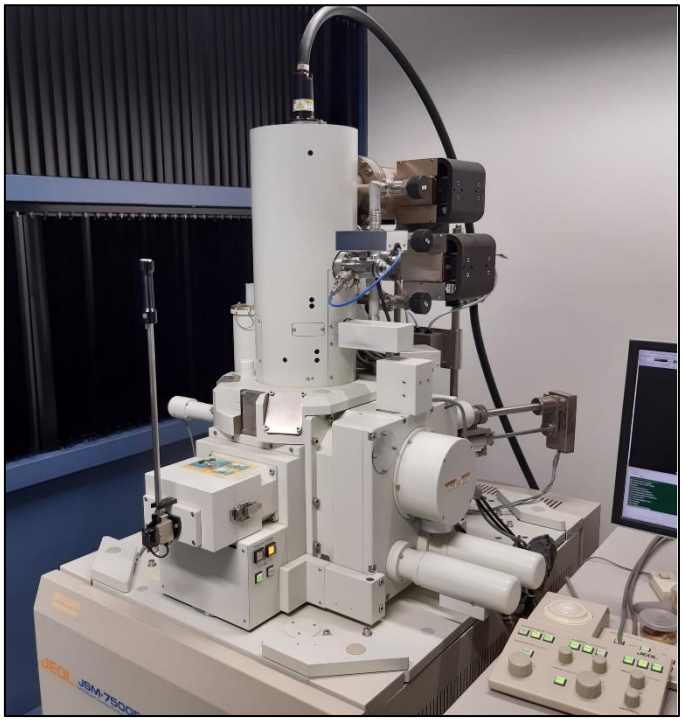

Figure 26 JEOL JSM-7500F SEM

The upper and lower secondary electron in-lens detectors (SEI and LEI respectively) can be used to analyze the effect on the sample microstructure with different sintering temperatures or different dopant loadings. The sample composition can also be analyzed using the COMPO mode which utilizes high energy backscattered electrons (scattered by 180°). Backscattered electrons can give Z-contrast, wherein elements with different atomic numbers show different contrasts in the SEM. Using this, iron (dark) and bismuth (light) rich regions can be identified within the sample.

2.6 Poling and high voltage measurements

High voltage measurements are performed on the sputtered samples before the sample is poled. The thickness of the samples is recorded before putting them in the sample holder with some silicone oil. The instrument can be used to generate P-V hysteresis loops, current density plots, and other significant electric data. Apart from this, the setup can be used to ascertain the fields at which the samples are shorting, which can act as a good framework for contact poling.

To evaluate the piezoelectric properties of the ceramic, the sputtered samples are poled at a sufficiently high electric field using the contact poling setup. The applied electric field has to be high enough to be able to influence the orientation of the Weiss domains but it also should not short the sample. The poling is done in a silicone oil bath at room temperature. Poling at elevated temperatures is not explored to avoid the issue of higher conductivity and losses at larger temperatures. The samples to be poled are fixed using the contact pins and the poling stage is immersed in the silicone bath. The voltage is applied to the samples using the amplifier and the samples are poled for an hour.

To measure the piezoelectric properties of a ceramic, it has to be poled using a strong electrical field. Poling involves reorientation of the Weiss domains upon application of an external electrical field. In an unpoled ceramic, the net polarization is zero due to the random orientation of the Weiss domains. Upon application of an electrical field, these domains can get oriented in the direction of the field. At a particular value of the electrical field, the polarization will attain its maximum value (saturation polarization, P_{sat}) due to the complete alignment of the domains. When the field is removed, some domains will retain their orientation leading to a non-zero retained polarization called the remnant polarization (P_r). The direction of the field can then be reversed to reorient the domains in the opposite direction. The electrical field at which there is net-zero polarization is called the coercive field (Ec). Figure 27 shows the Weiss domain reorientation and the hysteresis loop generated during poling.

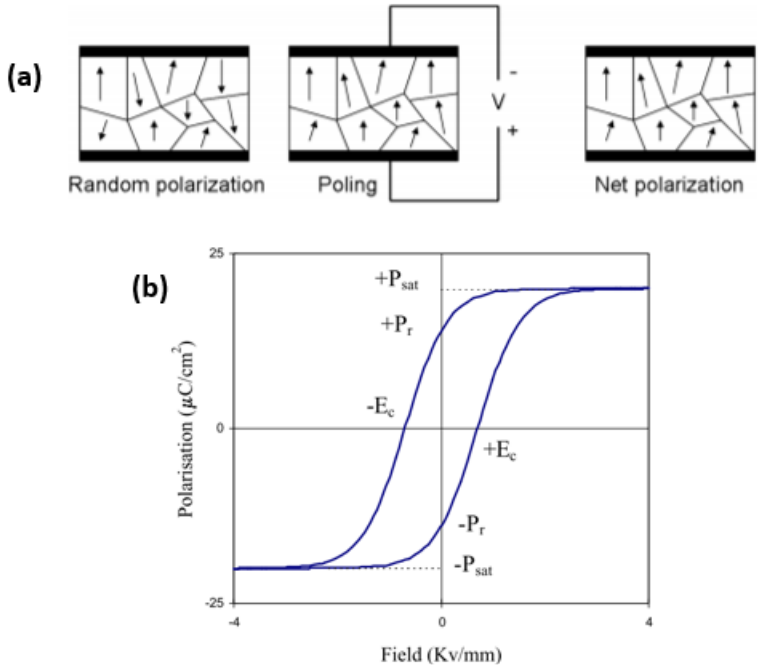

Figure 27 Domain reorientation during poling, (b) Hysteresis loop for piezoelectric material (67,68)

After poling, the dried samples are sputtered again to account for errors in d_{33} measurement due to charge build-up. Then a Berlincourt piezometer system is used to measure the d_{33} at a dynamic force of 0.25 N and 110 Hz frequency. The poling setup and the berlincourt piezometer system are shown in Figure 28 below

Figure 28 (a) Contact poling setup (b) Berlincourt piezometer

2.7 Broadband dielectric spectroscopy (BDS)

Doping piezoelectrics like bismuth ferrite with even trace amounts of dopants can cause a massive change in their dielectric and electrical properties. Here, broadband dielectric spectroscopy (BDS) of the samples can be done to measure their dielectric properties at a range of frequencies and temperatures. Before performing BDS measurements, silver electrodes are applied to the sample. Samples with silver electrodes have a better surface finish and the electrodes adhere more strongly to the sample.

The BDS has to be calibrated (first a short calibration and then using a standard 100 resistor) before the sample measurement is done. The sample is fixed in the holder which is inserted into the cryostat. Liquid nitrogen is used to cool the system during the high-temperature measurement of the sample. First, a single measurement sweep (0.1 Hz to 1 MHz) is done at

room temperature. After the single sweep, the measurement is then done for a temperature range of 25-200 °C with 25 °C increments. The BDS setup is shown below in Figure 29.

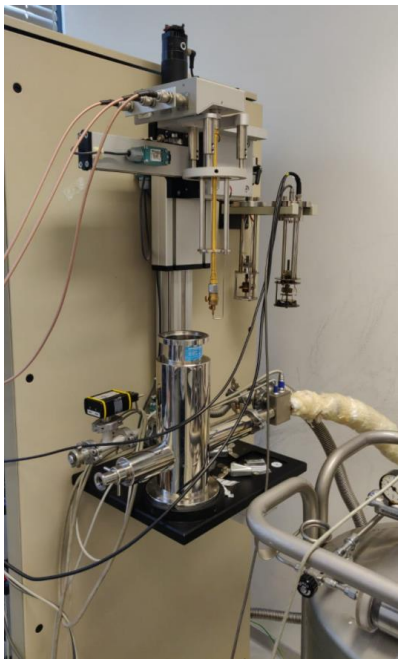

Figure 29 The BDS setup

Using the data from the BDS, further investigation into the conductivity, dielectric losses, dielectric permittivity, and impedance can be done. The variation of conductivity with frequency is analyzed using Jonscher's power law,

$$\sigma_{total} = \sigma_{DC} + A\omega^n \tag{17}$$

Where σ_{total} and σ_{DC} are the overall and the direct current conductivity respectively. ω is the angular frequency, A and the exponent n are characteristic parameters (69). The $\ln(\sigma_{DC})$ vs 1/T dependence is of great interest here as the slope of the plot can be used to calculate the activation energy.

$$\sigma = A_1 exp\left(\frac{-E_a}{k_b T}\right) \tag{18}$$

$$E_a = (-k_b)(\text{slope}) \tag{19}$$

Here E_a, A_1, and k_b are the activation energy, a pre-exponential parameter, and the Boltzmann's constant.

Complex impedance spectroscopy plots such as the Nyquist diagrams can help to separate the different contributions (grain, grain boundaries, and electrode interface) to the bulk electrical properties. It is also an effective way to calculate the relaxation frequency of the material, which in turn can help to calculate the dielectric constant of the ceramic system (70). The electrical properties can be simulated by expressing it as an RC circuit. As evident from Chapter 7.2 (the BDS section of cobalt doped BFO), there are two separate processes contributing to the overall bulk conduction. To simulate this effect, an RC circuit (demonstrated in Figure 30) with two

sets of parallel RC circuits connected in series can be designed. Each simple parallel RC circuit represents the individual components contributing to the overall conduction.

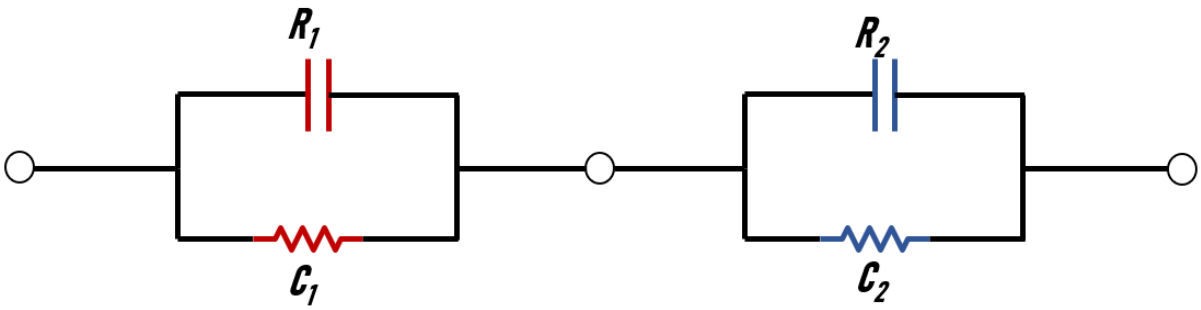

Figure 30 RC circuit for complex impedance fitting

Chapter 3.

Sample synthesis and optimization routines

This chapter highlights the synthesis route and optimization strategies adopted for the preparation of BFO based systems.

3.1 Binder optimization

Binders are used to enhance the relative density and mechanical characteristics of green ceramics so that they can be sintered without deterioration. Binder optimization was done on undoped BFO samples that were sintered at 775 °C for one hour. The pellets prepared were pressed with a 3-tonne force (~316 MPa). Figure 31 shows the variation of sample relative density and loss tangent with changing binder concentrations. The sintered samples are relatively dense but exhibit a decreasing density with increasing binder concentration. The decrease in density at higher binder concentrations could be due to the increased production of gases like CO_2 upon binder decomposition. The samples also exhibit acceptable dielectric losses (< 3% losses) for 2-8 wt% binder concentrations. The increased loss tangent at larger binder concentrations is likely due to increased porosity caused by the escape of decomposition gases. The 2 wt% binder samples exhibited the lowest dielectric losses and optimum density.

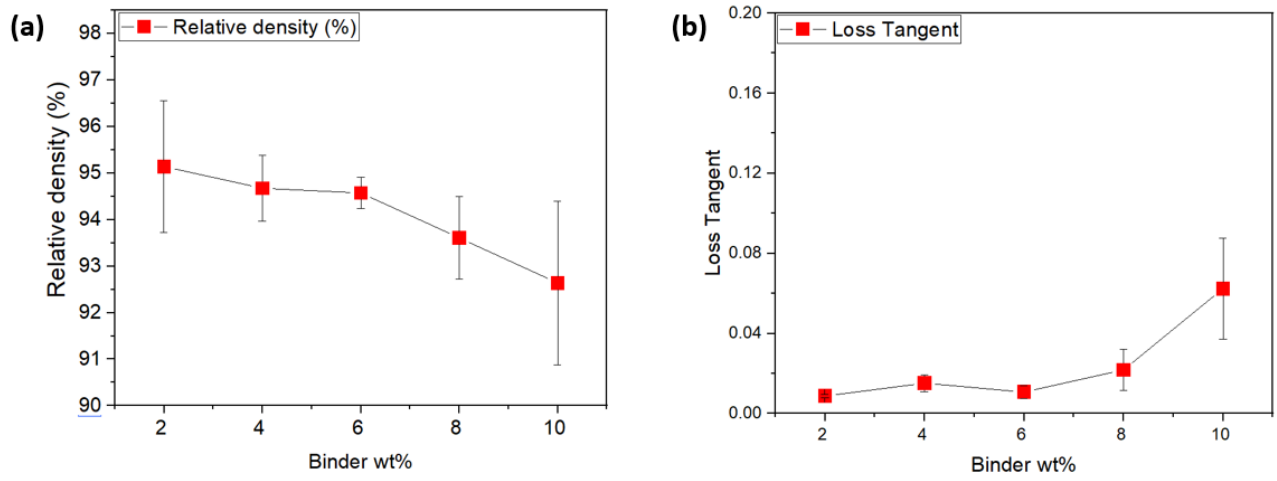

Figure 31 Variation of (a) relative density and (b) loss tangent with changing binder concentration

3.2 Pressure optimization

Pressure optimization tests were performed on BFO samples sintered at 775 °C. The samples were prepared by mixing the green ceramic with a 2 wt% binder. Figure 32 shows the variation of relative density and loss tangent with changing pressure. The pellets were pressed with 1.5 (~150 MPa), 3 (~320 MPa), and 5 (~530 MPa) tonne pressing force. Increasing the applied pressure led to the formation of more compact samples which corresponds to increasing sample

density. The dielectric losses were agreeable (< 3% losses) for the selected pressure range, with samples pressed at 320 MPa exhibiting the lowest losses.

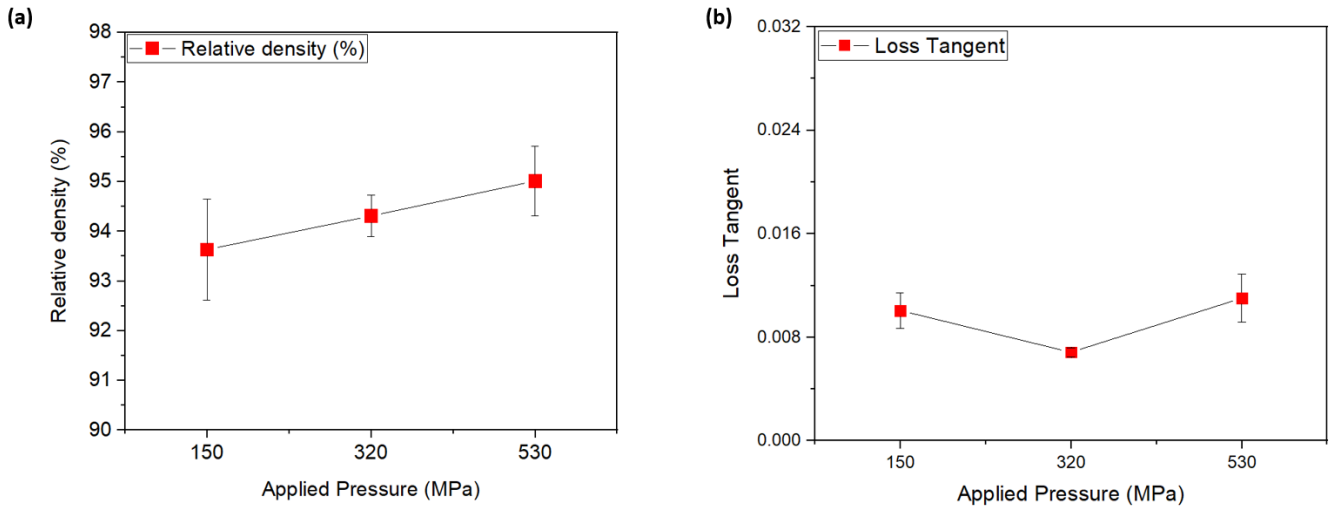

Figure 32 Variation of (a) relative density and (b) loss tangent with changing applied pressure

From the pressure and binder optimization studies samples with 2 wt% binder, pressed at 320 MPa present the optimum values. However, samples with 2 wt% binder sometimes showed cracks during pressing. To avoid any suboptimal pellets, a 4 wt% binder concentration was selected for the synthesis of all samples.

3.3 Calcination and sintering profiles

As per previous work on BFO, the calcination temperature of 750 °C was shown to produce the lowest amount of secondary phases (66). Due to the addition of dopants, other secondary phases apart from the primary perovskite phase may be developed during calcination. XRD analysis of BFO powder calcined at 775 °C in the air at a rate of 600 °C/hr for one hour showed next to no secondary phases (see Figure 33). For the sake of consistency, a similar calcination profile is selected for pristine BFO, doped BFO, and the BFO-STO powders.

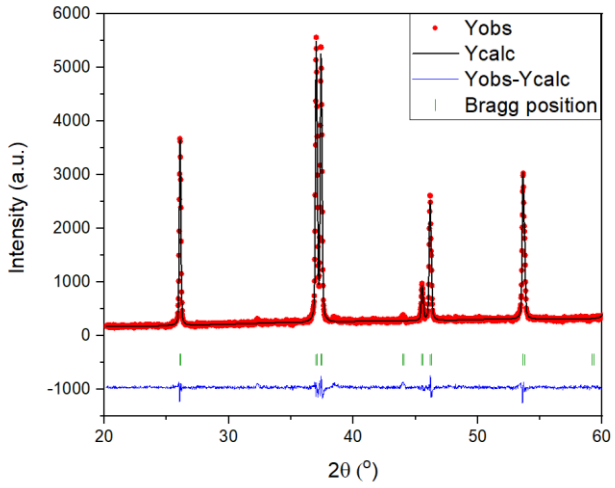

Figure 33 XRD pattern for the calcined BFO ceramic powder

Pristine BFO samples were sintered at a temperature of 775 °C. As mentioned before (in section 2.1.4 Sintering and polishing) the choice is based on getting highly dense and phase pure BFO powders using the particular sintering profile (66). The calcination and sintering profiles for BFO samples are shown in Figure 34 (a-b) below.

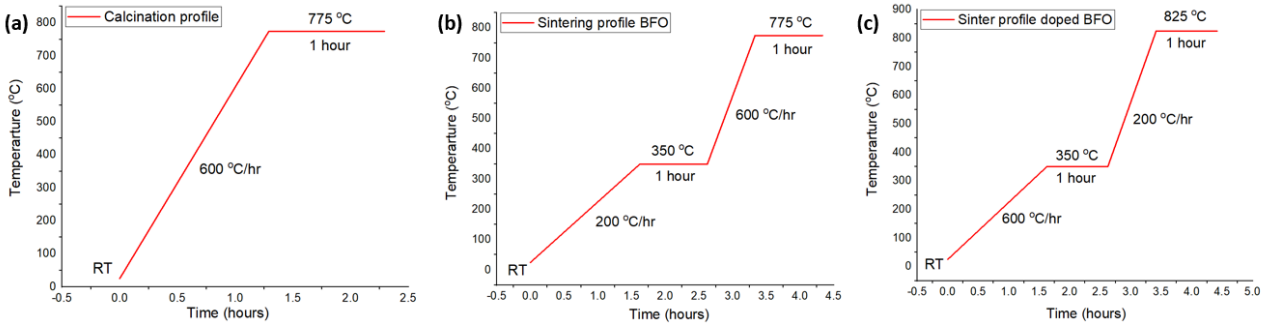

Figure 34 (a) Calcination profile, (b) Sinter profile for virgin BFO and (c) Sinter profile for doped BFO

Figure 34 (c) shows the sintering profile chosen for the doped BFO (titanium and cobalt doped) system. The choice of the profile was based on the relative density and the dielectric losses of the sintered samples. Figure 35 shows the XRD profiles of 1 at% Ti-doped BFO at different sintering temperatures. Samples sintered at 825 °C were dense (≈ 95 % relative density) and exhibited a relatively low amount of secondary phases. The sinter profile was kept the same for all the different dopant systems.

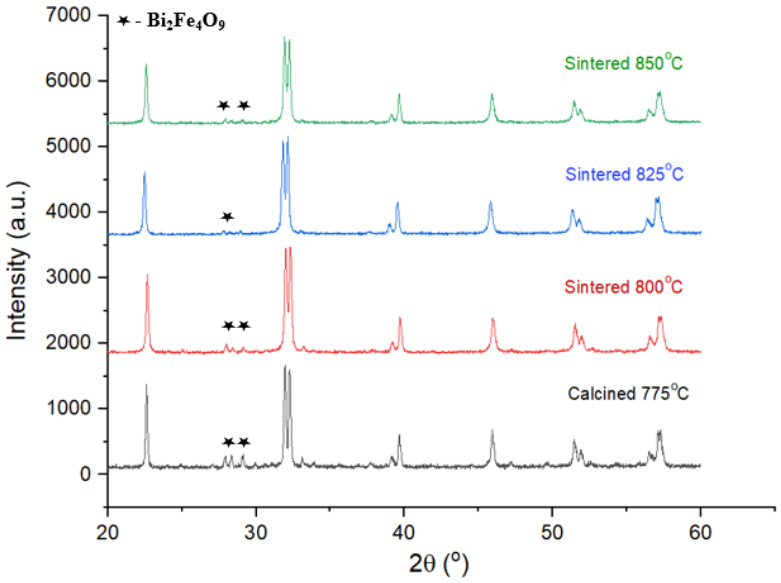

Figure 35 XRD of 1 at% Ti-doped BFO samples at different sintering temperatures

The sintering profiles for the BFO-STO system are shown below in Figure 36. The sintering is done at higher temperatures with increasing STO concentration. For 50 at% STO, the sintering time also had to be increased, as sintering at 1055 °C for one hour produced samples with a brownish hue, which is characteristic of an incompletely sintered sample. For 20 at% STO an additional temperature step at 700 °C is introduced, as a direct ramp to the sintering temperature led to extremely lossy samples. A large number of trials were done to optimize the sintering profiles for the different STO systems. Further work has to be done to find a profile that can be utilized consistently throughout these different STO systems.

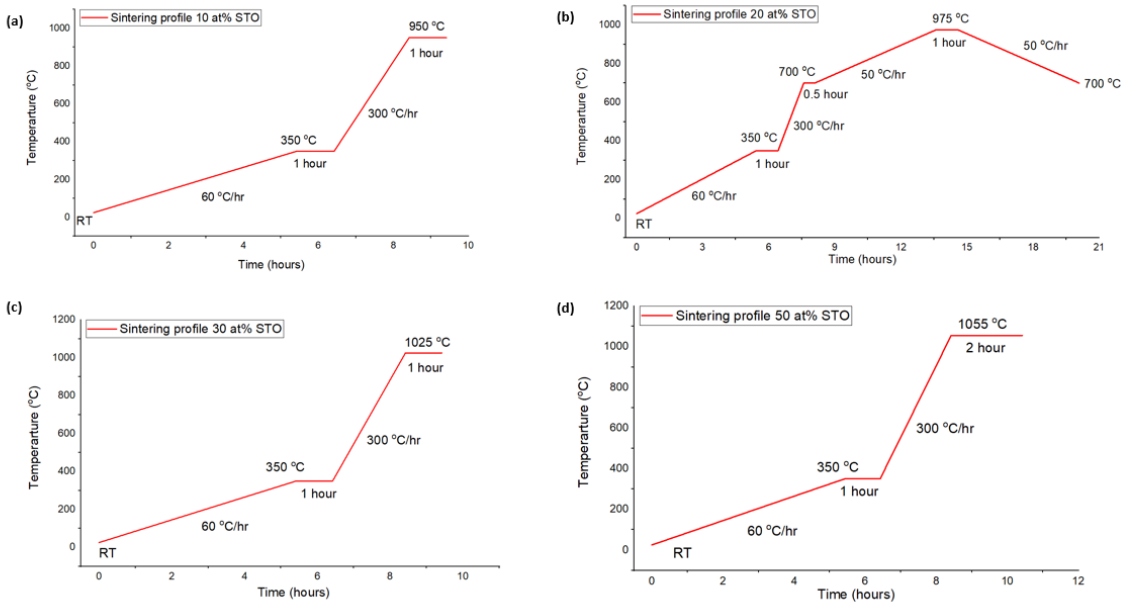

Figure 36 Sinter profile for (a) 10 at% STO, (b) 20 at% STO, (c) 30 at% STO and (d) 50 at% STO

Chapter 4.

X-ray diffraction (XRD) results

This chapter provides a brief overview of the relevant X-ray diffraction results. The chapter has been split into subsections based on the different dopants. Full pattern matching is performed to gather information on the lattice parameters, profile shape, and background. Rietveld refinements were done for a few systems to get more information on the phase composition and the peak intensities. Appendix 10.1 can be viewed for more details on the results of the full pattern matching and refinements.

4.1 BFO

The XRD patterns shown in Figure 37 confirm the formation of the rhombohedral structure with the R3c space group. The shape of the pattern matches well with other XRD patterns of BFO reported in the literature (13,14,66). The lattice parameters obtained from the full pattern matching are a=b= 5.58123(2) Å and c=13.87698(1) Å. The goodness of the fit is corroborated by the small Bragg R factor of 5.83. The Bragg R factor indicates how well the data calculated from the model matches the experimental data. The presence of iron-rich (Pbam) and bismuth-rich (I23) secondary phases have also been detected by the Rietveld refinement, with small amounts of $Bi_{25}FeO_{39}$ and $Bi_2Fe_4O_9$ (≈ 2 % each) present in the synthesized sample.

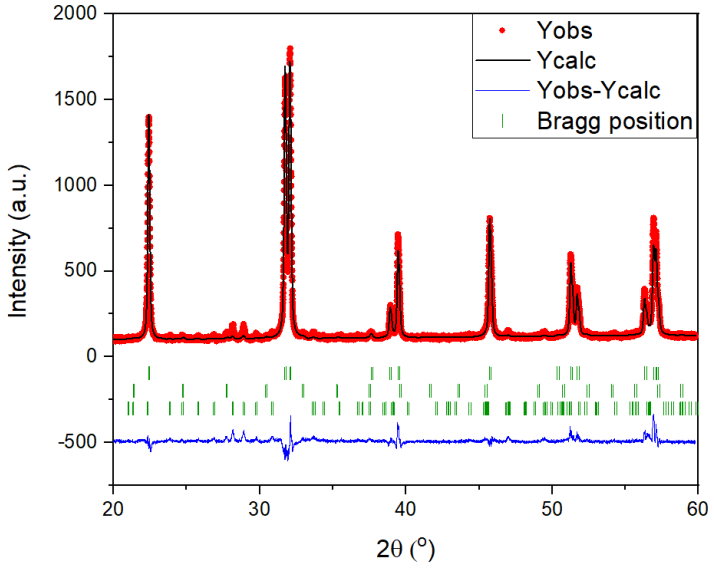

Figure 37 XRD pattern for BFO sintered at 775 °C

4.2 Cobalt

The XRD patterns shown in Figure 38(a), are similar to the cobalt doped BFO XRD patterns reported in the literature (43,51,71). The general shape of the cobalt patterns is also very similar to the XRD pattern of BFO. However, with an increase in the cobalt dopant, there is a change in the [012], [104], [110], and [202] peak shapes. As evident from Figure 38(b) there is no appreciable change in the lattice parameter with cobalt doping. This indicates no major

structural change with the incorporation of cobalt in BFO. This is expected as the ionic radii of Co^{3+} (61 pm) is almost similar to that of Fe^{3+} (64.5 pm) (41).

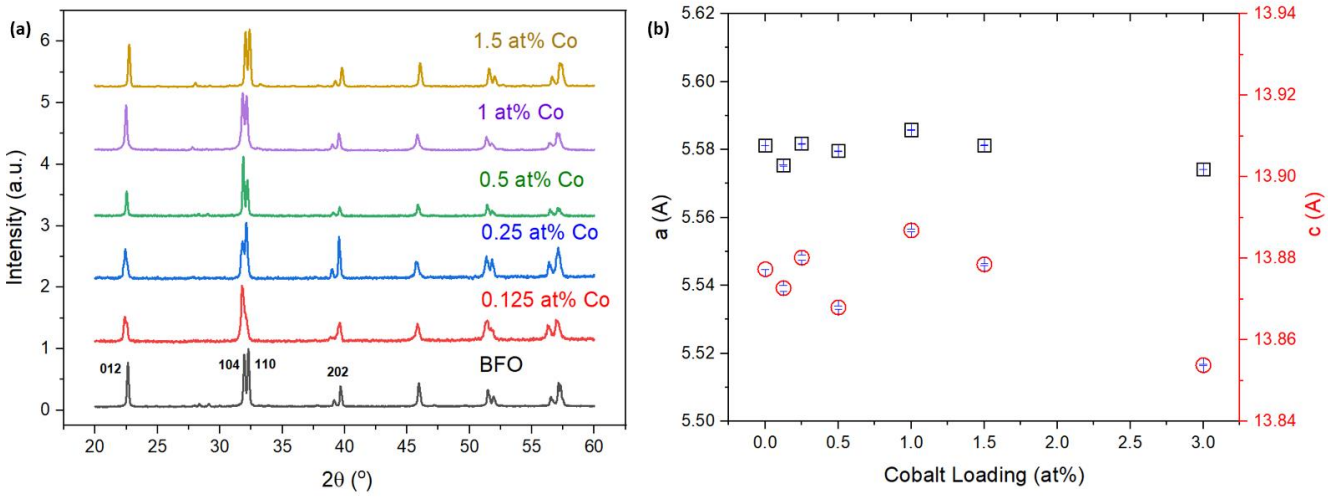

Figure 38 (a) XRD pattern and (b) Variation of lattice parameters, for different cobalt loadings

For analysis of phase composition, Rietveld refinements have been performed on 1 at% and 1.5 at% Co. The refined patterns for 1 and 1.5 at% Co are shown in Figure 39 below, with Bragg R factors 8.69 and 6.98 respectively. A majority R3c perovskite phase is present in both the systems (≈ 96 and 94 % respectively) along with some bismuth-rich phase (≈ 3 and 5 % respectively). Both these samples have a relatively low amount of iron-rich secondary phase (0.55 and 0.65 % respectively).

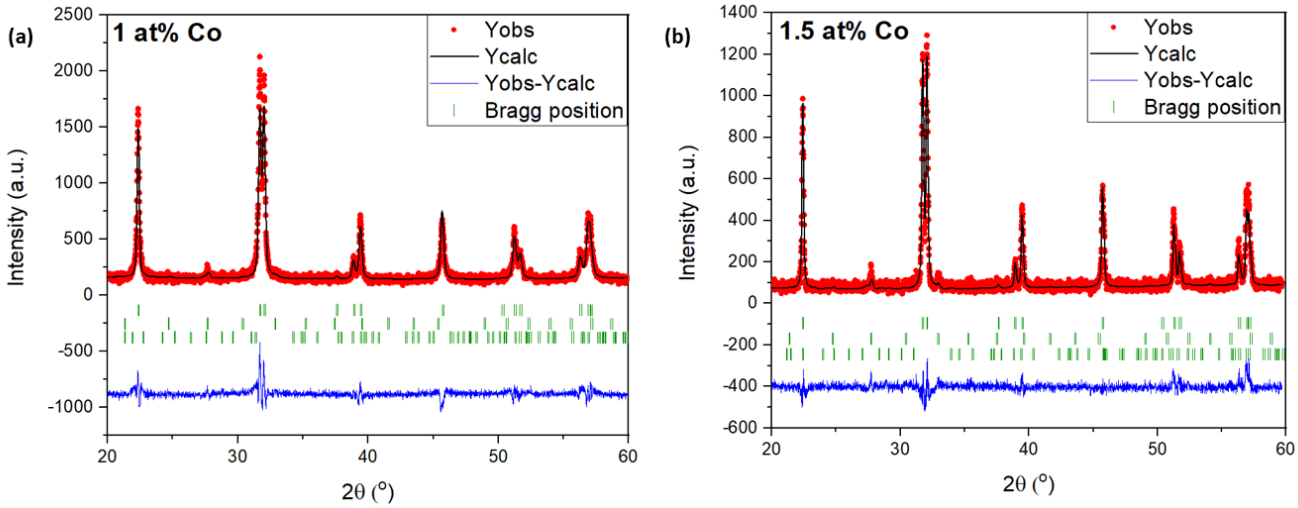

Figure 39 XRD patterns for (a) 1 at% Co and (b) 1.5 at% Co

4.3 Titanium

From the XRD pattern shown in Figure 40 below, there is no major change in the shape of the overall XRD patterns with the introduction of titanium at the B-site of the perovskite. However, a noticeable difference in the shape of the [104] and [110] peaks can be observed, with the dual peaks merging with increasing titanium concentration.

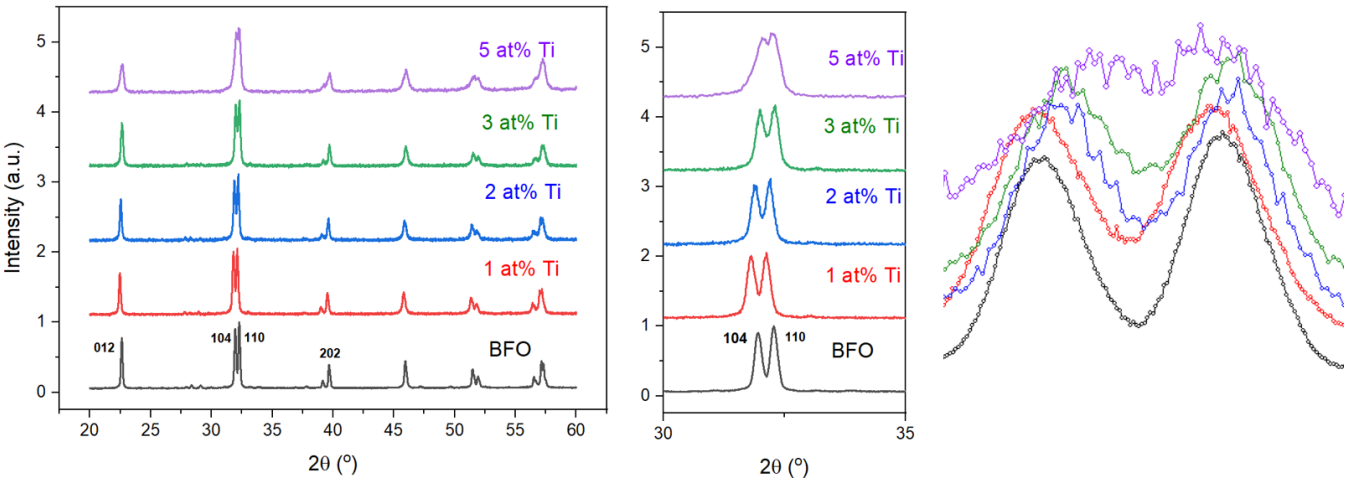

Figure 40 XRD pattern for different titanium loadings

As evident from Figure 41(a), there is no major change in the lattice parameters with increasing titanium concentration. This can be attributed to similar ionic radii of Ti^{4+} (0.68 Å) and Fe^{3+} (0.64 Å) which allows easier incorporation of titanium into the B site of the perovskite (34). The Rietveld refinements show the presence of a small amount of impurity phases. The 3 at% Ti sample has a 94 % major R3c perovskite phase, with the remaining 6 % being iron and bismuth rich phases ($Bi_{25}FeO_{39}$ (≈ 4 %) and $Bi_2Fe_4O_9$ (≈ 2 %))

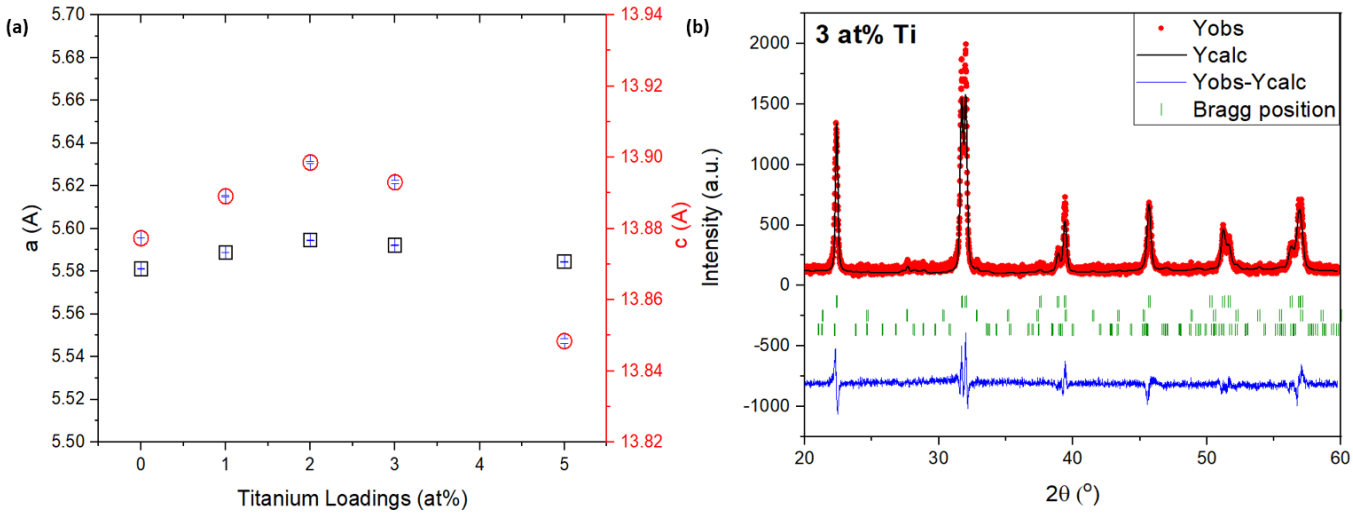

Figure 41 (a) Variation of lattice parameters for titanium loadings, (b) XRD pattern for 3 at% Ti

4.4 Cobalt-Titanium (Co-Ti)

Two cobalt-titanium systems (0.25-0.25 and 0.25-1 at% Co-Ti) have been explored in this study. The XRD pattern demonstrated by Figure 42(a) shows a similar overall shape, which is expected due to the minute concentrations of the dopants. Figure 42(b) shows the variation of the lattice parameters. As stated earlier, no major change in the lattice parameters is observed with changing dopant concentration. The minute changes in the value of lattice parameters (a and c) will cause small distortions in the rhombohedral perovskite structure.

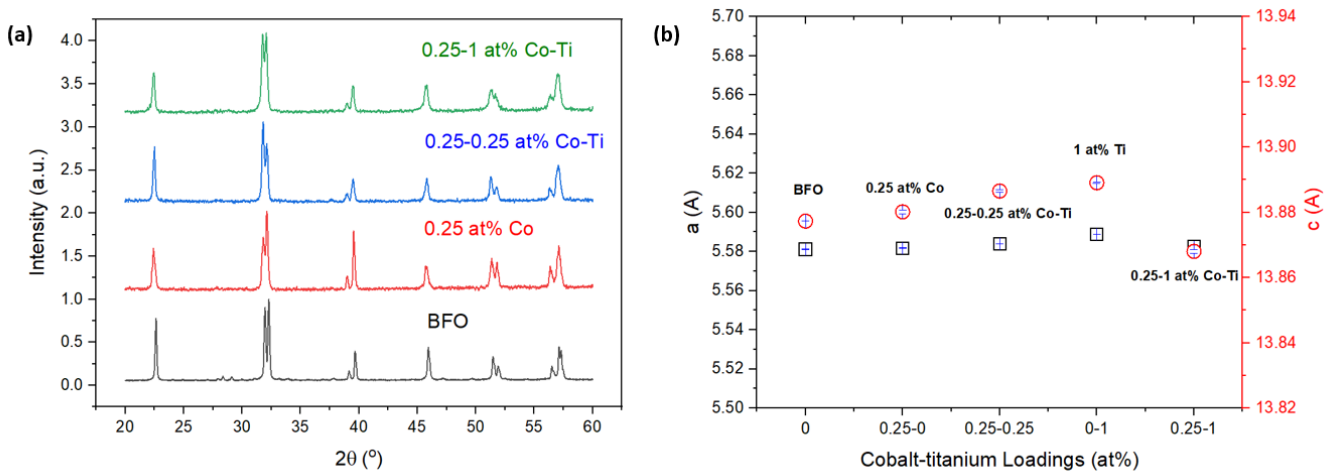

Figure 42 (a) XRD patterns and (b) Variation of lattice parameters, for cobalt-titanium loadings

4.5 BFO-STO

The XRD patterns for the BFO-STO solid solutions are shown in Figure 43 below. BFO has an R3c rhombohedral structure while STO has a cubic structure with the Pm-3m space group (59). With the increasing concentration of STO, there are noticeable changes in the shape and intensities of [104], [110], [202], and [024] peaks. Increasing the STO concentration leads to the merging of the dual [104] and [110] peaks. This merging of the peaks to a single peak can be attributed to a shift to a cubic structure with the rising STO concentration (72,73). At 20 at% STO there is a definite change in the dual peaks which is indicative of a structural transition from a rhombohedral to pseudocubic phase.

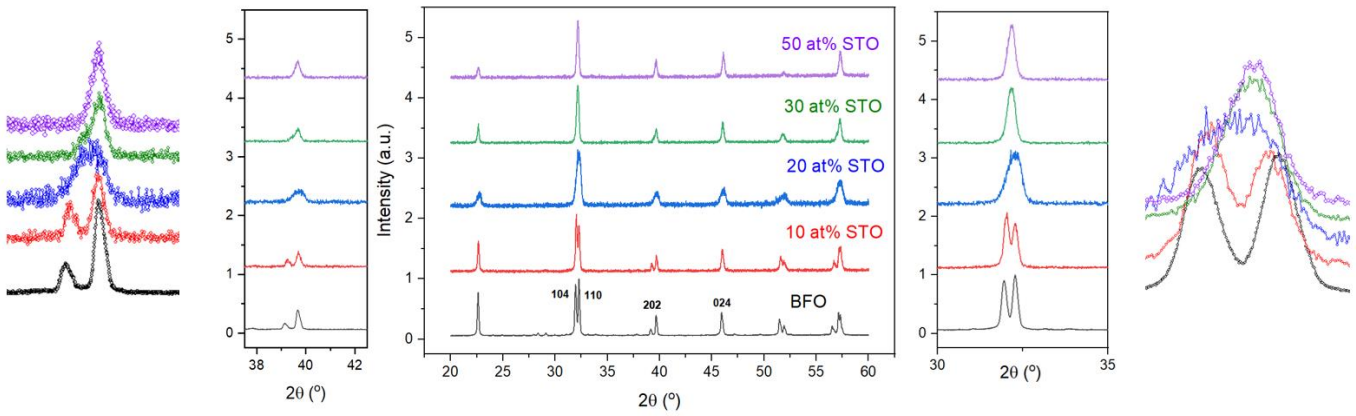

Figure 43 XRD patterns for BFO-STO systems

Chapter 5.

Microstructure study

This chapter highlights the SEM micrographs of the fracture surface for all major dopant loadings. To observe distinguishable fracture profiles, the samples have been either thermally etched or etched with acid. Thermal etching was done at temperatures 100 °C below their sintering temperatures for 20 minutes. For the titanium loadings, etching with acid either yielded no result, *i.e.*, no clear indication of microstructure or the effect of the acid was strong enough to damage the samples. Table 1 gives the approximate grain size values for the different doped BFO systems.

Table 1 Average grain size of the doped BFO samples from the SEM images

	BFO	**Cobalt (at %)**					**Titanium (at %)**				**Cobalt-titanium (at %)**		**BFO-STO (at %)**			
		0.125	**0.5**	**1**	**1.5**	**3**	**1**	**2**	**3**	**5**	**0.25-0.25**	**0.25-1**	**10**	**20**	**30**	**50**
Average grain size (microns)	2	3.8	3.7	5.7	3.8	3.1	<1	1.1	0.6	1.1	1.76	0.82	5.6	3.2	4.9	3.4

5.1 BFO

Micrographs of samples sintered at 775 °C show a clear and uniform grain structure. The samples are dense with a relative density of 95 %. Figure 44 shows the microstructure profiles for BFO. The average grain size of the BFO was around 2 microns.

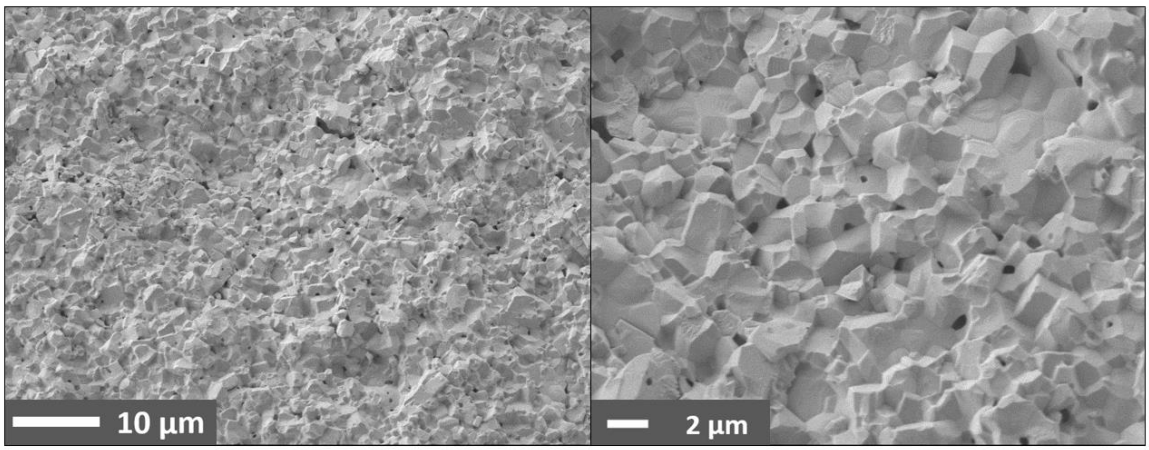

Figure 44 SEM images for BFO at (a) x1000 and (b) x3000 magnifications

5.2 Cobalt

An increase in the grain size of BFO with cobalt doping is observed from the micrographs in Figure 45. The micrograph of 0.25 at % cobalt shows a significant number of pores which is consistent with the lower density of the samples (see Figure 45). The increased grain size may be associated with the large number of oxygen vacancies produced by the introduction of cobalt. The high mobility of oxygen vacancies relative to other species allows more oxygen ions migration across the grain boundaries leading to grain growth.

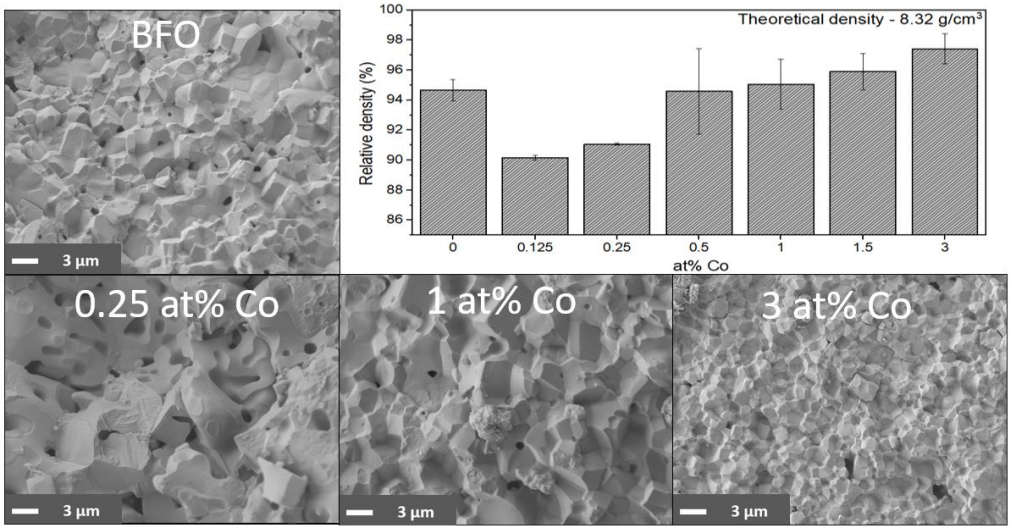

Figure 45 SEM images and density measurements for cobalt doped BFO sintered at 825 °C

5.3 Titanium

Figure 46 shows a reduction in grain size with increasing titanium doping. This can be attributed to the reduced oxygen vacancies as a result of donor-type doping. The low amount of oxygen vacancies implies slower oxygen ion movement leading to lower grain growth. The 3 at% and 5 at% titanium loadings also show reduced density. This may be due to the sintering temperature (825 °C) and time not being sufficient for the complete sintering of the titanium samples.

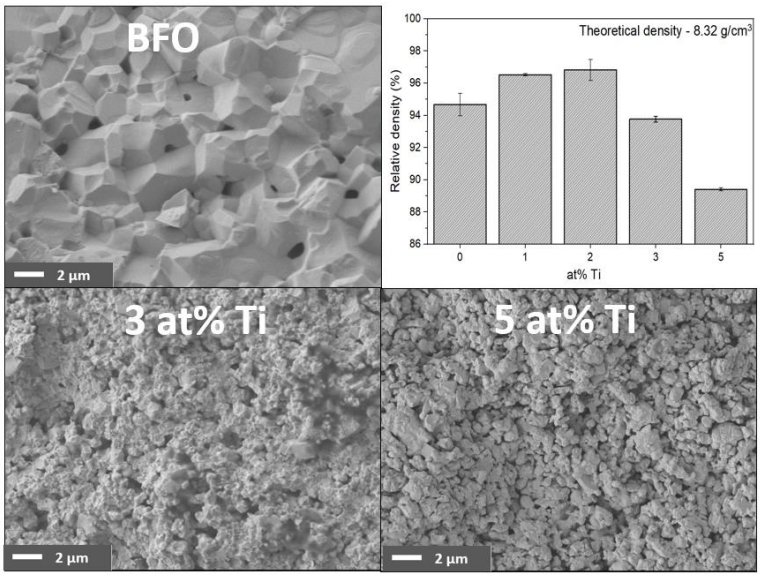

Figure 46 SEM images and density measurements for titanium doped BFO sintered at 825 °C

5.4 Cobalt-Titanium (Co-Ti)

Figure 47 shows the micrographs for cobalt-titanium co-doped systems. The addition of trace amounts of titanium leads to a reduction in grain size. Further reduction in grain size is observed at higher titanium loadings, with the 0.25-1 at% Co-Ti having an average grain size of less than one micron. The samples also show reduced density and have a large number of pores.

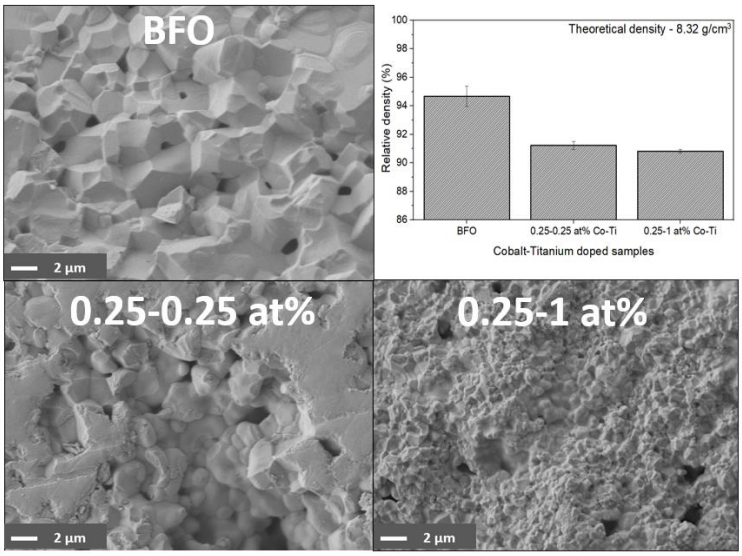

Figure 47 SEM images and density measurements for cobalt-titanium doped BFO sintered at 825 °C

5.5 BFO-STO

From Figure 48, a clear grain structure can be observed for the BFO-STO systems. The average grain size for these samples varies between 3 to 6 microns. A direct comparison of the grain size with increasing STO concentration (at% STO) is not suitable in this case, as these samples have been sintered using different sintering profiles. As mentioned previously in Chapter 3.3, different sintering temperatures, heating-cooling rates, and sintering time have been adopted to minimize the dielectric losses in these systems. The 20 at% STO sample is extremely porous, with a relative density of 85 %.

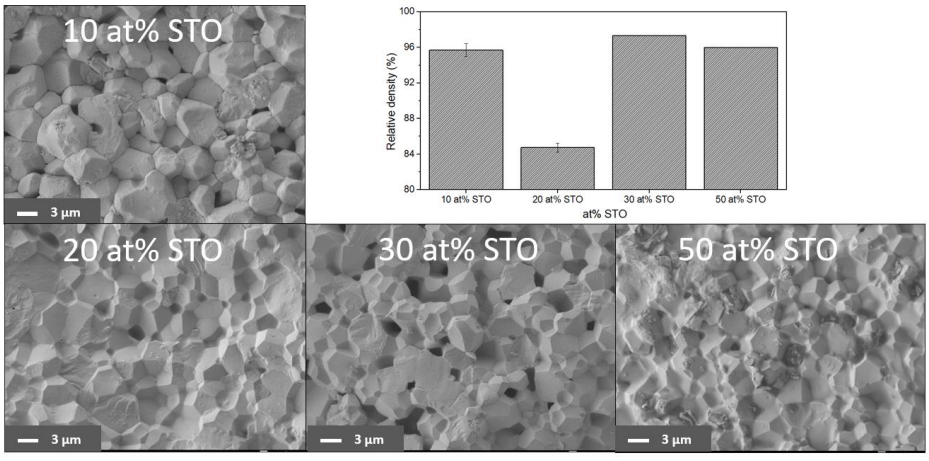

Figure 48 SEM images and density measurements for BFO-STO systems

Chapter 6.

High Voltage measurements

This chapter highlights the hysteresis and current loops as well as the current density plots for the different doped BFO systems. The variation of the piezoelectric charge and voltage constants (d_{33} and g_{33}), dielectric losses, and capacitance are also discussed.

6.1 BFO

The shape of the polarization vs electrical field (PE) hysteresis loop of BFO is consistent with the subcoercive (un-saturated) capacitor-like response found in the literature (74). The hysteresis loop presented in Figure 49(a) is also un-pinched since no quenching or heat treatments were done during processing. The existence of pinched loops has often been ascribed to the domain wall pinning by defects which can be easily induced in the system by changing quenching temperatures and cooling rates (14,75).

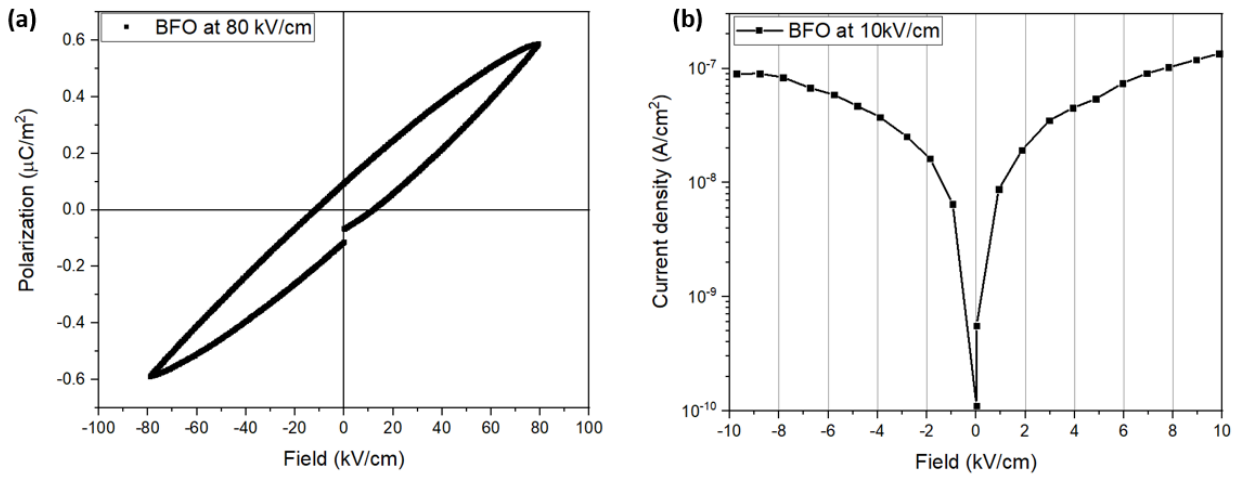

Figure 49 (a) PE loop and (b) Current density for BFO sintered at 775 °C

The most important point here is the leakage characteristics of our BFO. The PE loop obtained here is not lossy and has a very thin shape. The low leakage characteristic of our BFO is further supported by the leakage current density (CD) plot shown in Figure 49(b) and by the low value of loss tangent (≈0.015) obtained for this system. The prepared BFO has one order of magnitude less current density at room temperature in comparison to the values recently reported in the literature (51).

Despite having synthesized BFO with low leakage characteristics, the difficulty associated with poling due to its high coercive field still exists. The coercive field is temperature dependant and decreases with increasing temperature (1). Figure 50 shows the evolution of the PE hysteresis loops with increasing temperature. The hysteresis loop opens up more at higher temperatures (Figure 50(a-b)) but the sample also becomes more lossy due to increased dielectric losses. The change in the loop shape in Figure 50(c) may be attributed to pinning effects by mobile charge carriers at higher temperatures. However, the hysteresis loop still doesn't saturate before reaching the breakdown field.

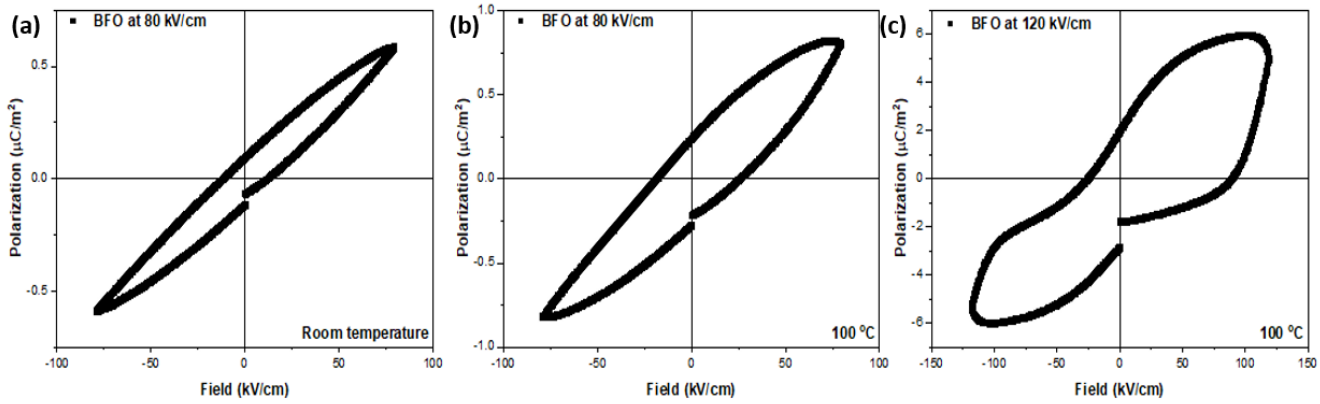

Figure 50 PE hysteresis loops for BFO at (a) Room temperature, 80 kV/cm (b) 100 °C, 80 kV/cm and (c) 100 °C, 120 kV/cm

To avoid large dielectric losses at higher temperatures, BFO was poled at room temperature with a field of 80 kV/cm for one hour. The poling conditions are kept the same for the different systems throughout this study for the sake of continuity and ease of comparison.

6.2 Cobalt

0.125 at%, 0.25 at% and 0.5 at% Co

Figure 51(a) shows PE hysteresis loops for cobalt-doped BFO samples sintered at 825 °C. The cobalt doped hysteresis loops show a characteristic pinched shape which is consistent with the literature (39). The pinched nature of the loop can be attributed to the domain wall pinning caused by charged defects such as oxygen vacancies, which have been induced in the system as a result of the acceptor cobalt doping (1). An increase in hysteresis loop pinching with increasing cobalt concentration is also noticeable from Figure 51(a). The hysteresis loops for 0.125 at% and 0.25 at% Co are pinched but open up at the given poling fields. The pinched hysteresis loop for 0.5 at% Co however does not open up significantly due to reduced polarization switching as a result of more domain wall pinning by defects.

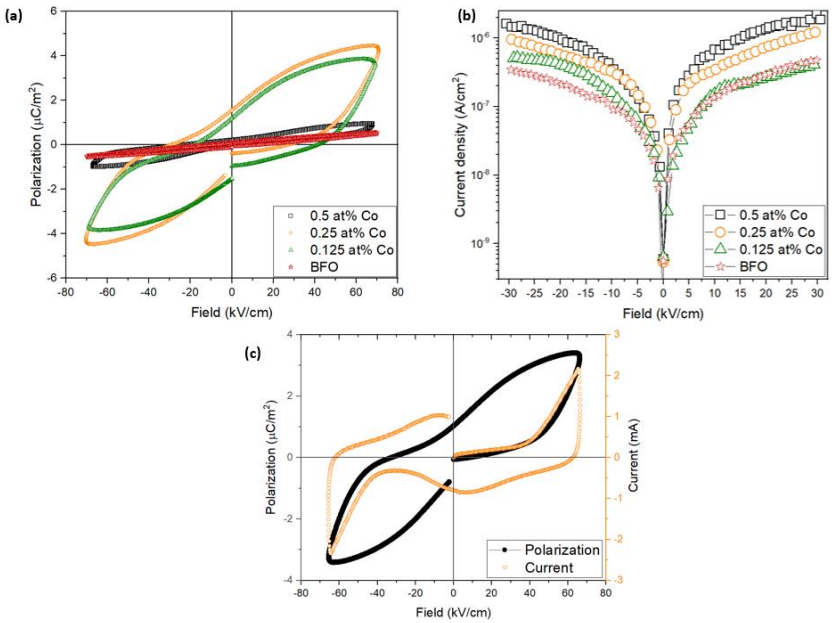

Figure 51 (a) PE loop and (b) Current density for cobalt doped BFO sintered at 825 °C (c) Domain switching in 0.25 at% Co at 70 kV/cm

The current density plots (Figure 51(b)) show an increase in the room temperature leakage current with increasing cobalt dopant concentration. Co^{2+} dopant ion acts as an acceptor and promotes oxygen vacancies and defect concentration leading to larger leakage currents (39).

The defects induced by cobalt substitution are also responsible for their improved polarization. The introduction of a very small number of Co^{2+} ions into BFO improves polarization due to increased concentration of oxygen vacancies which alters the dipole configuration. In literature, cobalt doping of BFO in trace amounts has been shown to induce large quadrilateral dipoles (43). These induced dipoles will influence domain switching, as evidenced from Figure 51(c). Doping BFO with a trace amount of cobalt (0.25 at%) facilitates domain switching at poling fields as low as 70 kV/cm.

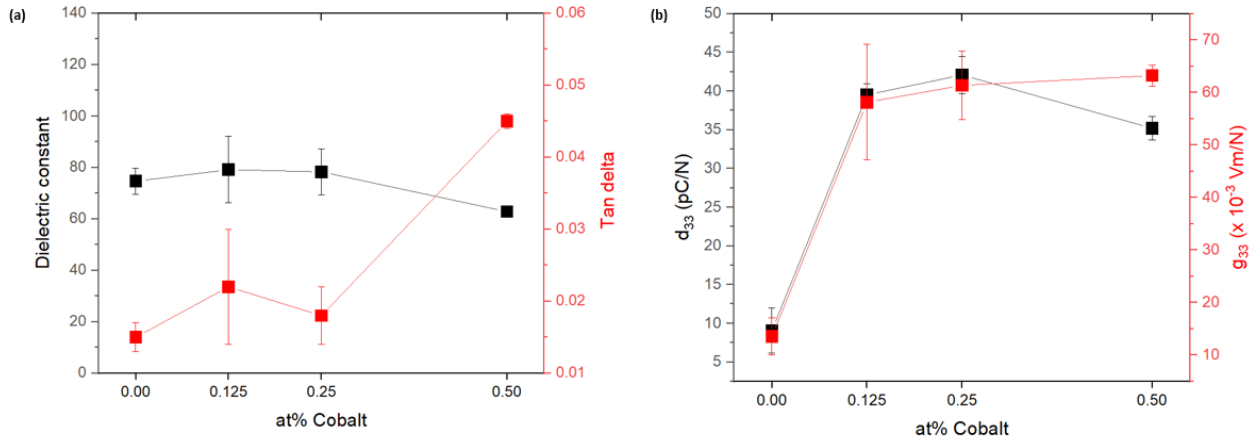

Figure 52 shows the variation of d_{33}, g_{33}, dielectric constant, and dielectric loss tangent with different cobalt loadings. There's a substantial increase in the d_{33} (and as a result g_{33}) with the introduction of a trace amount of cobalt. The increased d_{33} is in agreement with the enhanced polarization shown in the PE hysteresis loops for the doped samples. The d_{33} achieves a maximum at 0.25 at% Co dopant, but the g_{33} experiences further increase and maximize at 0.5 at% Co doping due to the decreased dielectric constant. However, the increase in the g_{33} when moving from 0.25 to 0.5 at% Co is relatively small.

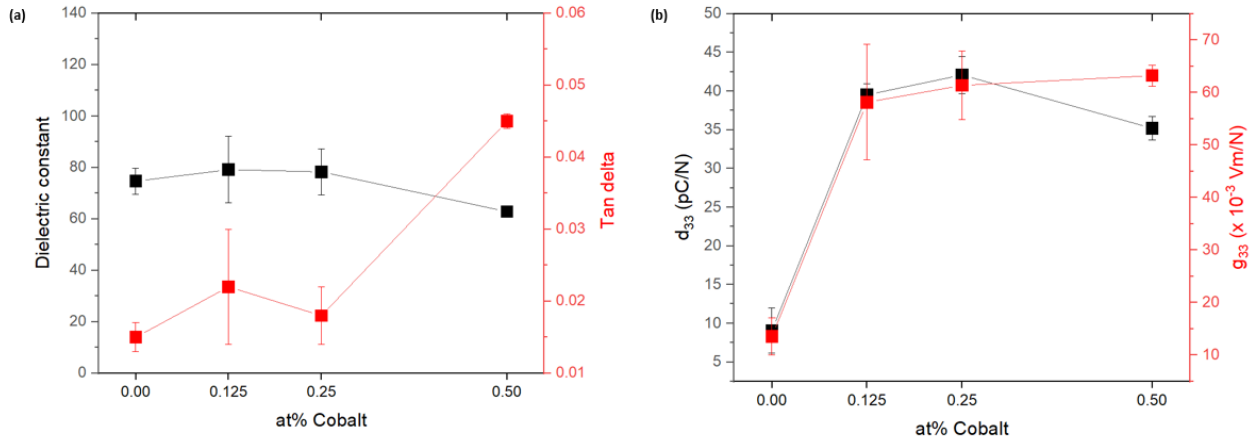

Figure 52 Variation of (a) d_{33} and g_{33} and (b) dielectric constant and tan delta for different cobalt-based BFO doping

1 at%, 1.5 at%, and 3 at% Co

Figure 53 (a) shows PE hysteresis loops for 1, 1.5, and 3 at% cobalt doped BFO samples sintered at 825 °C. The BFO samples doped with a larger concentration of cobalt (> 0.5 at% for this study), show lossy and underdeveloped PE loops. The loops are reported at different fields due to the different breakdown fields with changing dopant concentrations. The lossy nature is supported by the large dielectric loss tangent (Figure 54) and increased room temperature leakage current values. The increase in leakage is consistent with previous results and literature, with Co^{2+} dopant ion promoting oxygen vacancies and defects at larger dopant concentrations.

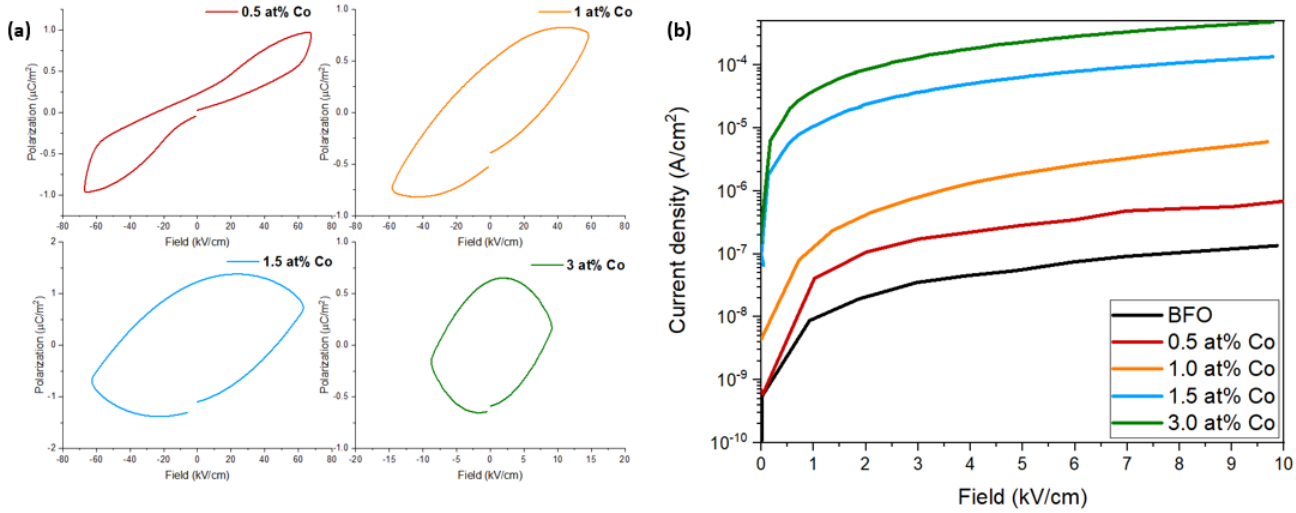

Figure 53 (a) PE loop and (b) Current density for 1, 1.5 and 3 at% cobalt doped BFO sintered at 825 °C

The dielectric constant increases, similar to the loss tangent, with increasing cobalt dopant concentration. The large dielectric constant could be related to the large dipole moment as a result of the production of oxygen vacancies.

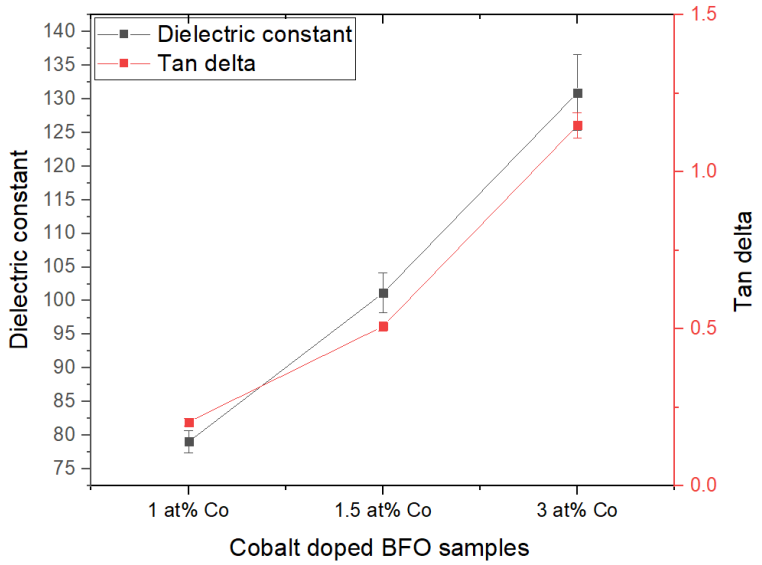

Figure 54 Variation of dielectric constant and tan delta for 1, 1.5, and 3 at% cobalt-based BFO doping

6.3 Titanium

Figure 55(a) shows the PE hysteresis loops for titanium doped BFO samples sintered at 825 °C. The obtained loops are thin, unsaturated and their shape agrees with the literature (47,48). The extremely thin structure of the loops suggests a non-lossy nature of the titanium doped samples, which is confirmed by the room temperature CD study. The room temperature CD plots (Figure 55 (b)) suggest that titanium doping is successful in improving the leakage characteristics of BFO. This is due to Ti^{4+} substitution at the B site which suppresses the formation of oxygen vacancies resulting in reduced leakage current.

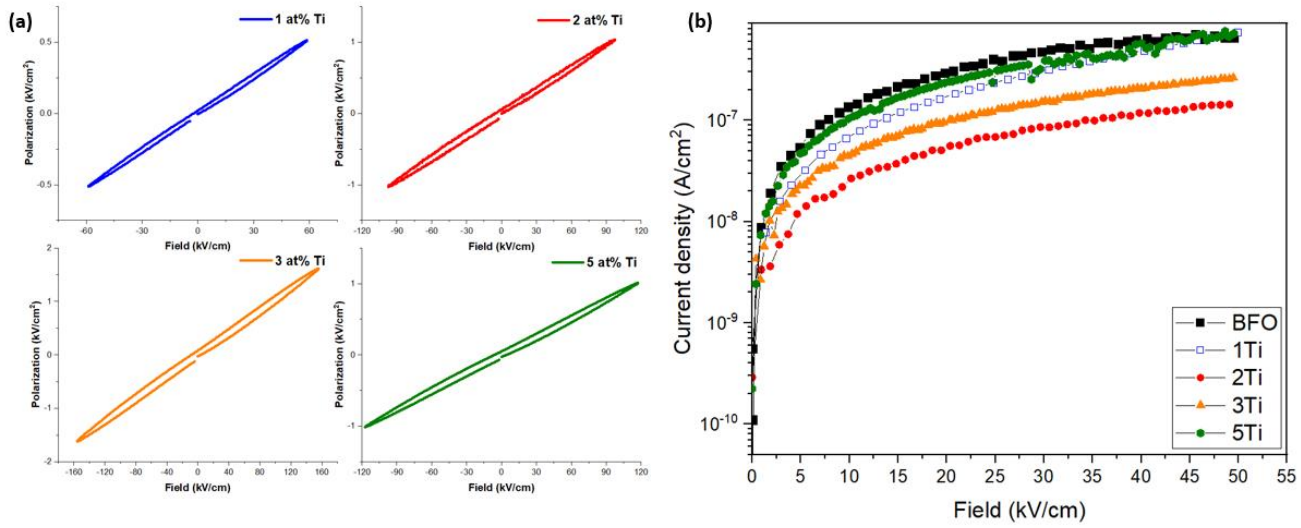

Figure 55 (a) PE loop and (b) Current density for titanium doped BFO sintered at 825 °C

The dielectric constant and the loss tangent variation with titanium doping at room temperature are shown in Figure 56(a). Substitution of Ti^{4+} at the B site causes an increase in the dielectric constant and a decrease in the loss tangent of the BFO system. Poling of titanium doped BFO however poses a problem, with very low d_{33} values obtained from samples poled at 80 kV/cm.

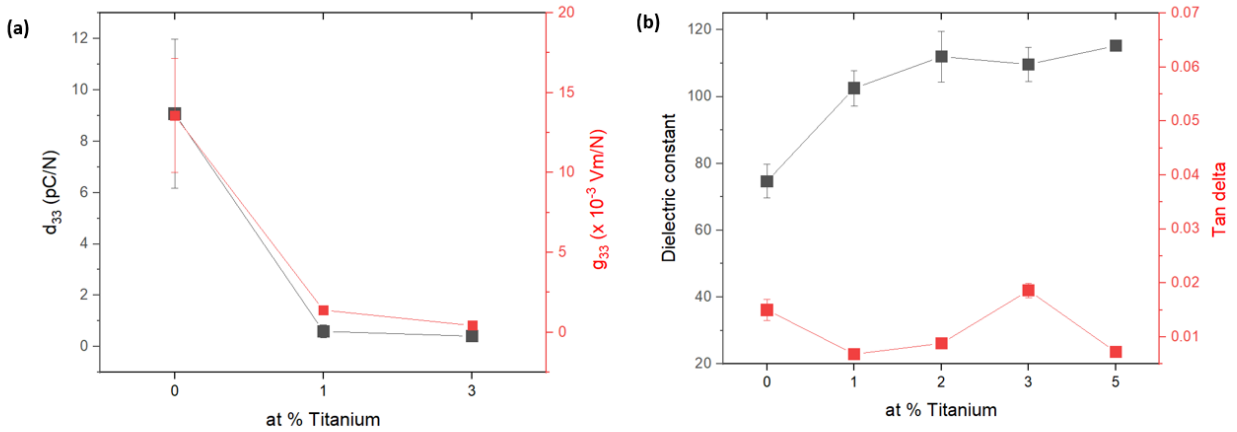

Figure 56 Variation of (a) dielectric constant and (b) d33 and g33 for different titanium-based BFO doping

Further studies on the optimization of sintering profile (sintering temperature and time) were performed to obtain titanium doped BFO with appreciable polarization. Figure 57(a) shows that increasing sintering temperature doesn't impact the PE loops. Sintering 5 at% Ti at higher temperature and for larger sintering time does cause opening of the loop at a high field of 115 kV/cm. However, Figure 57(c) shows there is still no domain switching (no peak in the current loop) before breakdown is reached.

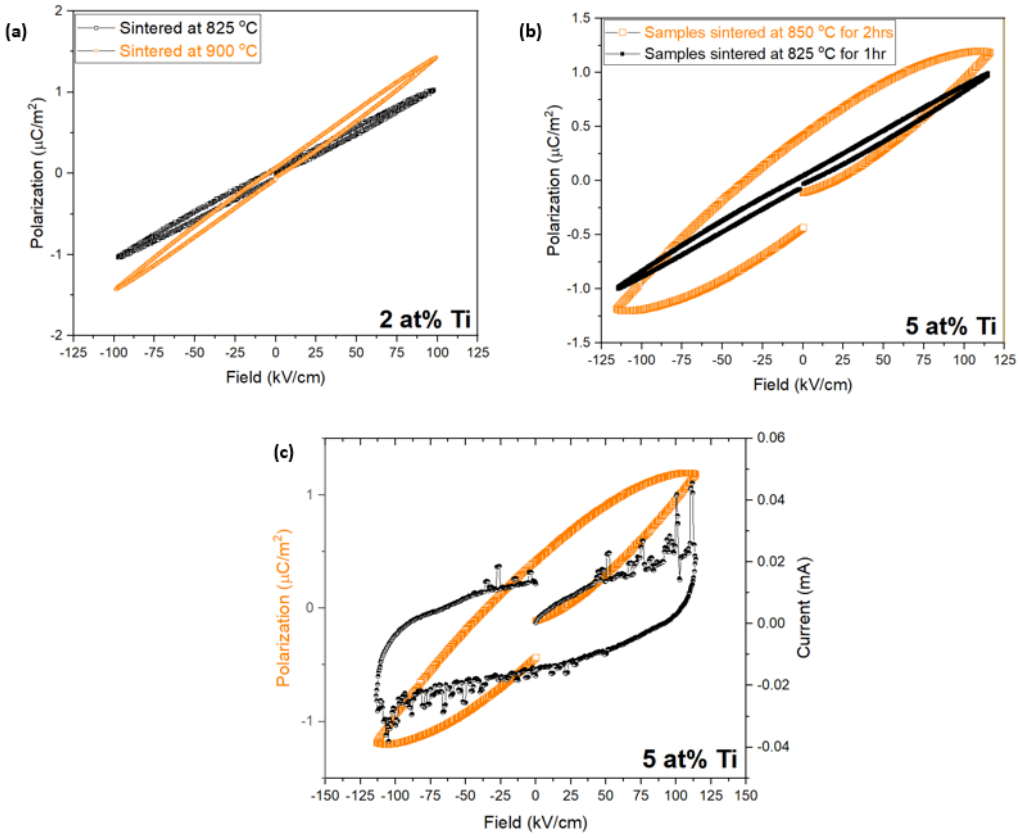

Figure 57 Variation of PE loops for (a) 2 at% Ti with changing sintering temperature (b) 5 at% Ti with changing sintering temperature and time (c) PE and CE loops for 5 at% Ti sintered at 850 °C for 2 hours

6.4 Cobalt-Titanium (Co-Ti)

From previous sections, it is clear that the introduction of cobalt improves the polarization while adding titanium leads to the enhancement of leakage characteristics. The next obvious step is to explore a co-doped system of cobalt and titanium to get the benefits of both the individual dopants. Figure 58 shows the PE hysteresis loops and current density curves for cobalt-titanium doped BFO samples sintered at 825 °C. The 0.25 at% cobalt-titanium (Co-Ti) system shows a pinched PE loop, similar to the one obtained for the cobalt-doped BFO systems in Chapter 6.2. Increasing the titanium content causes thinning of the loop, making it similar to the unopened and non-lossy loops obtained for titanium. Apart from imparting an appreciable polarization to the BFO samples, the 0.25-0.25 at% Co-Ti show excellent leakage characteristics with them performing as well as (or even better) the BFO samples at room temperature (Figure 58(b)).

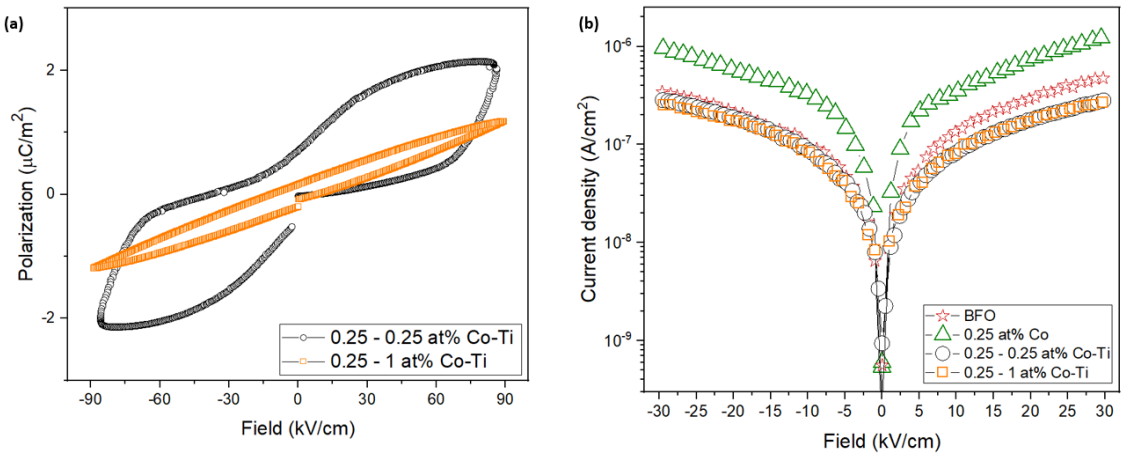

Figure 58 a) PE loops and (b) Current density for cobalt titanium co-doped BFO sintered at 825 °C

Figure 59(a-b) shows the variation of d_{33}, g_{33}, the dielectric constant, and loss tangents for the co-doped samples. The 0.25-0.25 at% Co-Ti shows d_{33} almost similar to the 0.25 at% cobalt system. The dielectric constant also increases with increasing titanium concentration. Incorporation of titanium allows poling at higher voltages, with the breakdown field of the samples increased with increasing titanium content. Samples poled at 100 kV/cm show the highest d_{33} and g_{33} out of all the cobalt and titanium doped systems explored in this study (Figure 58(c)).

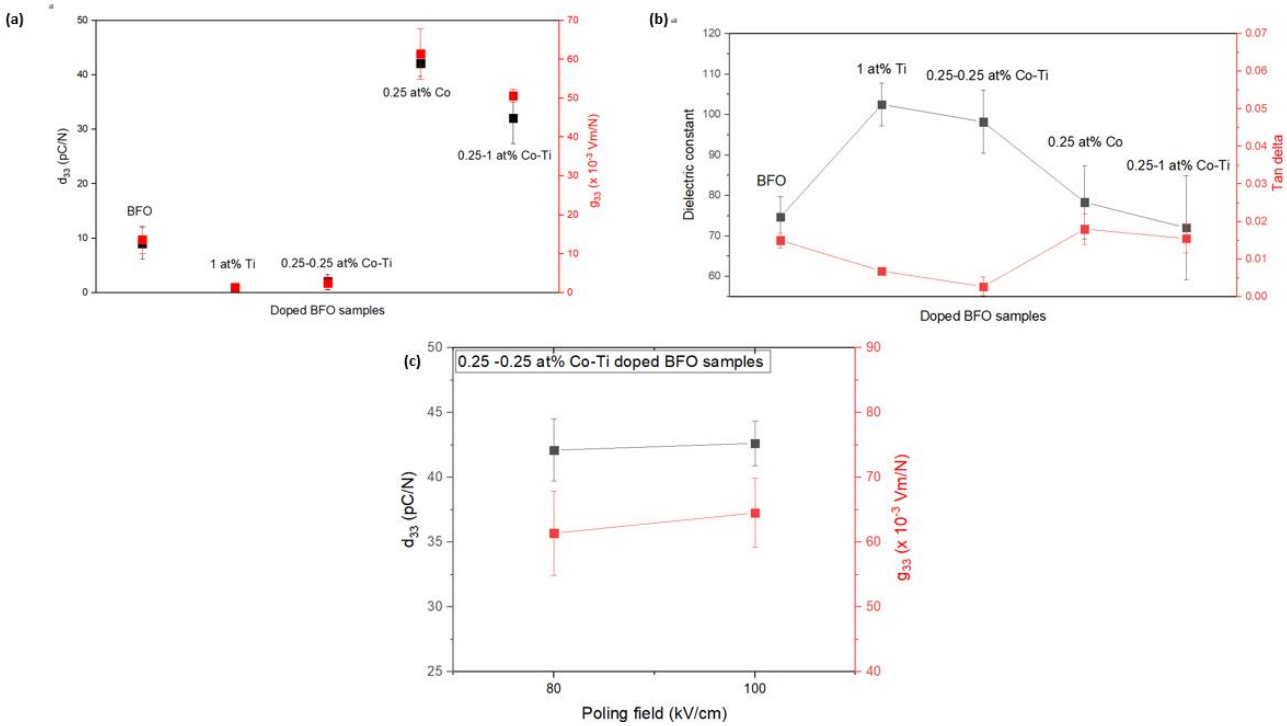

Figure 59 Variation of (a) d33 and g33 and (b) dielectric constant and tan delta for different cobalt titanium BFO doping and (c) d33 and g33 for 0.25-0.25 at% Co-Ti BFO doping at different polling fields

6.5 BFO-STO

Figure 60 shows the PE hysteresis loops and current density plots for the BFO-STO system, with the 30 at% STO sample showing the largest polarization. The large polarization at 30 at% STO is consistent with the literature, as the morphotropic phase boundary for the BFO-STO system has been reported to exist in the 30-40 at% STO range (59,61).

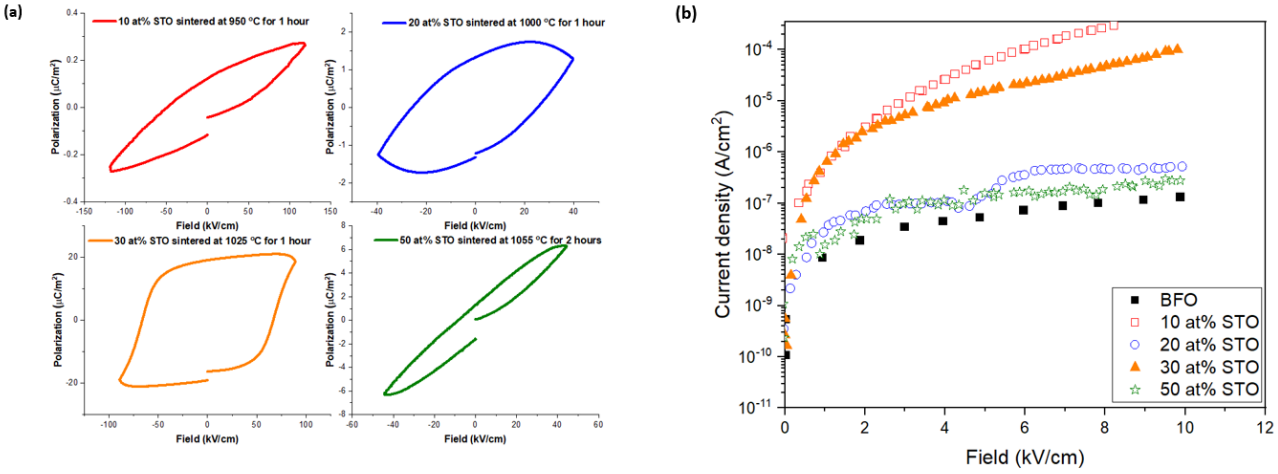

Figure 60 a) PE loops and (b) Current density for BFO-STO samples

The lossy PE loop at 10 at% STO can be due to the large amounts of bismuth in the sample (the sample is 90% BFO). The bismuth loss at high temperatures (>900 °C) along with some compositional inhomogeneity can be used to justify the poor PE loops. For 50 at% STO, the unopened loop can be attributed to the transition to a cubic structure that is non-ferroelectric (see Chapter 4.5). The poor PE loops for 20 at% STO may be due to the transition of the system to a pseudocubic phase. The 30 at% STO sample has the highest d_{33} out of all the doped systems explored in this study (see Figure 61). However, due to its large capacitance (and dielectric constant), the system exhibits a much lower g_{33} value.

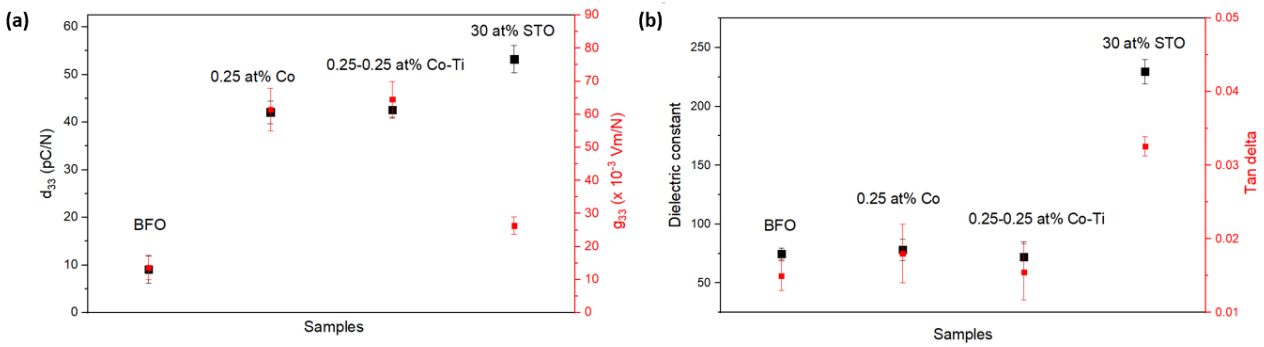

Figure 61 Variation of (a) d33 and g33 and (b) dielectric constant and tan delta for BFO-STO systems

Figure 62(a) shows the high temperature (100 °C) PE hysteresis loops for 30 at% STO samples. Higher temperature measurements lead to further enhancement of hysteresis loop along with reduction of the coercive field. A clear peak in the current loop denoting domain switching can

be seen in Figure 62(b) for the 30 at% STO sample. The square-shaped peaks in current loops are due to limitations in the PE analyser, which can overload at currents higher than 2.5 mA.

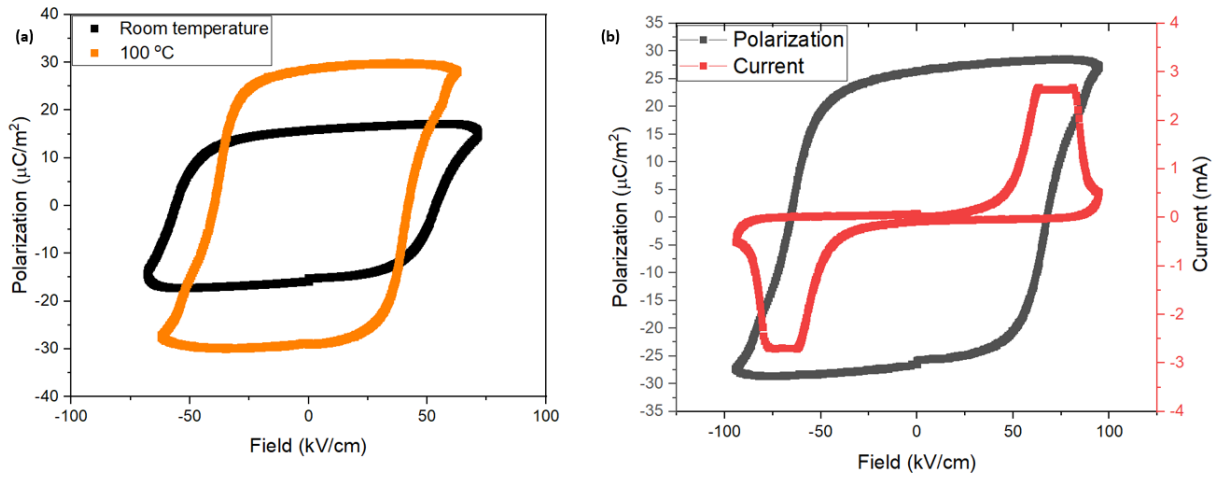

Figure 62 (a) High temperature (100 °C) PE loop and (b) Current loops for 30 at% STO

Chapter 7.

Broadband dielectric spectroscopy (BDS) results

Impedance spectroscopy is an important tool for ascertaining the dielectric properties of ceramic systems. This section highlights the AC conductivity, activation energy, dielectric losses, and permittivity of different dopant systems at a range of temperatures and frequencies. Additional Nyquist plots, Jonscher, and impedance fitting can be found in Appendix 10.2.

7.1 BFO

The AC conductivity plots presented in Figure 63(a) show the variation of conductivity with temperature. At higher temperatures, more mobile charge carriers and defects can be generated leading to an increase in conductivity. The conductivity also rises with frequency, which can be associated with the increased hopping of charge carriers (76,77). Figure 63(b-c) shows the variation of real permittivity and loss tangent with frequency at different temperatures. The permittivity rises with temperature due to the larger amount of mobile charge carriers present in the system. The larger amount of charge carriers and defects with increasing temperature also contribute to the large dielectric losses.

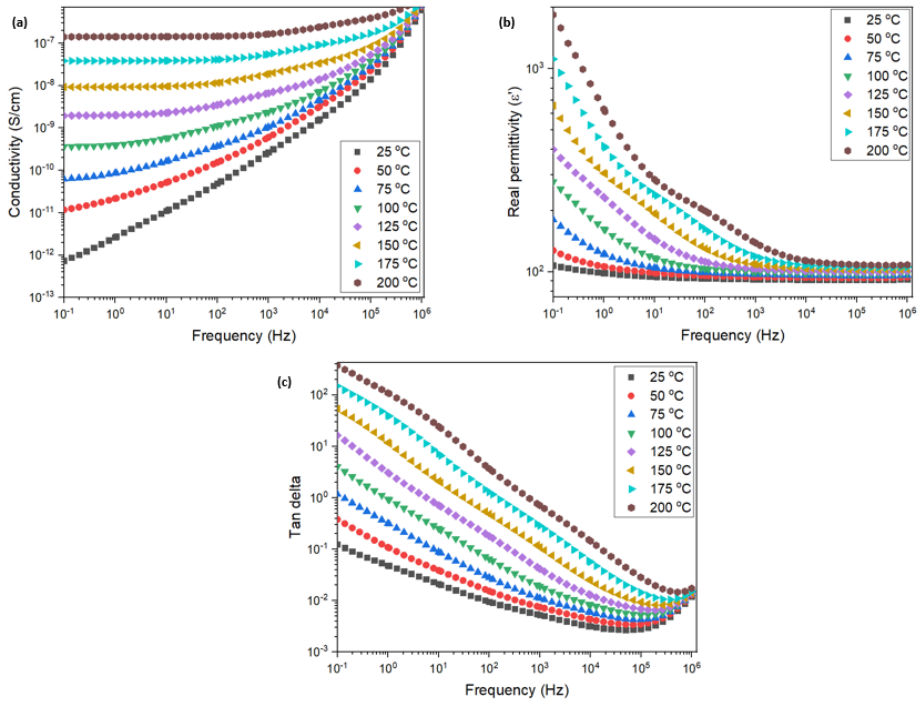

Figure 63 Variation of (a) real part of conductivity (b) real permittivity and (c) loss tangent with frequency at different temperatures for BFO

Nyquist plots are a complex impedance plot of the real part (Z') to the imaginary part of the impedance (Z''). The shape of the Nyquist plots indicates the different contributions (bulk,

grain boundary, defects, and electrode interface) to the total conductivity. The existence of a perfect semicircle relates to an ideal Debye type relaxation behavior and is generally a characteristic of a homogenous material (78). The Nyquist plots show a singular semicircle (see Figure 64(a))) for the selected temperature range. The singular semicircle denotes the single contribution (bulk contribution) to the conductivity for the undoped BFO system. The semicircles also exhibit decreasing radii with increasing temperature, which coincides with the diminution in resistance. The activation energy is obtained from the slope of the Arrhenius plot shown in Figure 64(b). The activation energy fitting is done with two slopes as the Arrhenius plot (Figure 64(b)) is not completely linear. The choice to plot two activation energies also provides some consistency throughout this discussion (as explained later on in Chapter 7.2).

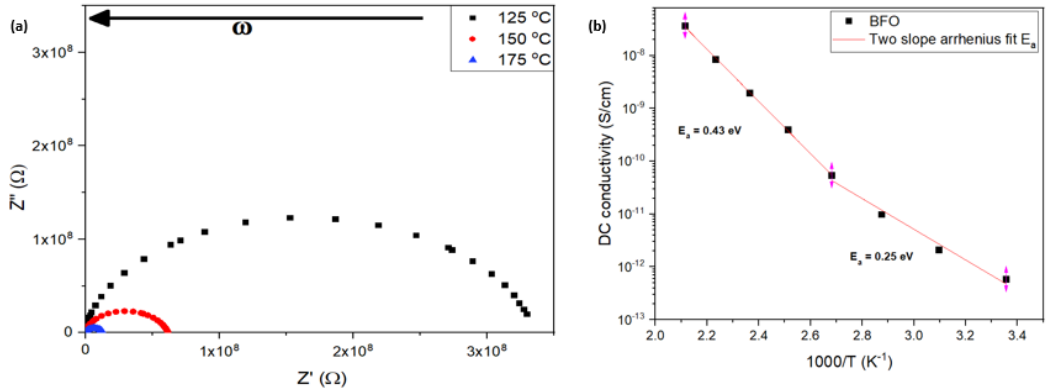

Figure 64 (a) Nyquist plots for 125, 150, and 175 °C and (b) Activation energy, for BFO

7.2 Cobalt

The AC impedance analysis (Nyquist and complex impedance vs frequency plots) for the 3 at% cobalt doped BFO (given in Figure 65 below), shows the presence of two distinct semicircles. As mentioned before, the presence of multiple semicircles in the Nyquist plot implies that the electrical characteristics are influenced by more than one mechanism (69). This non-ideal behavior can be attributed to a variety of factors such as grain boundaries, doping-induced defects, grain orientations, and sample inhomogeneities (79). Further evidence for the multiple relaxation mechanisms can be seen from the complex impedance vs frequency plots given in Appendix 10.2.

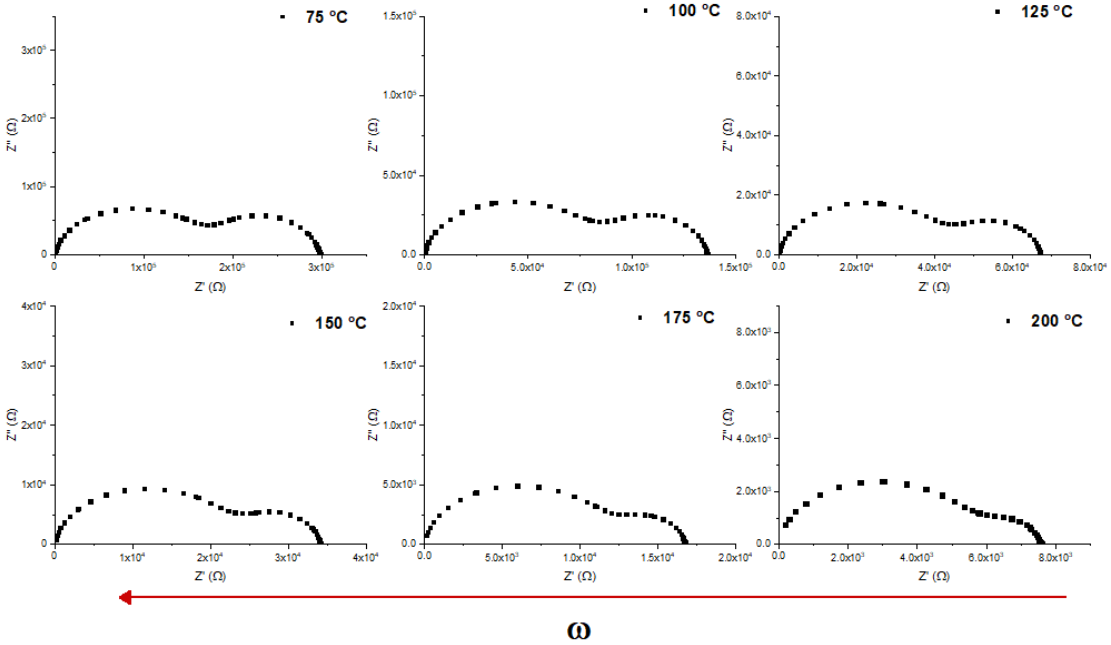

Figure 65 Nyquist plots for 3 at% Co at different temperatures

Initially, the presence of secondary peak was thought to be associated with the possible cobalt segregation at the grain boundaries. High-resolution energy-dispersive X-ray spectroscopy (EDS) was further performed to investigate the cause of this observed secondary peak in the impedance data. However, the EDS data (given below in Figure 66 and Table 2) did not indicate any grain boundary enrichment. Moreover, the sample was found to be highly inhomogeneous with the presence of bismuth-rich and iron-cobalt complexes. From Figure 66(b) clear Co-Kα and Co-Kβ peaks can be seen for spots 4 and 7, indicating Fe-Co rich regions (iron-cobalt complexes). The presence of the secondary peak in the impedance data may thus be attributed to material inhomogeneities. For more details on the EDS data refer to Appendix 10.2.4

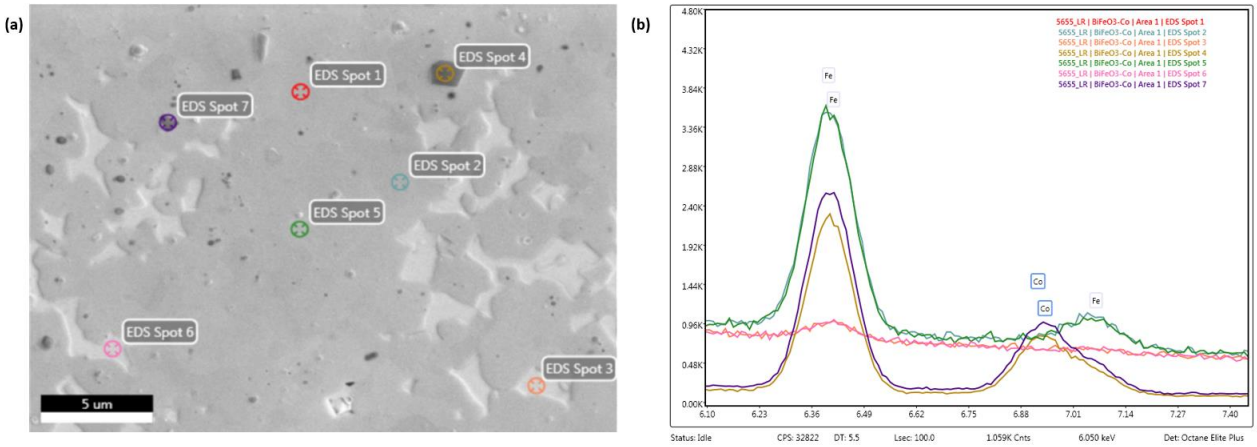

Figure 66 (a) EDS measurements at seven spots for 3 at% Co (b) Presence of Co-Kα and Co-Kβ peaks

Table 2 Summary of EDS results

EDS spot	O-K (at %)	Fe-L (at %)	Co-L (at %)	Bi-M (at %)	Phase
1	65.60	7.60	0	23.75	$Bi_{12}Fe_4O_{33}$ (Bismuth rich)
2	63.01	7.65	0	23.08	$Bi_{12}Fe_4O_{33}$ (Bismuth rich)
3	47.00	0	0	36.13	Bi_2O_3 (Bismuth oxide)
4	76.20	17.28	6.25	0	$Fe_{1.8}Co_{1.2}O_4$ (Iron-cobalt complex)
5	81.45	18.55	0	0	FeO_2 (Iron oxide)
6	46.02	0	0	36.20	Bi_2O_3 (Bismuth oxide)
7	75.89	16.23	5.82	2.06	$BiFe_8Co_3O_{38}$ (Bismuth-iron-cobalt complex)

As mentioned previously, in Chapter 2.7, a set of two parallel RC circuits connected in series have been used to model the individual contributions (bulk and material inhomogeneity). To avoid confusion, these secondary contributions due to material inhomogeneities will be addressed with the abbreviated SC throughout the remaining text. The capacitance and resistance of these two components for 3 at% Co at different temperatures is plotted in Figure 67 below. There is a decrease in resistance with increasing temperature which is in agreement with the decreasing radii of the Nyquist plots at higher temperatures.

Figure 67(a) shows the variation of the bulk and SC resistance with temperature. The slopes of the bulk and SC contributions are similar in magnitude, implying that these two components have a similar contribution to the overall conductivity. Further investigation and more in-depth analysis for the cobalt dopant case is required. From the impedance plots, we know for certain that there are multiple contributions to the overall conduction. How distinct these contributions are and how they individually affect the overall conductivity is still largely unknown.

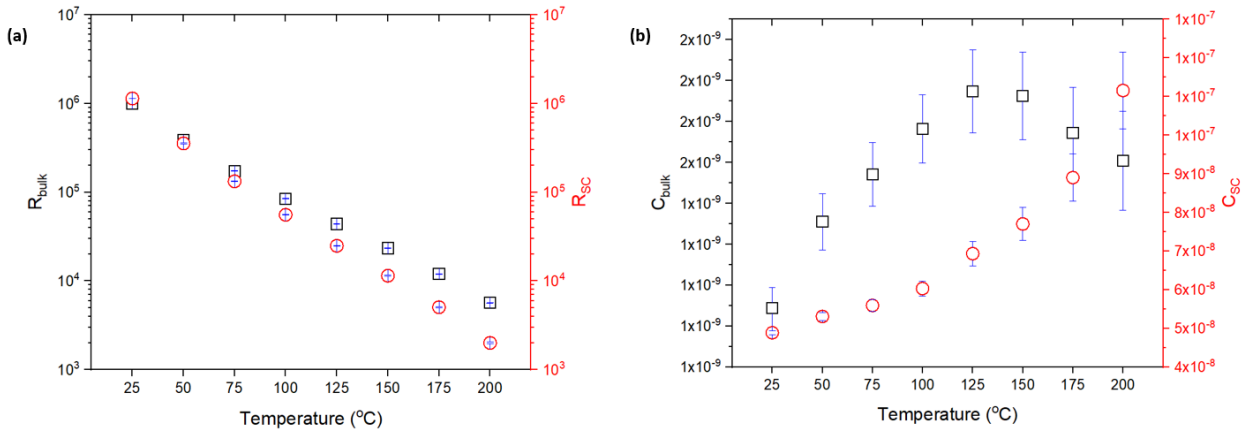

Figure 67 Variation of (a) resistance and (b) capacitance of two components for 3 at% Co

Plotting for activation energy is thus done with slopes for two intermediate temperature stages (25 to 100 °C and 100 to 200 °C). Figure 68(b) shows the increase in conductivity with cobalt doping in BFO. This increase can be attributed to the substitution of Co^{2+} into the lattice, which acts as an acceptor dopant for BFO. As a result of charge recompensation, oxygen vacancies are created which will contribute to the conductivity. The magnitude of the bulk and SC-derived activation energies along with their variation with dopant concentration is shown in Figure 68(c). The difference in the two activation energies decreases with increasing cobalt concentration.

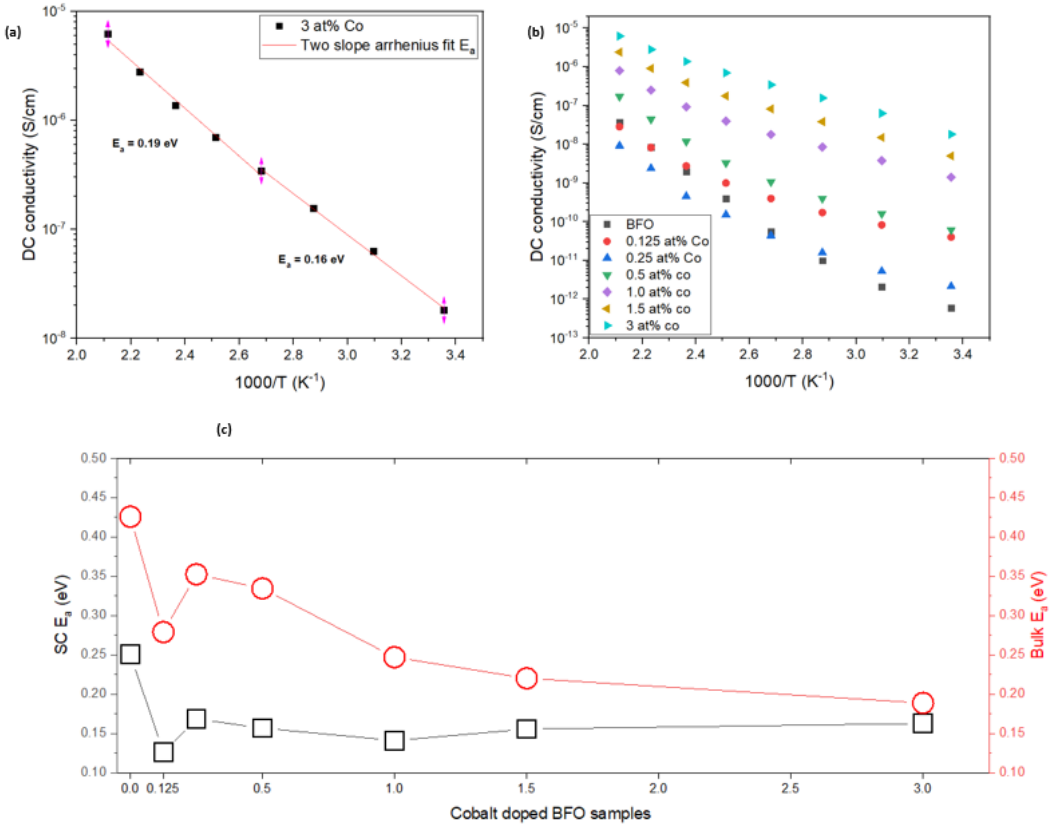

Figure 68 (a) Activation energy fit with two slopes (b) Variation of DC conductivity for cobalt doped BFO with varying temperatures (c) Variation of activation energy for cobalt doped BFO

Figure 69 shows the variation of real permittivity with frequency at different temperatures for a cobalt-doped BFO sample (0.5 at% Co). In the low-frequency region, real permittivity increases drastically with temperature, which is due to dielectric dispersion caused by charged species in the system (defects and charge carriers). This low-frequency dispersion is traditionally associated with hopping conduction (the movement of charge carriers within the system) (21). At lower temperatures, the dipoles are stationary due to space charge relaxation at the interface, leading to lower magnitudes of dielectric constant at low temperatures. As the temperature increases, the number of charges injected into the system increases, leading to an increase in the dielectric constant. The large value of dielectric constant at a lower frequency can also be attributed to the defect-induced dipoles, which are easily able to reorient themselves with the application of current. At higher frequencies, these dipoles lag behind the applied electrical field, leading to the development of a plateau region (77). The loss tangent curve also shows an increase with increasing temperature, which is expected, as, at higher temperatures, there are a large amount of thermally activated charge carriers and other defects which will lead to more losses. Due to the presence of these charge carriers, the conductivity will be higher at these temperatures. Hopping conduction can be assumed as the dominant relaxation mechanism. Maxwell-Wagner type conduction can be ruled out, as the characteristic step-wise peak in tan delta with increasing frequency is absent (14).

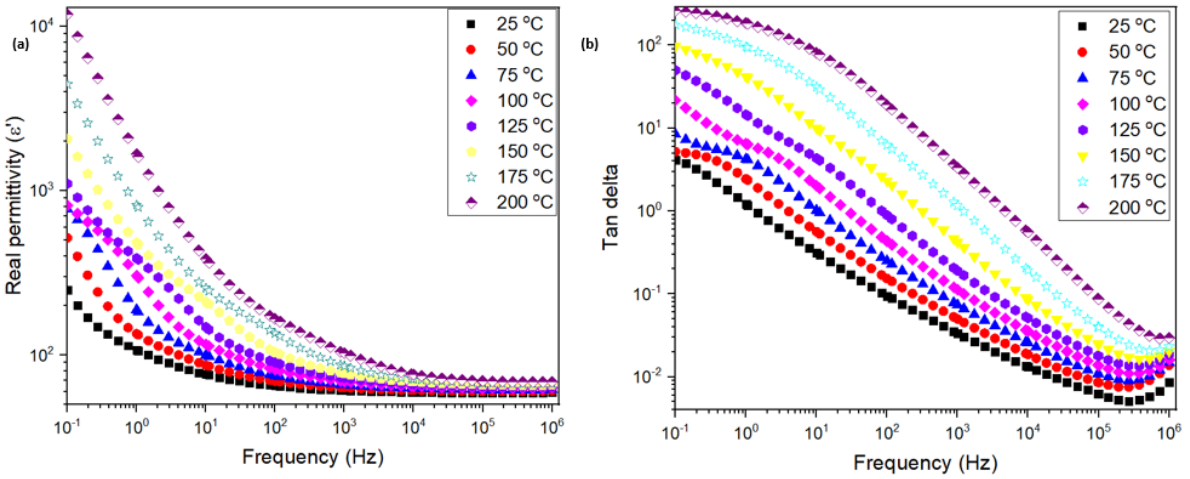

Figure 69 Variation of (a) real part of permittivity and (b) loss tangent with frequency at different temperatures for 0.5 at% Co

7.3 Titanium

An analysis of the Nyquist plots for titanium doped BFO (for 1 at% Ti, given in Figure 70 below) shows a singular semi-circle in the measured frequency range. However, the activation energy fitting is done with two slopes similar to how it was done in the previous sections. From the activation energy plots shown in Figure 71(a,c), an increase in the activation energy with titanium doping of BFO can be observed.

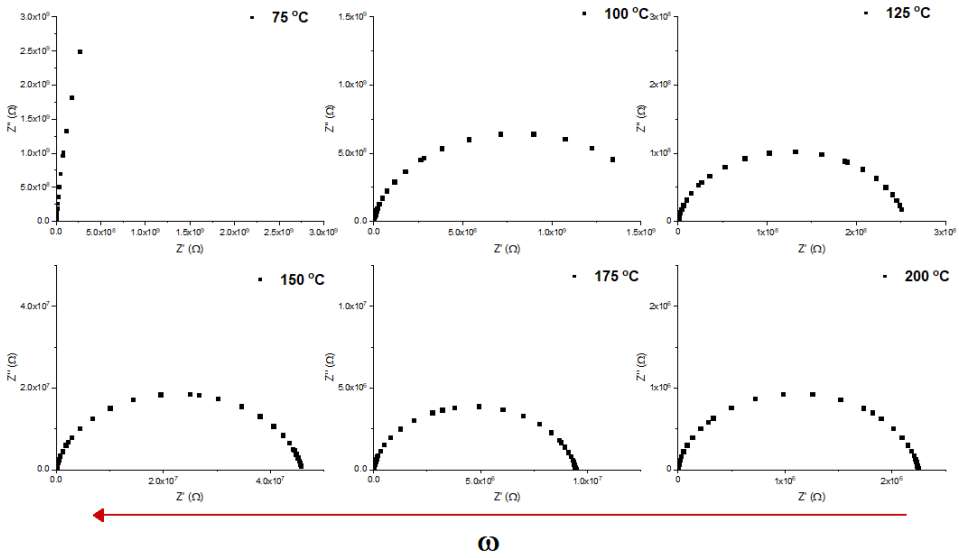

Figure 70 Nyquist plots for 1 at% Ti at different temperatures

Titanium doped BFO shows low conductivity at room and elevated temperatures due to the suppression of oxygen vacancies as a result of the introduction of the Ti^{4+} ion onto the B-site of the perovskite. From Figure 71(b), the value of conductivity for titanium doped samples is close to that of the undoped BFO. The 1 at% Ti shows lower conductivity than BFO at temperatures as high as 200 °C. The room temperature current density measurements shown in Chapter 6.3 (Figure 55(b)) provide further evidence of the excellent leakage characteristics imparted on BFO as a consequence of titanium doping

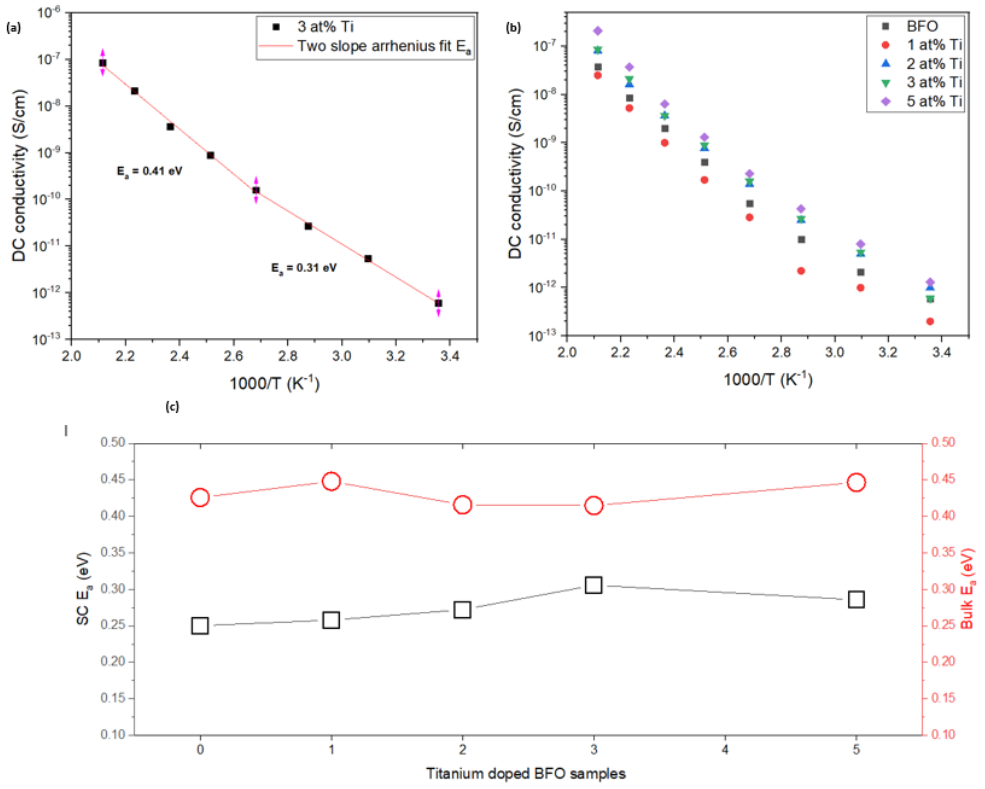

Figure 71 (a) Activation energy fit with two slopes (b) Variation of DC conductivity for titanium doped BFO with varying temperatures (c) Variation of activation energy for titanium doped BFO

7.4 Cobalt-Titanium (Co-Ti)

The cobalt-titanium co-doped system was explored to combine the characteristics of the highly polarizable cobalt systems with the low leakage titanium doped BFO systems Figure 72(a) shows the DC conductivity of titanium cobalt co-doped BFO system with varying temperatures. The data given in this plot along with the results from room temperature current density measurements presented in Chapter 6.4 (Figure 58(b)) prove that conductivity is reduced at both room and elevated temperatures due to co-doping. Increasing titanium concentration (from 0.25 to 1 at%) further reduces the conductivity of the system. The 0.25-0.25 at% Co-Ti system may prove to be an excellent candidate for high-temperature applications due to its excellent polarizability and low conductivity at a range of temperatures. The permittivity and loss tangent (Figure 72(b-c)) follow similar trends as described in the previous sections.

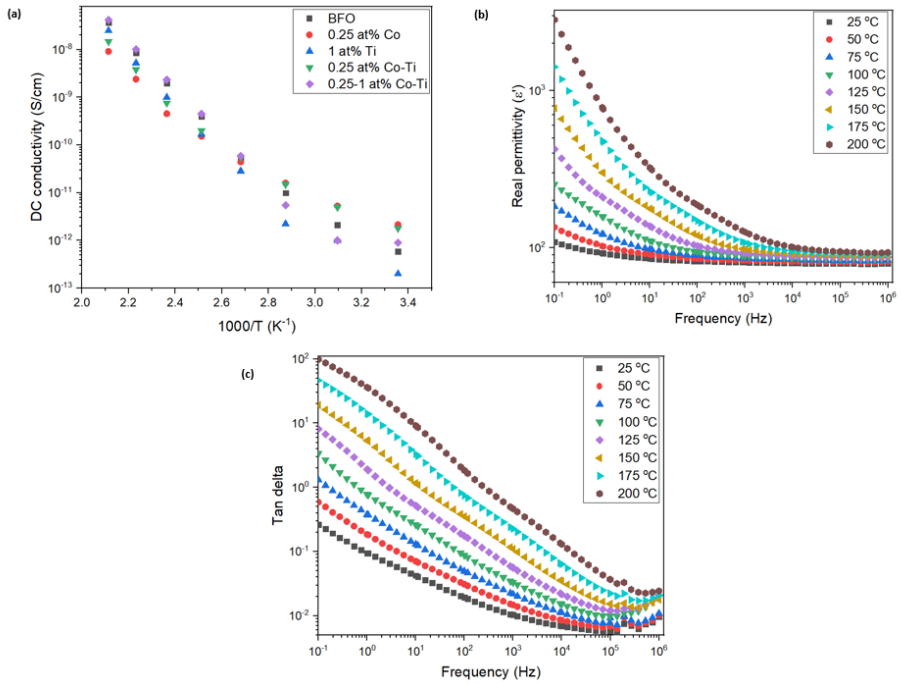

Figure 72 (a) Variation of DC conductivity b) Real permittivity and (c) tan delta for cobalt-titanium doped BFO

The Nyquist plots for 0.25-0.25 at% Co-Ti displayed in Figure 73(a) show a single semicircle corresponding to bulk contribution to electrical conduction. There's an increase in the activation energy with increasing titanium concentration (see Figure 73(c)). This is in conjunction with the decreased conductivity of the samples due to titanium incorporation.

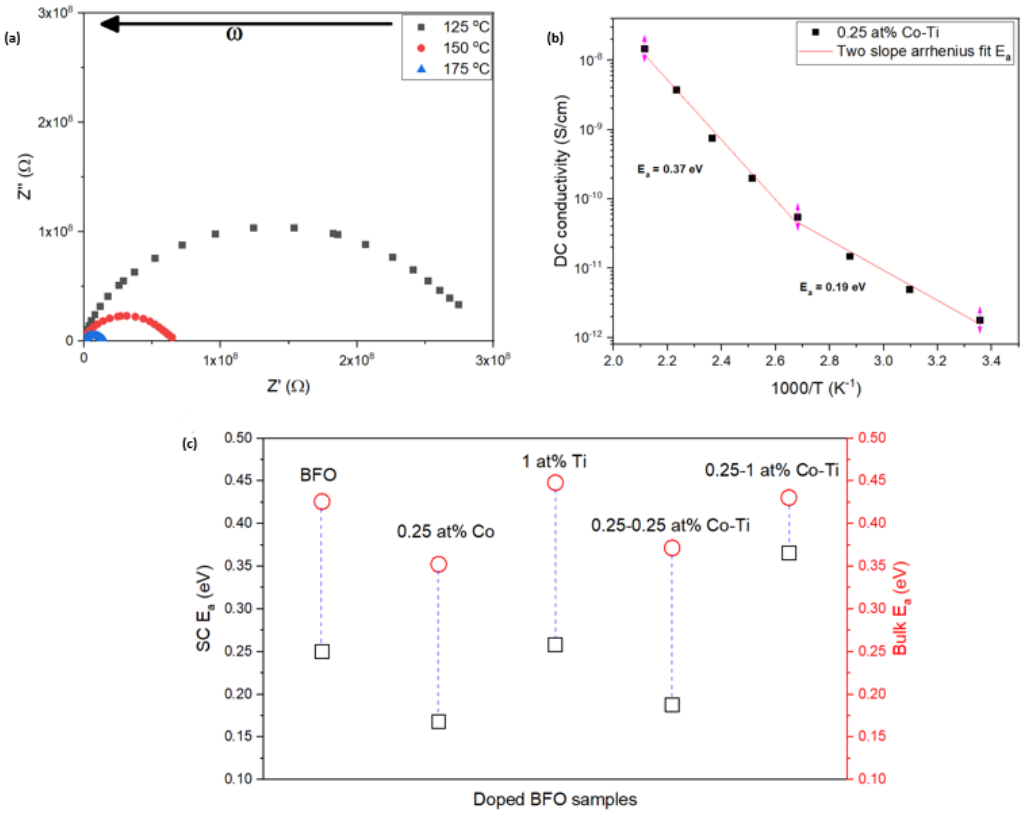

Figure 73 (a) Nyquist plots for 0.25-0.25 at% Co-Ti BFO samples at different temperatures (b) Activation energy fit with two slopes (c) Variation of activation energy for cobalt-titanium doped BFO

7.5 BFO-STO

Before diving into any discussion on the dielectric properties of BFO-STO, it has to be noted that, unlike the cobalt and titanium doped systems, individual BFO-STO systems have different sintering profiles (for detailed explanation on the profiles, visit chapter 3.3 Calcination and sintering profiles). Changing sintering parameters like sintering temperature, time, cooling-heating rates, along with phase composition (10 to 50 at% STO) will impact the defect chemistry and strongly influence the properties under discussion. Keeping these factors in mind, this section attempts to highlight some interesting characteristics observed in the BFO-STO solid solution system.

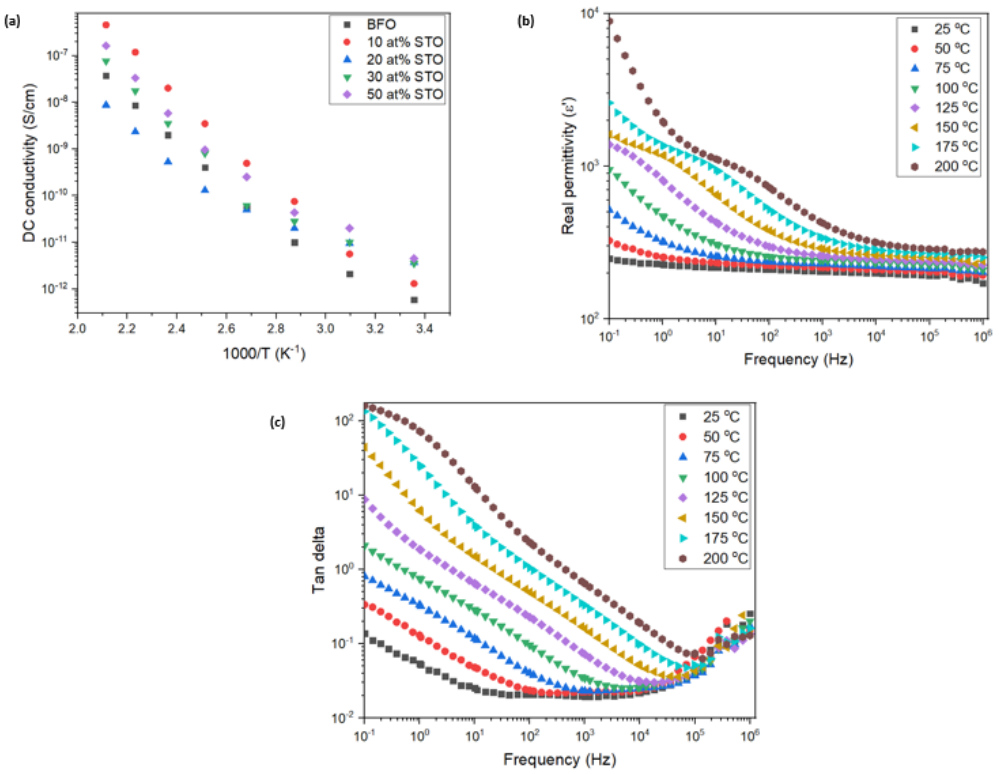

Figure 74 Variation of DC conductivity for BFO-STO systems, (b) Real permittivity and (c) tan delta for 30 at% STO samples

The variation of conductivity at different temperatures for the BFO-STO system is shown in Figure 74(a). The incorporation of STO leads to the system becoming more conductive, which is in agreement with the literature (60). However, there are some irregularities at higher temperatures. 10 at% STO experiences a drastic increase in conductivity at higher temperatures. This can be attributed to the major bismuth phase (sample is 90 at% BFO) being unstable at temperatures above 900 °C (sample sintered at 950 °C). Another interesting observation is 20 at% STO having lower conductivity than phase pure BFO at elevated temperatures. This anomalous behavior could be due to some phase change or may be related to the increased porosity of the sample. The permittivity and loss tangent show the expected response with varying temperature and frequency (see Figure 74(b-c)).

A summary of the DC conductivity of the different doped BFO systems at room and elevated temperatures (200 °C) is presented in Table 3. Titanium and cobalt-titanium co-doped systems show similar and, in some cases (1 at% Ti), lower magnitudes of conductivity than BFO. Titanium doped (donor) samples exhibit lower conductivity than the cobalt (acceptor) doped samples. The cobalt titanium co-doped system exhibits a low magnitude of conductivity which is decreased even further with increasing titanium loading from 0.25 to 1 at%. The BFO-STO solid solutions show higher values of conductivity than pure BFO.

Table 3 Room and high-temperature DC conductivity for different BFO doped systems

Sample	Room temperature DC Conductivity (25 °C) (S/cm)	High-temperature DC Conductivity (200 °C) (S/cm)
BFO	5.5×10^{-13}	3.7×10^{-8}
0.125 at% Co	4.0×10^{-11}	2.8×10^{-8}
0.25 at% Co	2.2×10^{-12}	9.2×10^{-9}
0.5 at% Co	6.2×10^{-11}	1.7×10^{-7}
1 at% Co	1.4×10^{-9}	7.9×10^{-7}
1.5 at% Co	5.0×10^{-9}	2.4×10^{-6}
3 at% Co	1.8×10^{-8}	6.2×10^{-6}
1 at % Ti	2.0×10^{-13}	2.5×10^{-8}
2 at % Ti	1.0×10^{-12}	8.1×10^{-8}
3 at % Ti	6×10^{-13}	8.6×10^{-8}
5 at % Ti	1.3×10^{-12}	2.1×10^{-7}
0.25-0.25 at% Co-Ti	1.8×10^{-12}	1.5×10^{-8}
0.25-1 at% Co-Ti	9.0×10^{-13}	4.2×10^{-8}
10 at % STO	1.3×10^{-12}	4.5×10^{-7}
20 at % STO	3.7×10^{-12}	8.7×10^{-9}
30 at % STO	3.5×10^{-12}	7.6×10^{-8}
50 at % STO	4.5×10^{-12}	1.6×10^{-7}

Chapter 8.

High-temperature measurements

From the previous sections, we have established that the 0.25-0.25 at% Co-Ti and 30 at% STO systems show excellent properties. They possess high d_{33} values and the data from the BDS measurements (see Chapter 7) along with the high-temperature PE hysteresis loops (for 30 at% STO, Chapter 6.5) suggest that these systems can be applied for high-temperature applications. This chapter highlights an *in-situ* experiment for ascertaining the high-temperature response of our doped BFO systems. The high-temperature response of the 0.25-0.25 at% Co-Ti and 30 at% STO systems is measured and compared with the response of undoped BFO.

Figure 75 shows the high-temperature setup used for the measurements. The copper plate and the oscilloscope wires which form the two terminals of the sensor are soldered at 450 °C. A metal ball is dropped from a set height (400 mm) onto the cantilever strike plate. The voltage response generated due to the vibrations caused by the impact of dopped ball is collected and analyzed by the oscilloscope. A hot plate is used to get measurements at a variety of temperatures ranging from 25 °C to 200 °C. The hot plate is covered with aluminium foil for shielding. Five measurements are taken at each temperature; the mean values of the response and the standard deviation are used for further analysis.

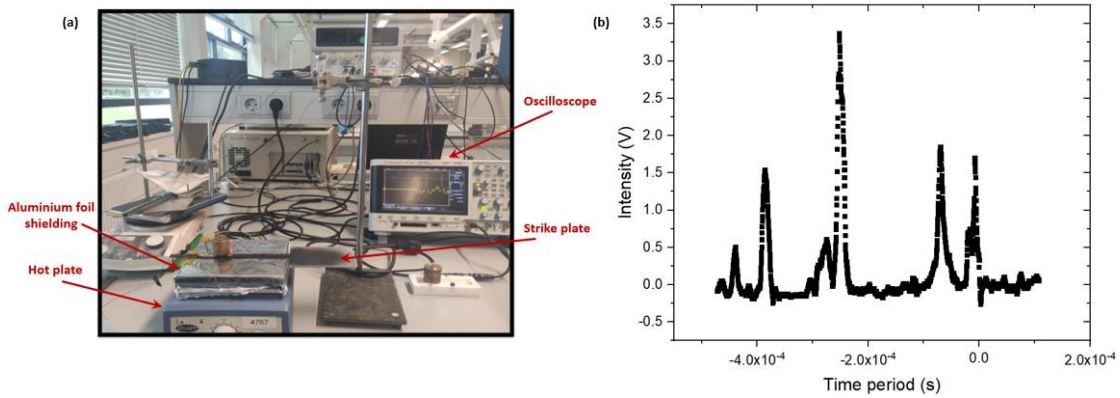

Figure 75 (a) High-temperature measurement setup (b) Voltage response for 30 at% STO sample

Figure 76 (a-c) shows the intensity of the signals at different temperatures for the three samples. There is a drop in the signal intensity with increasing temperatures for both the BFO and the 0.25-0.25 at% Co-Ti systems. However, there is a clear enhancement of the voltage response for the 30 at% STO system at higher temperatures. This enhanced high-temperature voltage response coupled with the excellent high-temperature PE loop of 30 at% STO proves its viability for high-temperature sensing systems.

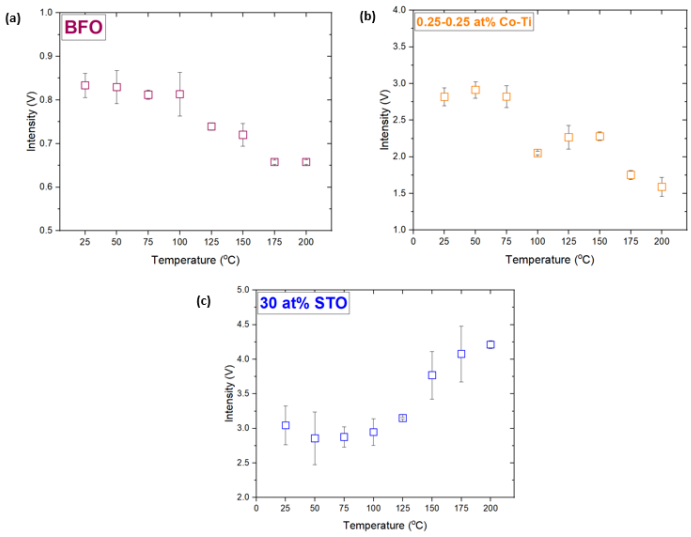

Figure 76 Voltage response measured from the oscilloscope for (a) BFO, (b) 0.25-0.25 at% Co-Ti and (c) 30 at% STO

An effective charge constant value has been calculated by multiplying the voltage response from the oscilloscope with the dielectric constant values at 1 kHz for different temperatures (obtained from the BDS). Figure 77(a-c) shows the variation of this effective charge constant with temperature. There is a clear improvement in high-temperature performance for the 30 at% STO system. The scatter in the effective charge constant values for the BFO and the 0.25-0.25 at% Co-Ti systems can be attributed to the large variations in the voltage response. Since this effective charge constant has been defined as a product of the oscilloscope voltage response and the dielectric constant, an abrupt change in the values of the voltage will cause a variation in the value of the effective charge constant.

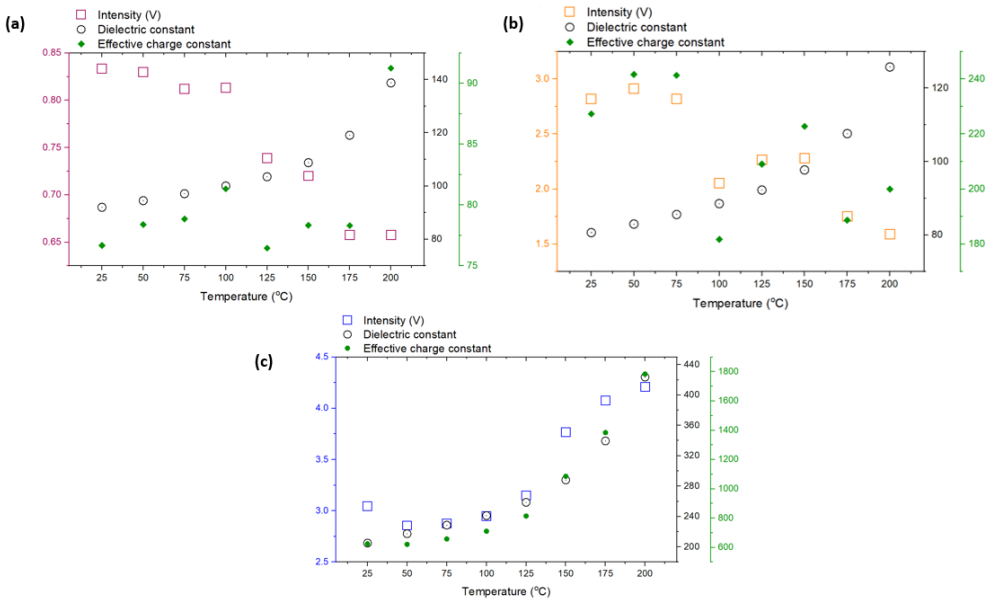

Figure 77 Variation of the voltage response, dielectric constant, and effective charge constant with temperature for (a) BFO, (b) 0.25-0.25 at% Co-Ti and (c) 30 at% STO

Chapter 9.

Conclusion and recommendations

Bismuth ferrite (BFO) is an exciting piezoelectric material that has the potential to be a viable PZT replacement. However; the presence of secondary parasitic phases and its large electrical conductivity makes the widescale utilization of BFO difficult. The primary aim of this thesis is to achieve high polarization and low leakage characteristics in BFO via doping. To achieve this objective, the incorporation of cobalt and titanium dopants into BFO has been studied in detail. A solid solution of BFO with strontium titanate (STO) has also been explored.

The opening phase of this study deals with synthesis optimization with respect to the amount of binder added and the pressure applied for the formation of the pellets. The results from the binder optimization study indicated good relative density (≈ 95 %) and low dielectric losses (< 3 %) for samples with low binder concentrations. Pressure optimization studies showed optimum results for samples pressed with 3 and 5 tonne pressing forces. A combination of 4 wt% binder concentration and a 3-tonne pressing force (≈ 320 MPa) was selected as the profile for the synthesis of all future samples.

The first batch of experiments was aimed at making phase pure BFO. BFO was synthesized by calcining and sintering at 775 °C. Rietveld refinements on the sintered sample showed the presence of a primary R3c perovskite phase along with the formation of some iron and bismuth-rich parasitic phases (≈ 4 %). The sintered samples exhibited high relative density (≈ 95 %) and the SEM micrographs showed a uniform grain structure. The polarization vs electric field (PE) hysteresis loops showed an unsaturated and unopened response. Poling the sample at 80 kV/cm at room temperature, yielded minute values of the piezoelectric charge constant (d_{33}≈ 8 pC/N). BDS measurements of the prepared BFO showed very small values of the conductivity (≈ 6 x 10^{-13} S/cm) at room temperature.

The next phase dealt with the B-site doping of BFO with cobalt and titanium. These dopants were chosen based on the literature, with cobalt doped BFO showing improved polarization while titanium doped BFO showing reduced conductivity. A similar sintering profile (825 °C) was selected for all the doped samples for the sake of consistency and ease of comparison between different systems

The introduction of a trace amount of cobalt into BFO led to a massive increase in the d_{33} of the sample. The addition of cobalt also led to increased conductivity and higher leakage due to the formation of oxygen vacancies. At higher dopant concentrations (≥ 1 at%) the increase in the leakage was massive and the samples could not be poled effectively. The Nyquist and complex impedance vs frequency plots showed the formation of two distinct peaks (semicircles for Nyquist) implying two distinct contributions to the overall conductivity. High-resolution EDS studies on the 3 at% Co system confirmed the presence of inhomogeneities in the sample. The resistance of these two components obtained from complex impedance modelling (bulk and SC) showed almost similar activation energies which imply that they have a similar contribution to the overall conductivity. Further investigation into the cause of these peaks has to be undertaken to get a more in-depth insight into the overall phenomena.

Titanium doping of BFO was successful in reducing the leakage however poling of titanium doped samples proved to be difficult; with the poled samples showing a non-appreciable d_{33} value. From the BDS measurements, titanium samples showed DC conductivity similar to that of undoped BFO, with the 1 at% Ti-doped sample possessing lower conductivity values at room and high temperatures. The reduced conductivity and improved leakage can be attributed to a reduction of oxygen vacancies as a result of Ti^{4+} substitution at the B-site of the perovskite. The reduction in oxygen vacancies is also supported by the SEM micrographs which show a reduced grain size with titanium doping (due to lower oxygen ion movement leading to lower grain growth). The lattice parameters obtained from profile matching showed that doping BFO with cobalt and titanium led to a non-appreciable change in the lattice parameters.

Further exploration of a co-doped system of cobalt-titanium was done to combine the desired characteristics of the individual dopants. BFO was doped with trace amounts of cobalt and titanium (0.25 at% each of Co and Ti) and the system formed showed excellent leakage characteristics and very high d_{33} values. Incorporation of titanium allowed poling of samples at higher fields.

A study on the solid solution of bismuth ferrite and strontium titanate (STO) was done, to obtain high piezoelectric properties by incorporating a morphotropic phase boundary (which has been reported in the range of 30-40 at% STO). The 30 at% STO system showed excellent piezo properties with an average d_{33} of 53 pC/N. The XRD plots show a transition from a rhombohedral structure to a cubic structure with increasing STO concentrations. The structural transition can be seen as early as the 20 at% STO system, where the dual [104] and [110] peaks start merging implying the formation of some pseudocubic phase.

At the end of the study, some in-situ high-temperature results are provided. The high-temperature setup used is novel and is still being optimized. However, some basic measurements obtained from the setup can still provide an insight into the piezoelectric response of our systems at high temperatures. Our BFO sample showed a decreased voltage response with increasing temperature. The 0.25-0.25 at% Co-Ti exhibited some variations but overall, it showed a similar drop with temperature. The 30 at% STO system however showed an increased response with rising temperature proving its viability for high-temperature applications.

The results obtained in this study are very interesting, but there are certain avenues that we couldn't explore due to time restrictions. This paragraph will highlight some of our recommendations and point out areas of research that can be explored further. Optimization of corona poling for small ceramic samples (such as our BFO) is an interesting field to explore. More homogenous field distribution in the corona setup would allow for poling a larger amount of our samples in a shorter time. Performing XRD measurements before and after poling to see any change in the structure of our samples (for samples that show a large d_{33} value). Further investigation to ascertain the nature of the secondary peaks in the impedance measurements. Performing high-resolution transmission electron microscopy (HRTEM) on the cobalt doped samples. Exploration of high-temperature poling of BFO-STO systems. Our results show that the 30 at% STO system performs admirably well at high temperatures which necessitates conducting further high-temperature studies. Lastly, optimization of the high-temperature *in-situ* experiment setup is required. The systems need to be clamped better to not allow for lateral

movement of the strike plate. The aluminium foil which is used for shielding also expands at high temperatures which can cause problems during measurement.

To conclude, we have successfully managed to develop a system with low leakage and higher polarizability by co-doping BFO with trace amounts of cobalt and titanium. We have also devised a solid solution system that shows extremely high d_{33} values and offers enhanced performance at high temperatures. Figure 78 below gives a graphical summary of the most important result of our doped BFO systems.

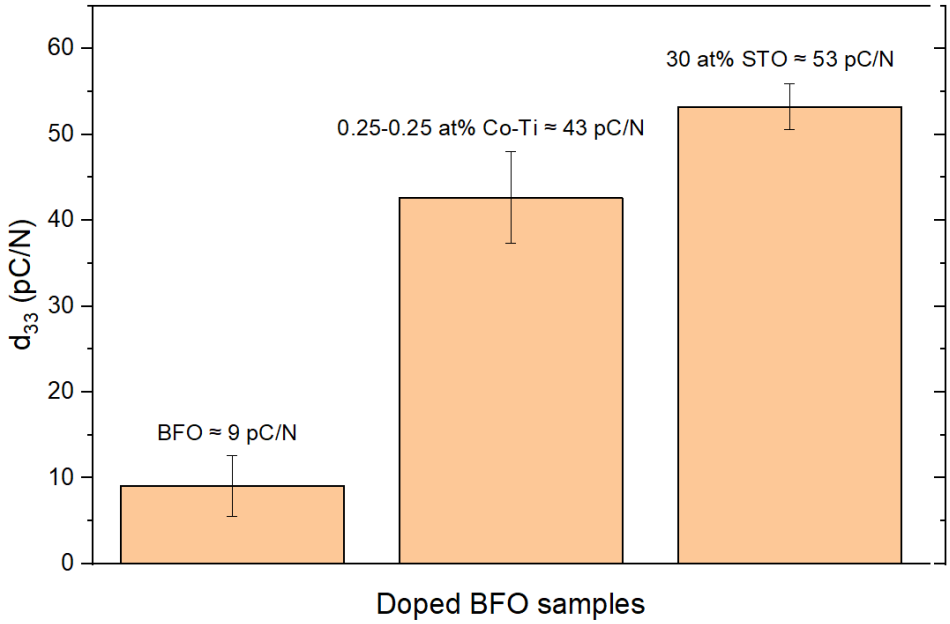

Figure 78 d_{33} values for the BFO, 0.25-0.25 at% Co-Ti and 30 at% STO systems

Chapter 10.

Appendix

10.1 XRD data- full pattern matching and refinements

The table below gives lattice parameters, volume, and Bragg R factor for the major perovskite phase. Rietveld refinements have been further performed for the systems highlighted in red.

System	a(Å)	b(Å)	c(Å)	Volume (Å^3)	Bragg R factor
BFO	5.58123(2)	5.58123(2)	13.87698(1)	374.356(4)	5.83
0.125 at% Co	5.57531(24)	5.57531(24)	13.87268(72)	373.447(30)	2.29
0.25 at% Co	5.58169(13)	5.58169(13)	13.88015(64)	374.504(21)	2.68
0. 5 at% Co	5.57957(8)	5.57957(8)	13.86793(36)	373.891(12)	1.06
1 at% Co	5.58578(8)	5.58578(8)	13.88686(36)	375.234(12)	8.69
1.5 at% Co	5.58123(7)	5.58123(7)	13.87851(27)	374.398(10)	6.98
3 at% Co	5.57419(4)	5.57419(4)	13.85378(18)	372.789(6)	0.65
1 at% Ti	5.58883(4)	5.58883(4)	13.88907(16)	375.704(6)	2.18
2 at% Ti	5.59455(7)	5.59455(7)	13.89853(30)	376.730(11)	0.62
3 at% Ti	5.59217(10)	5.59217(10)	13.89302(45)	376.260(16)	9.62
5 at% Ti	5.58452(15)	5.58452(15)	13.84841(66)	374.026(23)	1.28
0.25-0.25 at% Co-Ti	5.58389(10)	5.58389(10)	13.88652(39)	374.972(14)	2.61
0.25-1 at% Co-Ti	5.58244(18)	5.58244(18)	13.86805(57)	374.278(23)	0.84

Full pattern matching data for different systems obtained from FullProf software:

Calcined BFO

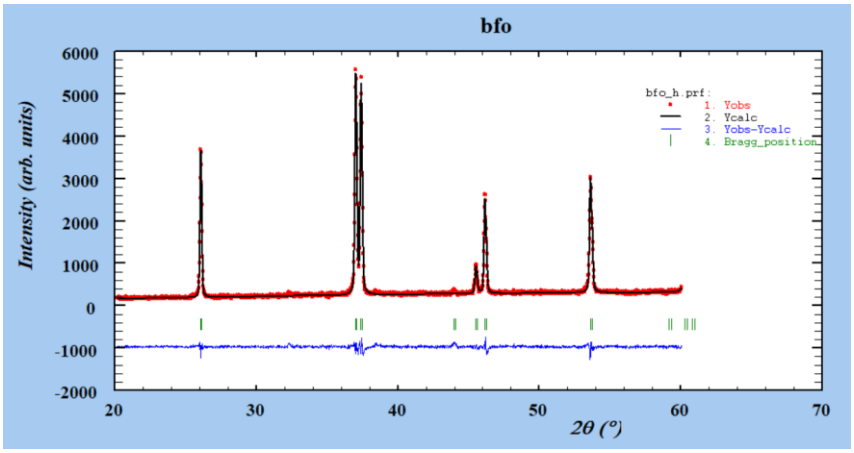

0.125 at% Co

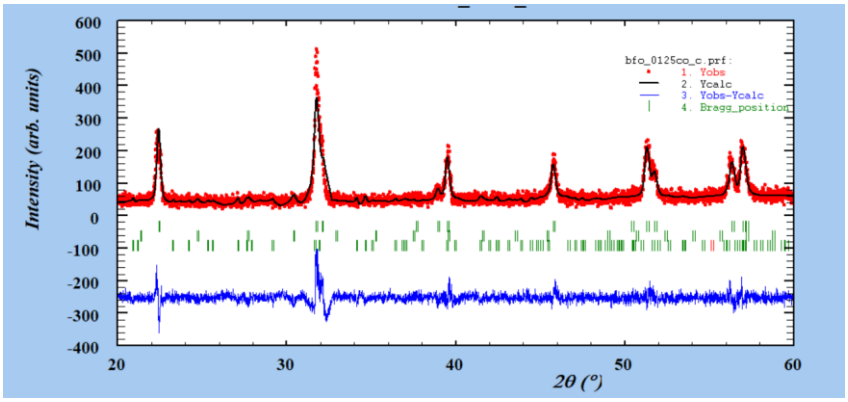

0.25 at% Co

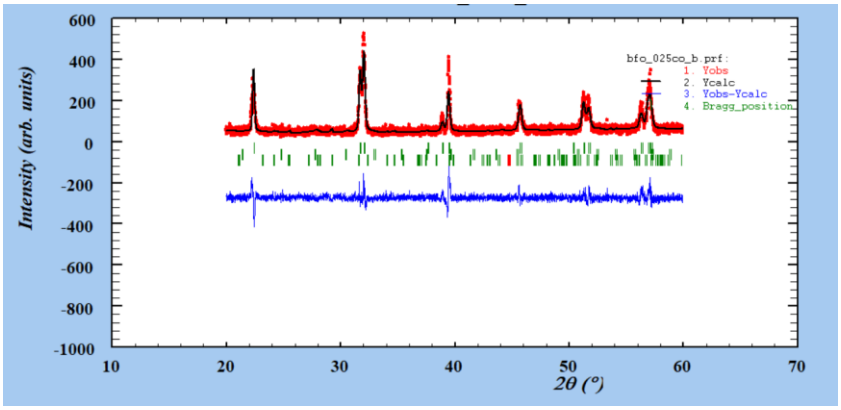

0.5 at% Co

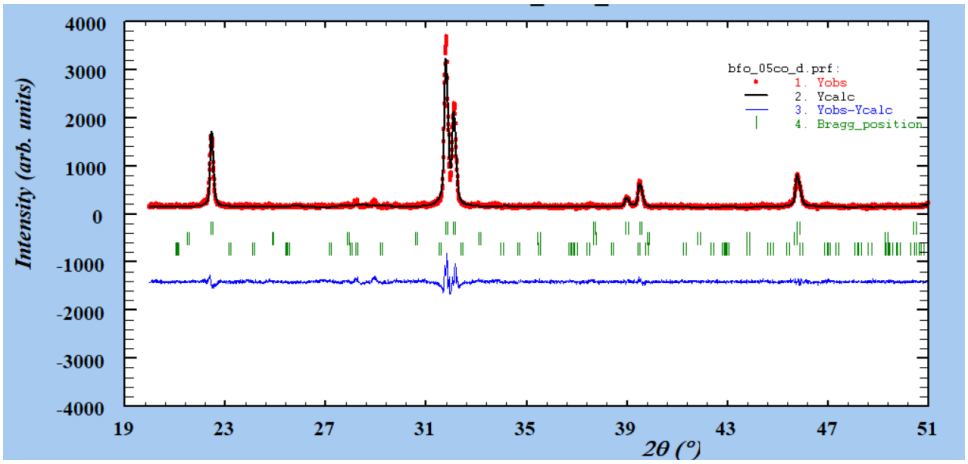

3 at% Co

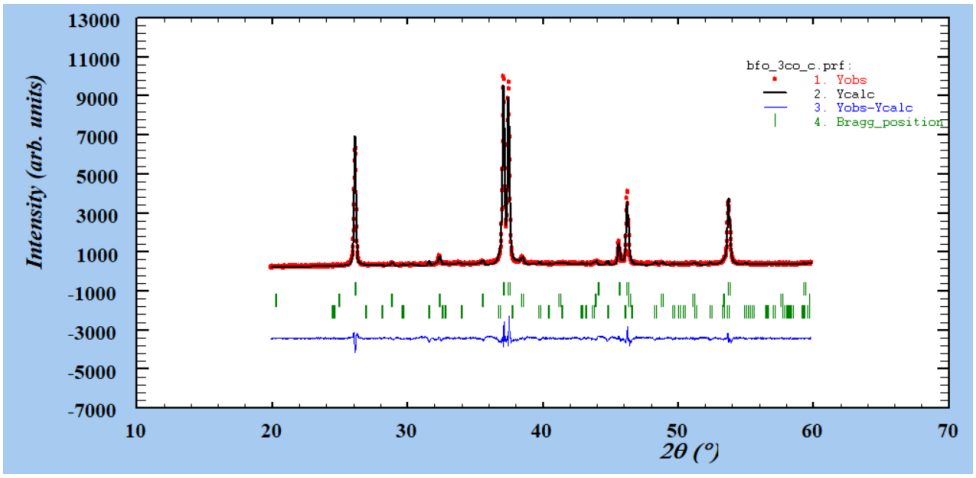

1 at% Ti

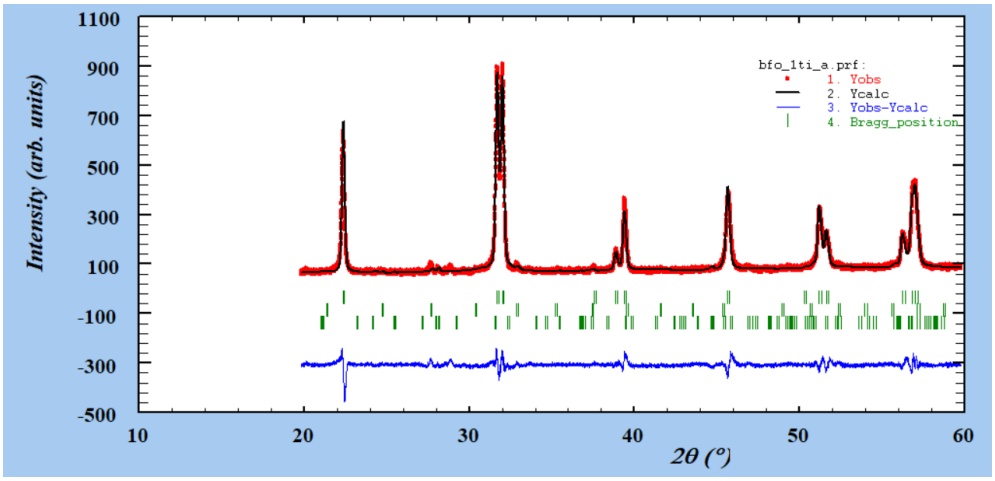

2 at% Ti

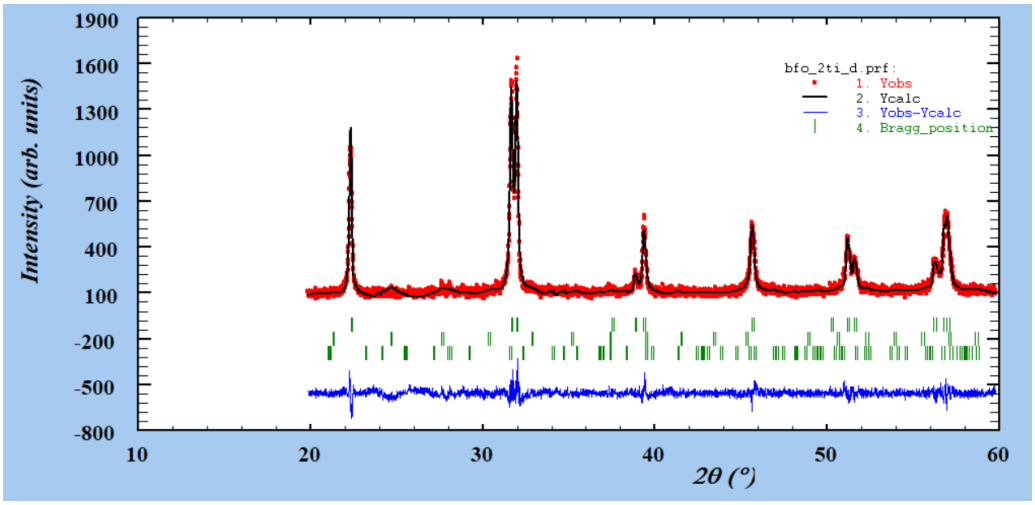

5 at% Ti

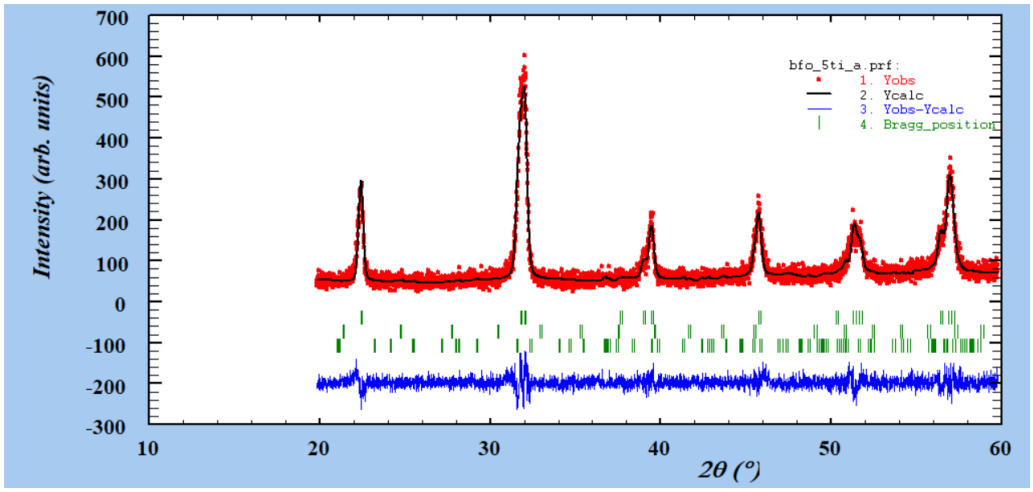

0.25-0.25 at% Co-Ti

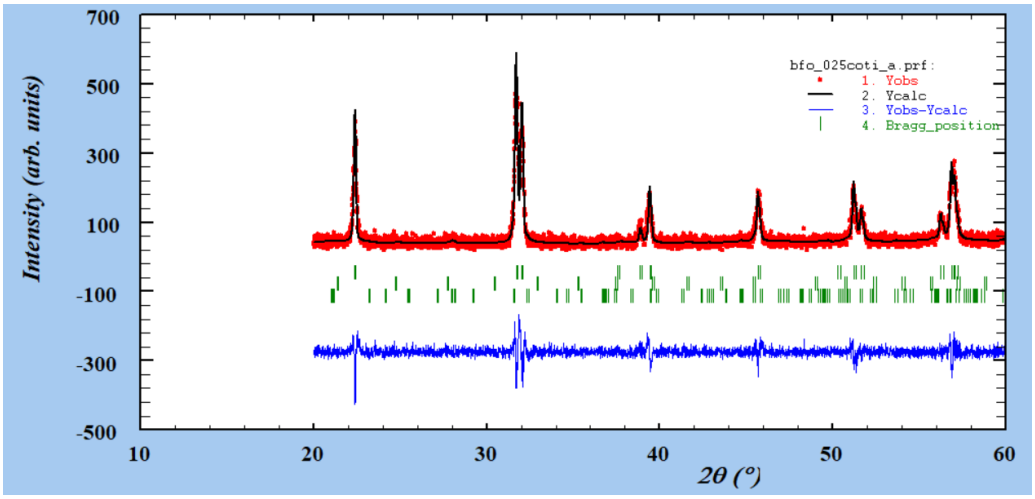

0.25-1 at% Co-Ti

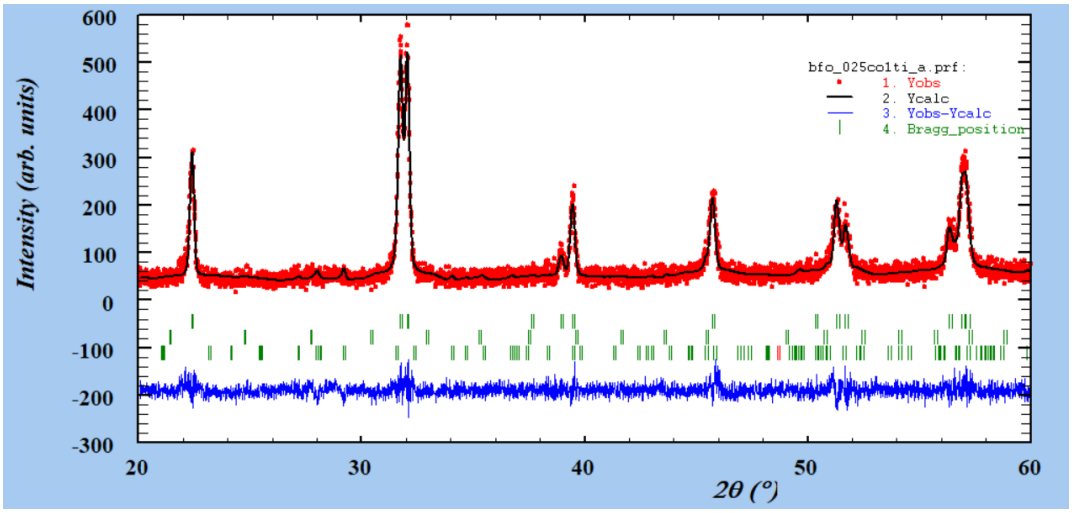

10.2 Analysis of data from BDS

10.2.1 Jonscher fitting (AC conductivity vs frequency)

BFO

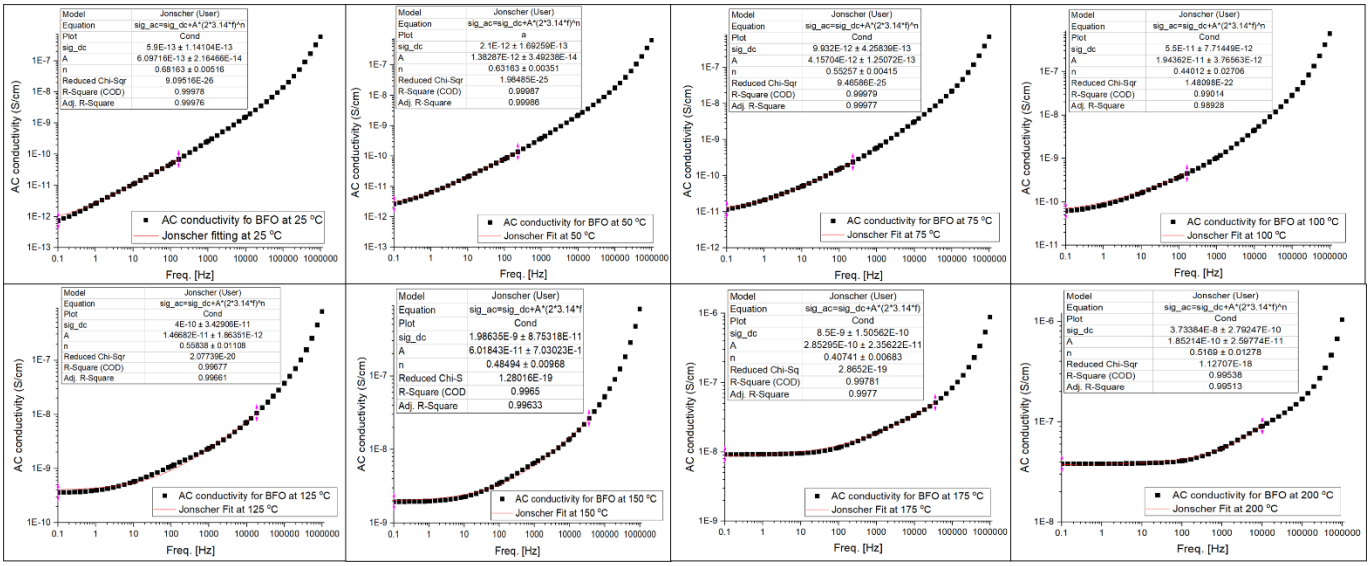

Cobalt

0.125 at% Co

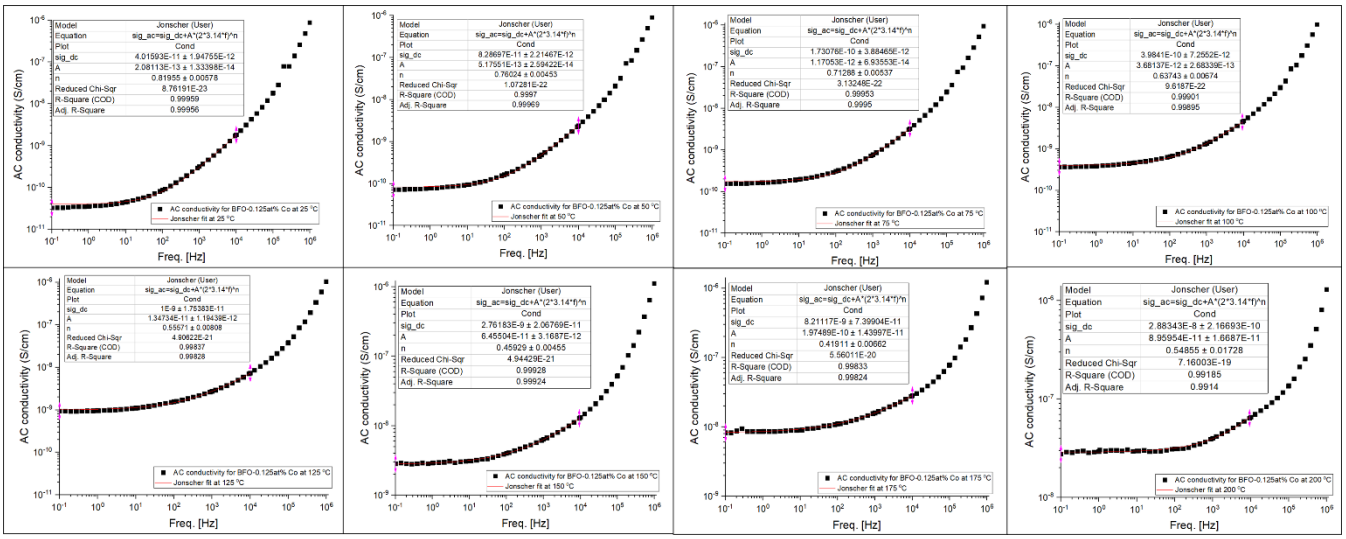

0.25 at% Co

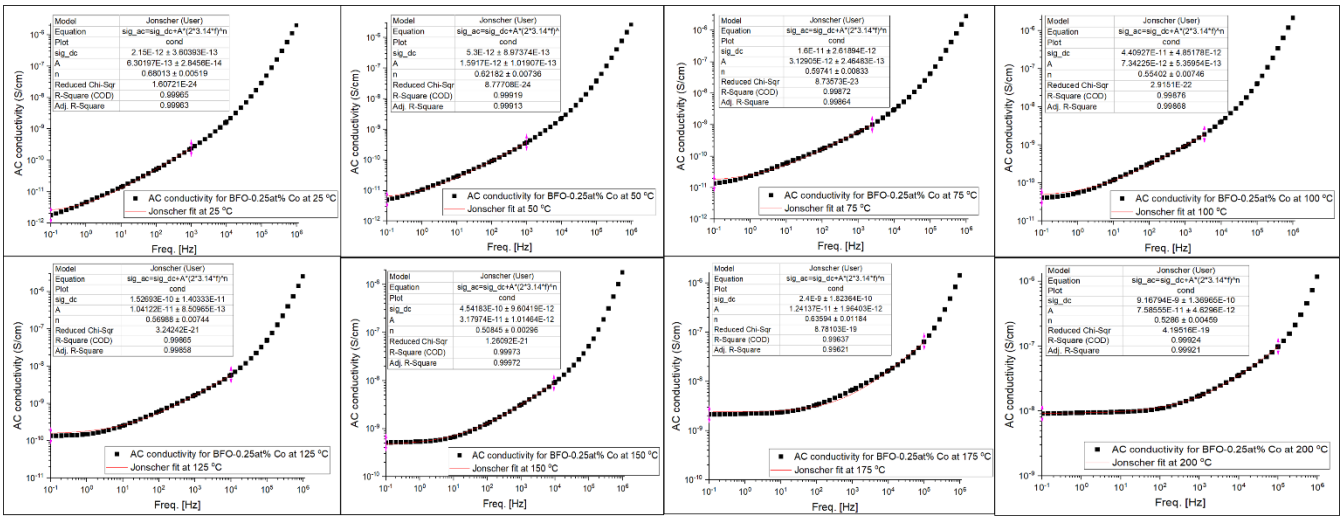

0.5 at% Co

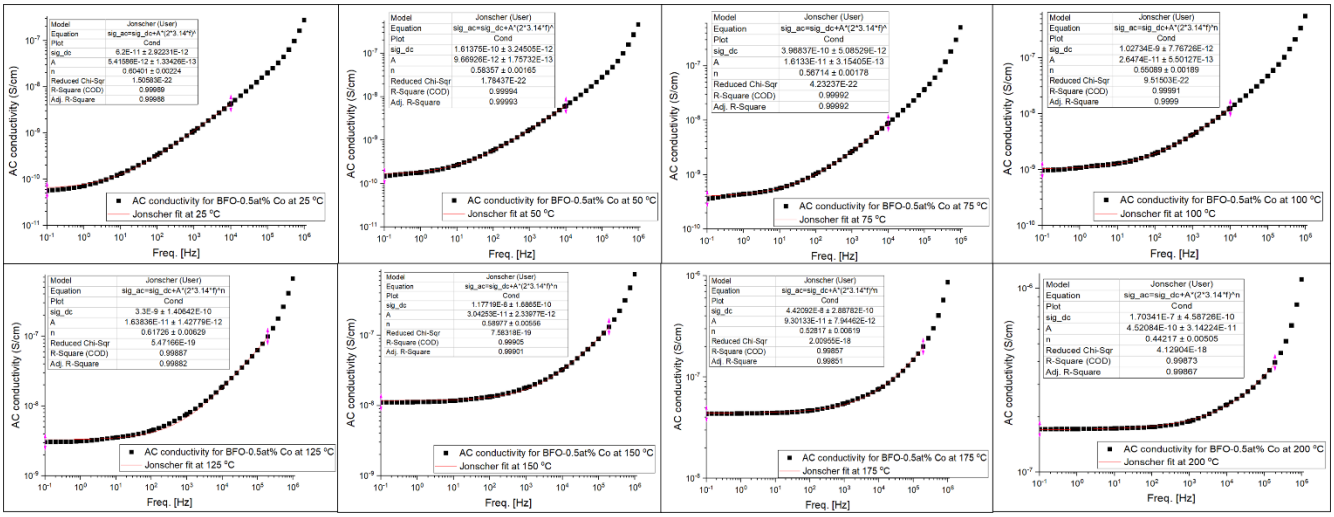

1 at% Co

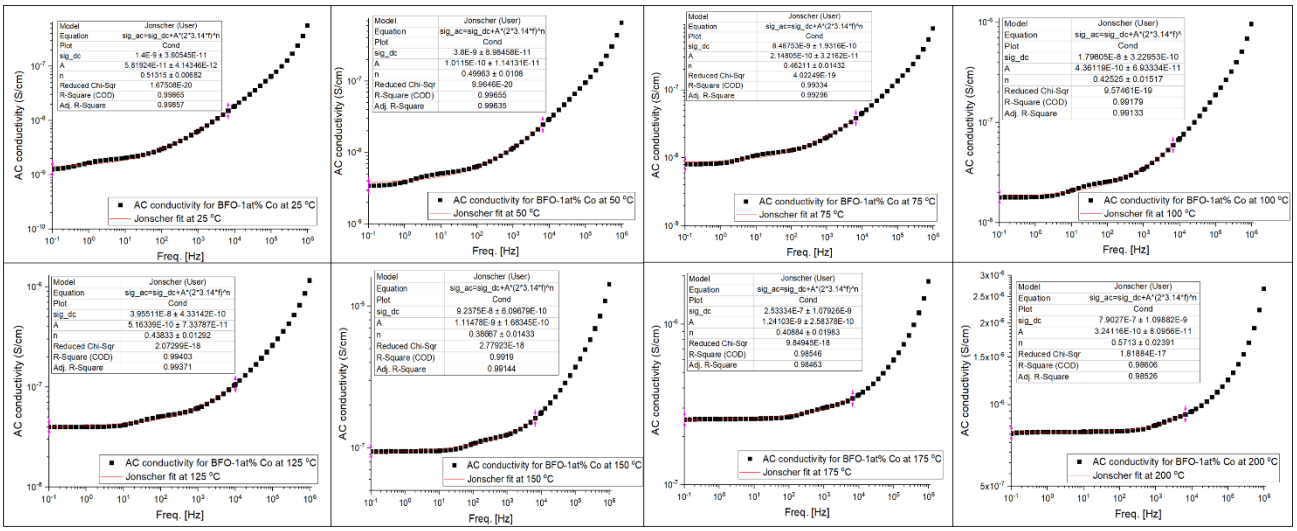

1.5 at% Co

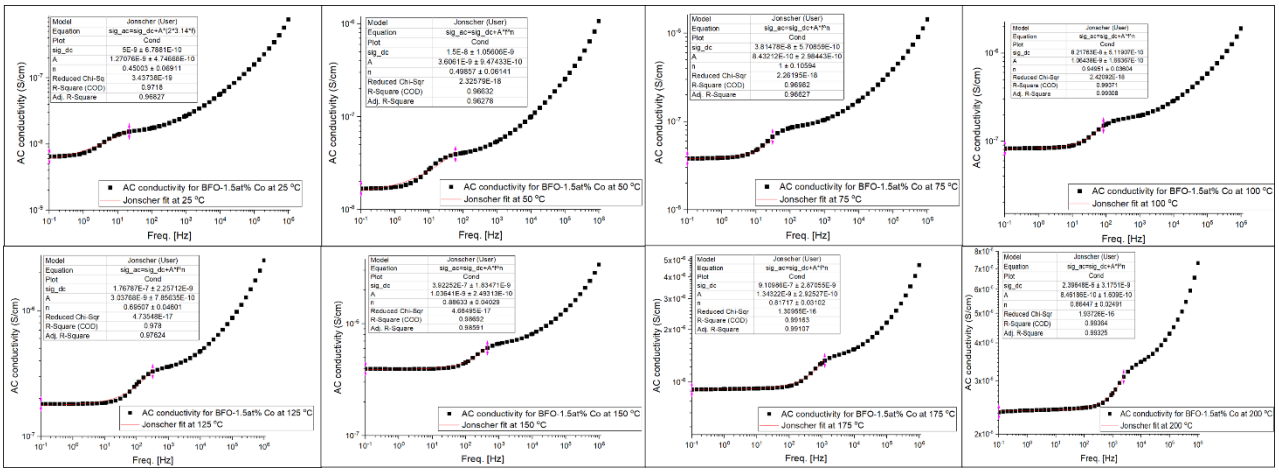

3 at% Co

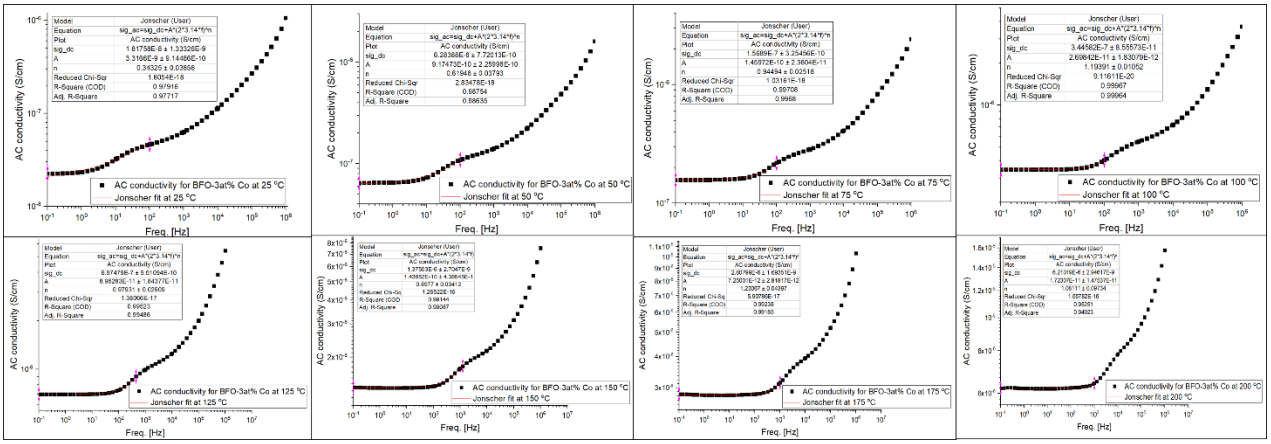

Titanium

1 at% Ti

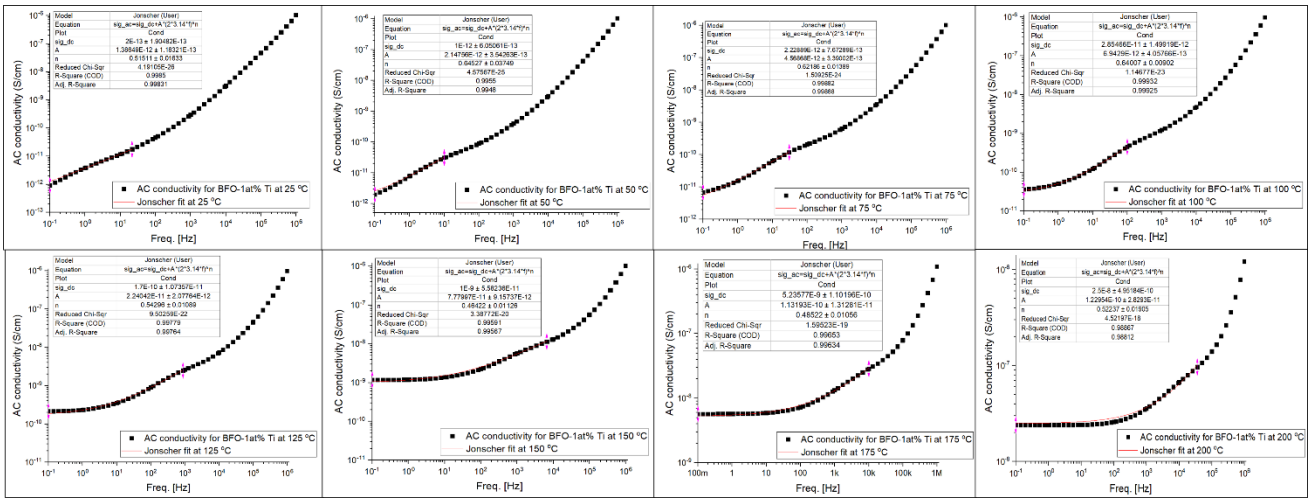

2 at% Ti

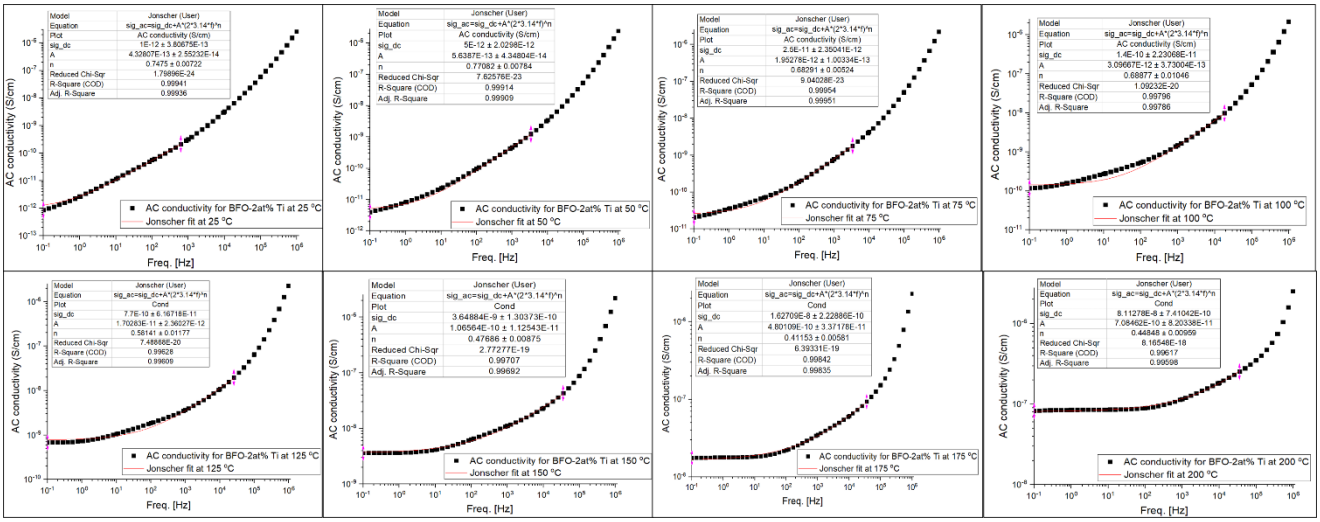

3 at% Ti

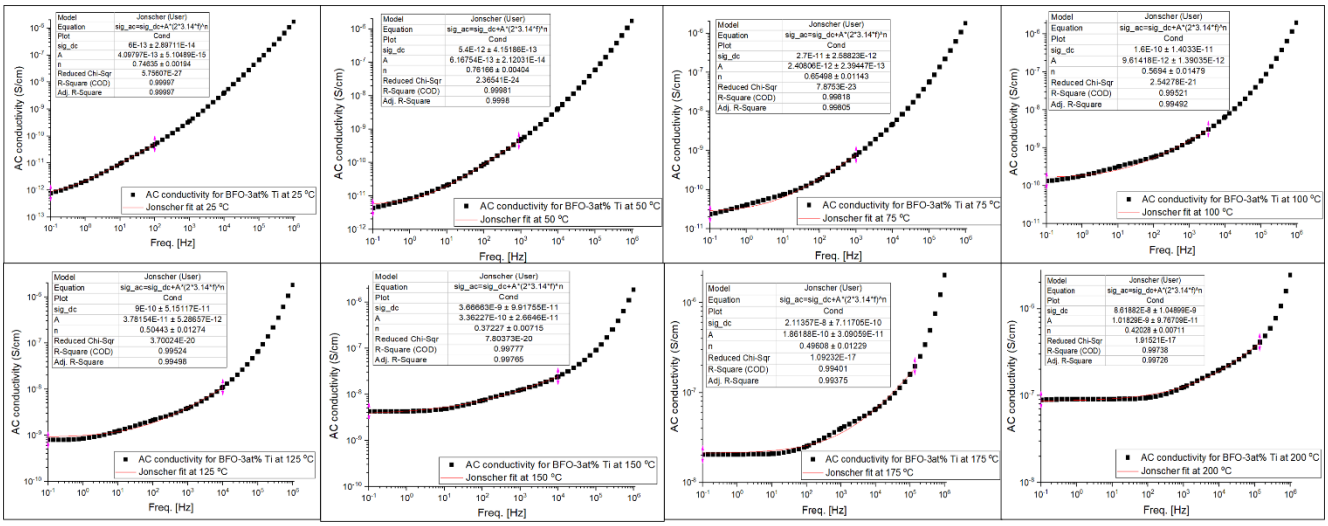

5 at% Ti

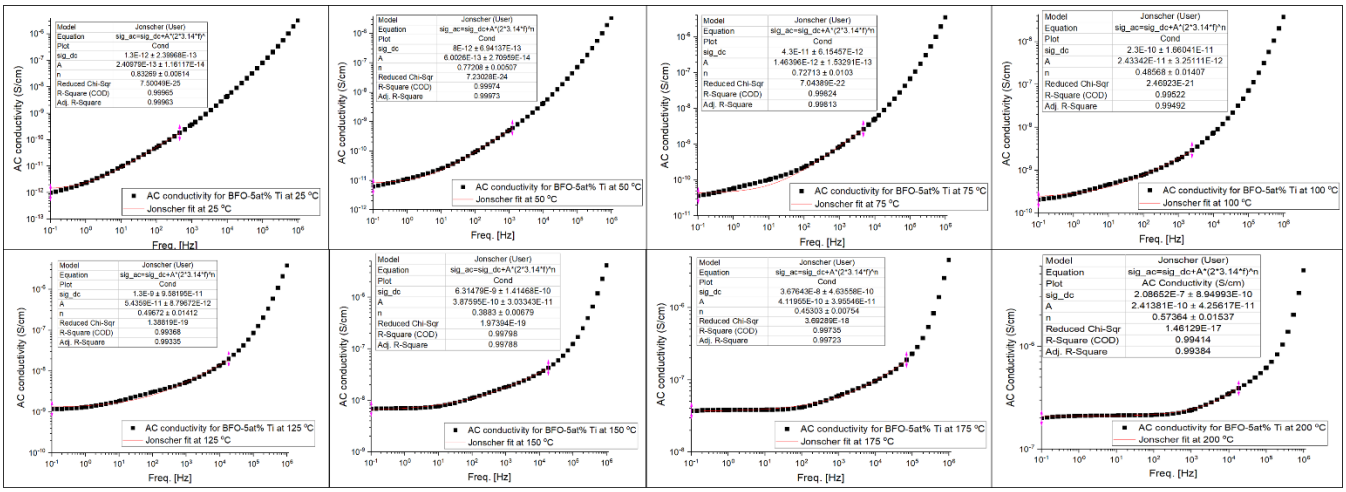

Cobalt-titanium

0.25-0.25 at% Co-Ti

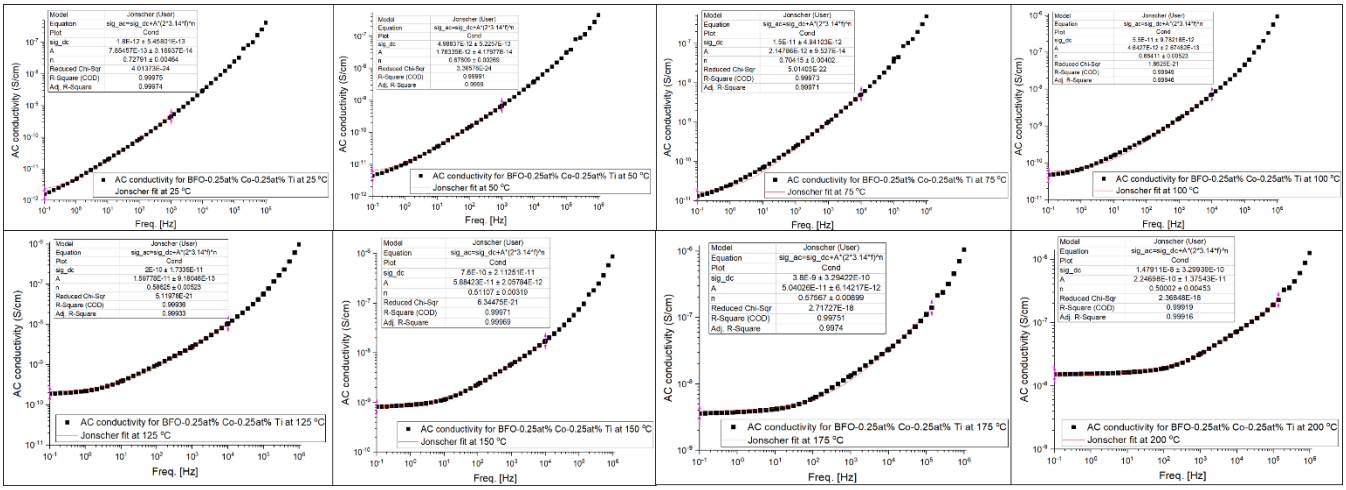

0.25-1 at% Co-Ti

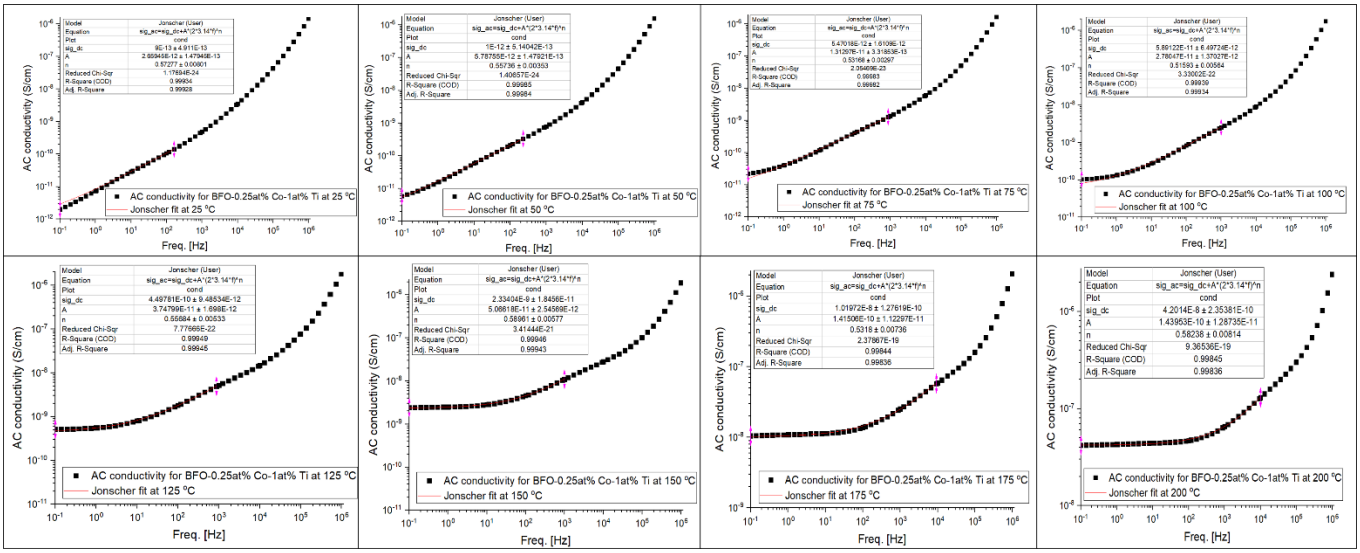

BFO-STO

30 at% STO

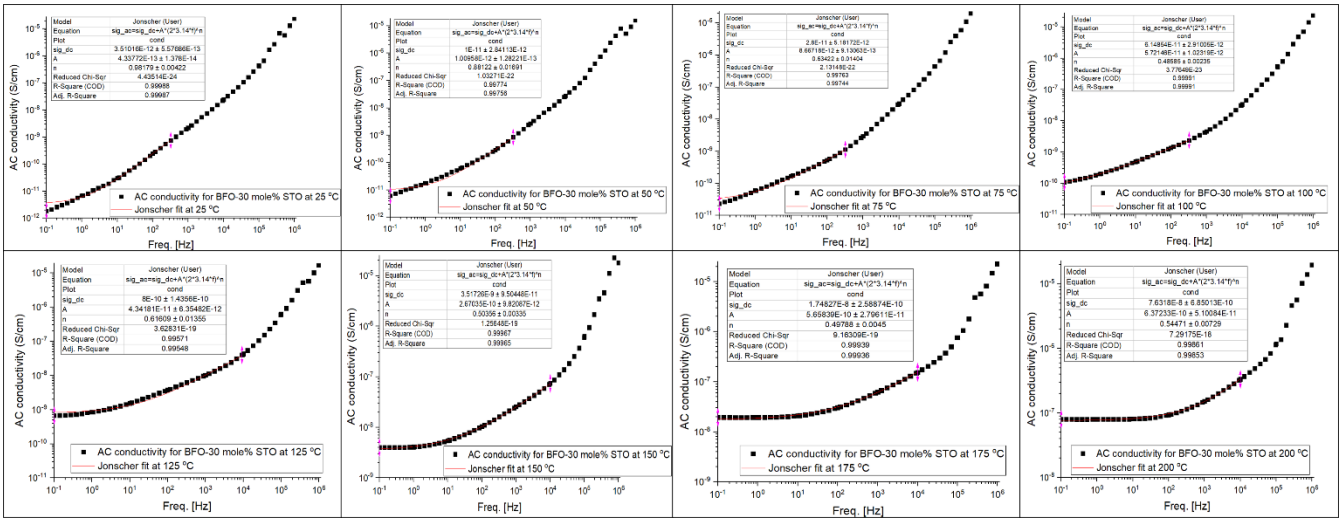

10.2.2 Nyquist plots (from 75 to 200 ºC)

BFO

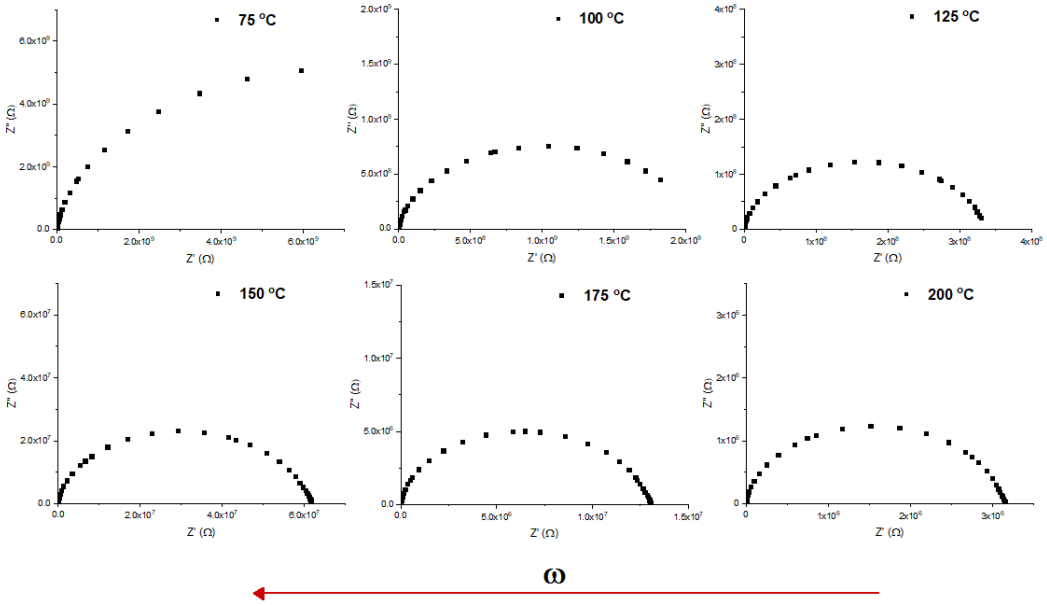

Cobalt

0.125 at% Co

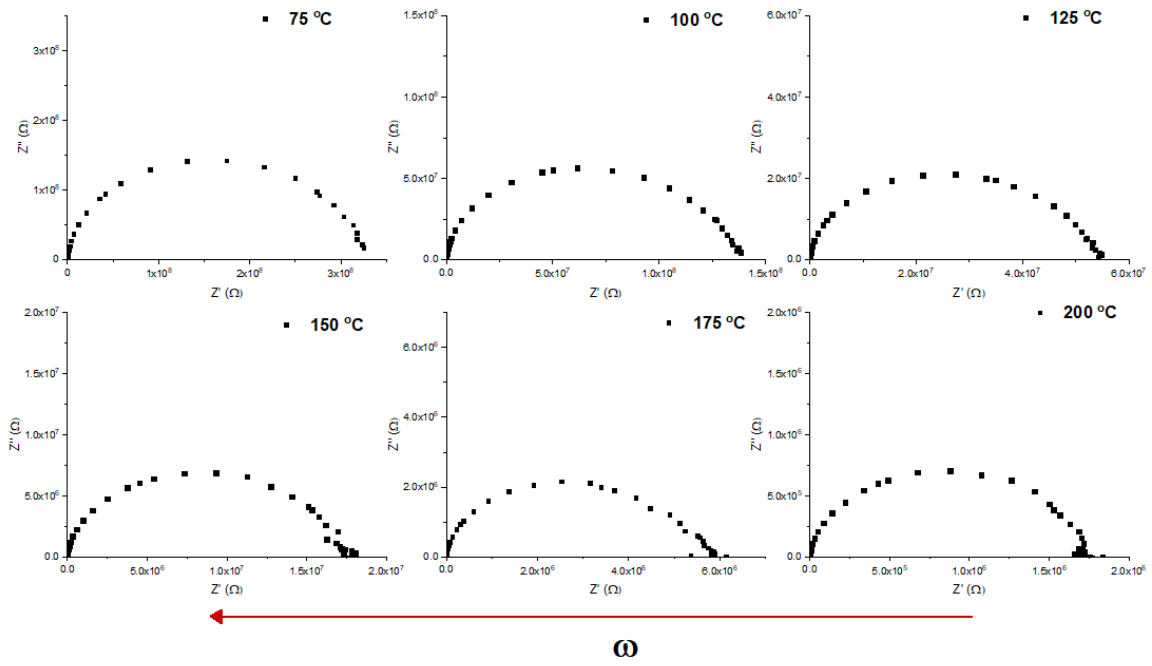

0.25 at% Co

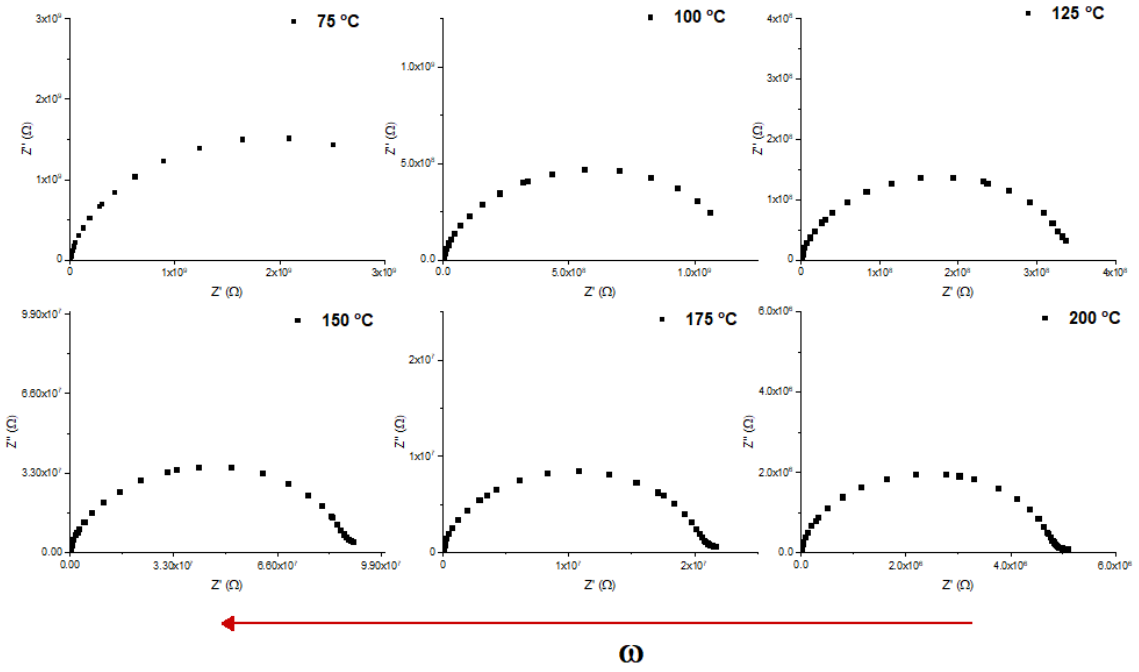

0.5 at% Co

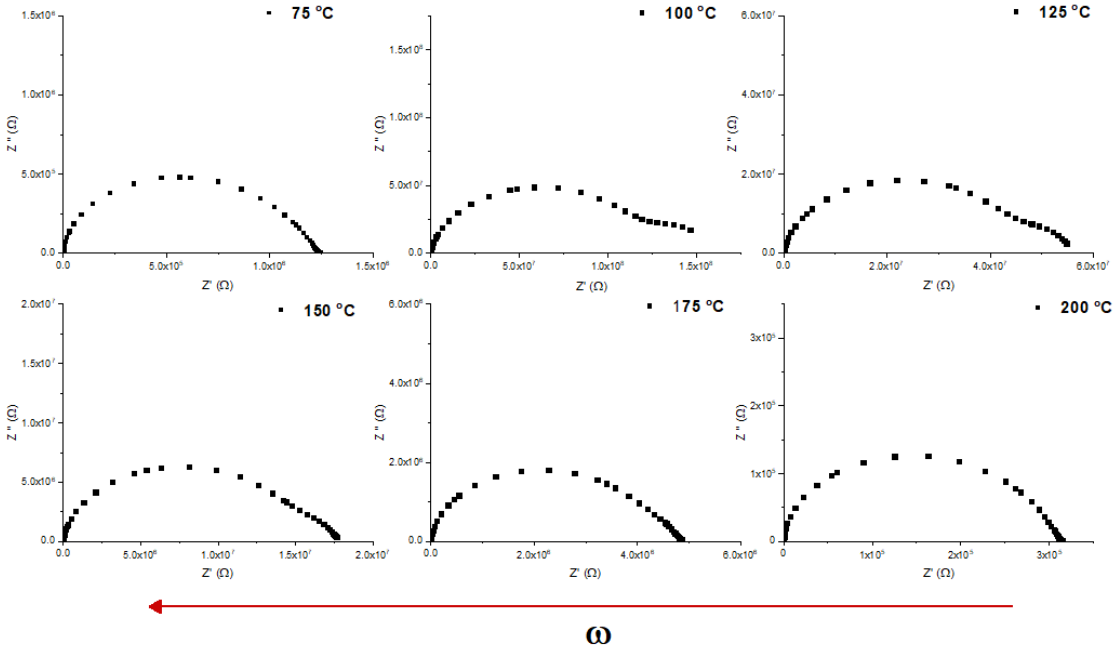

1 at% Co

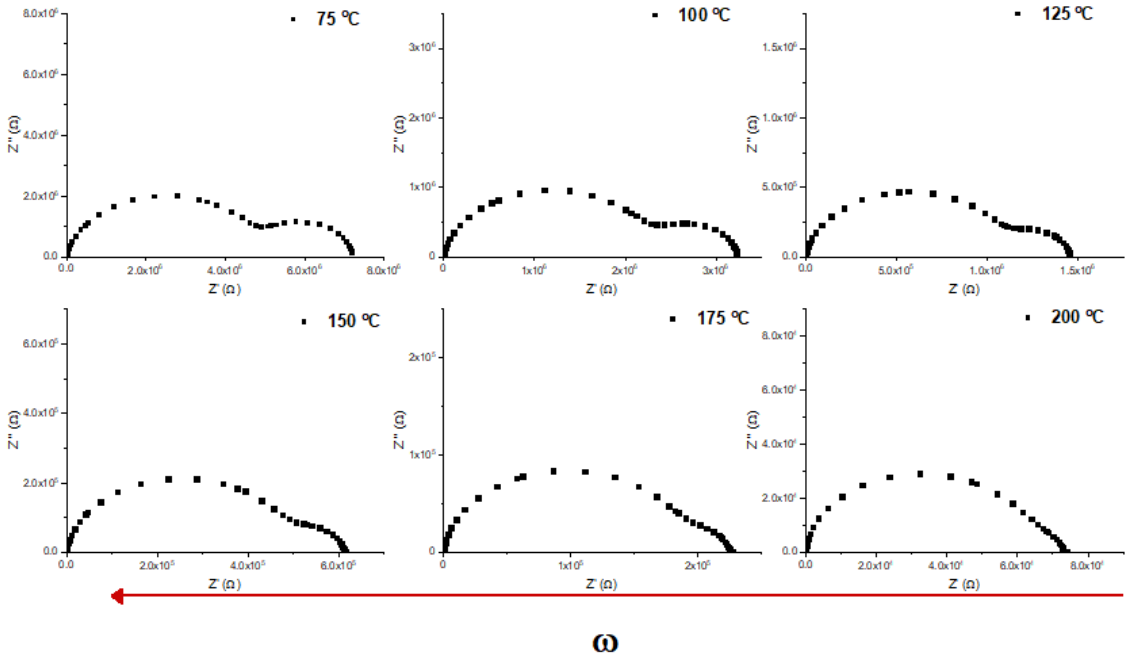

1.5 at% Co

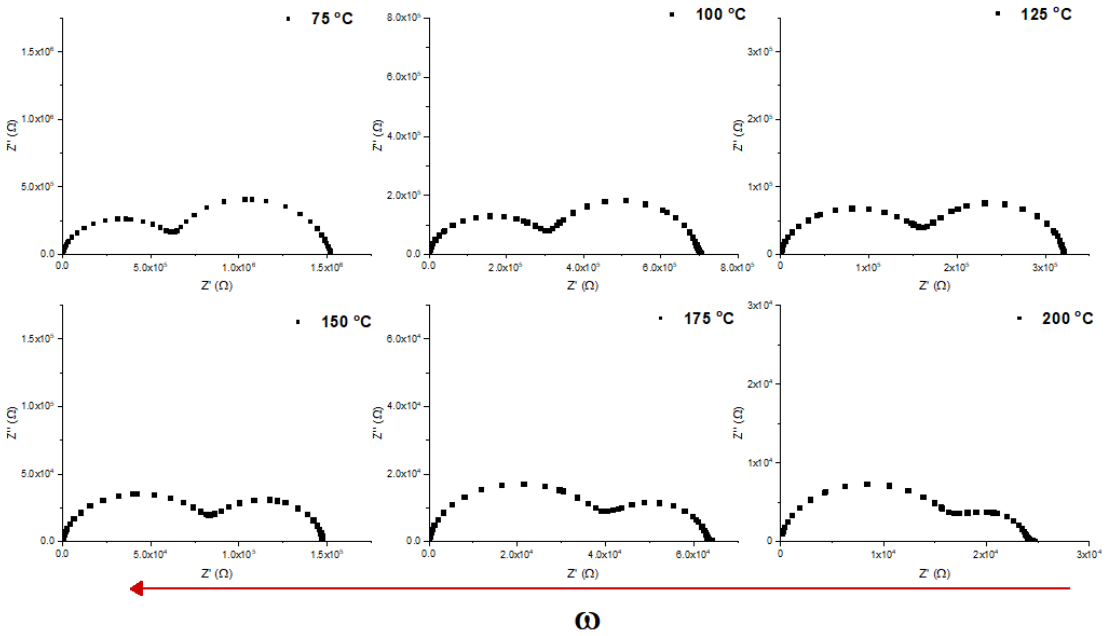

3 at% Co

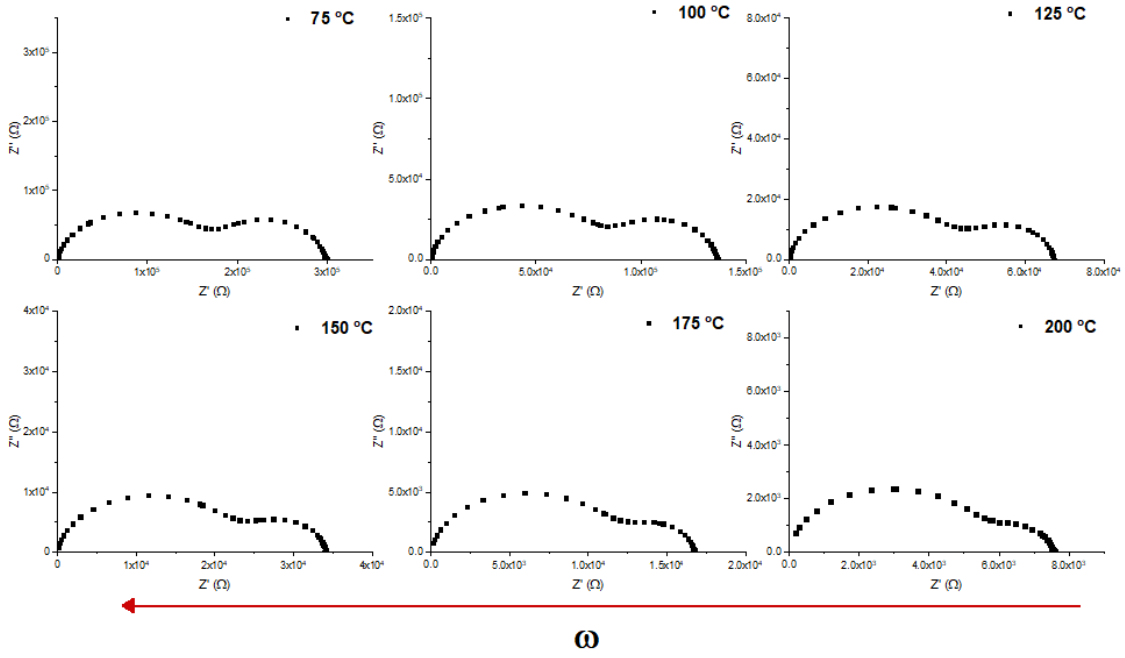

Titanium

1 at% Ti

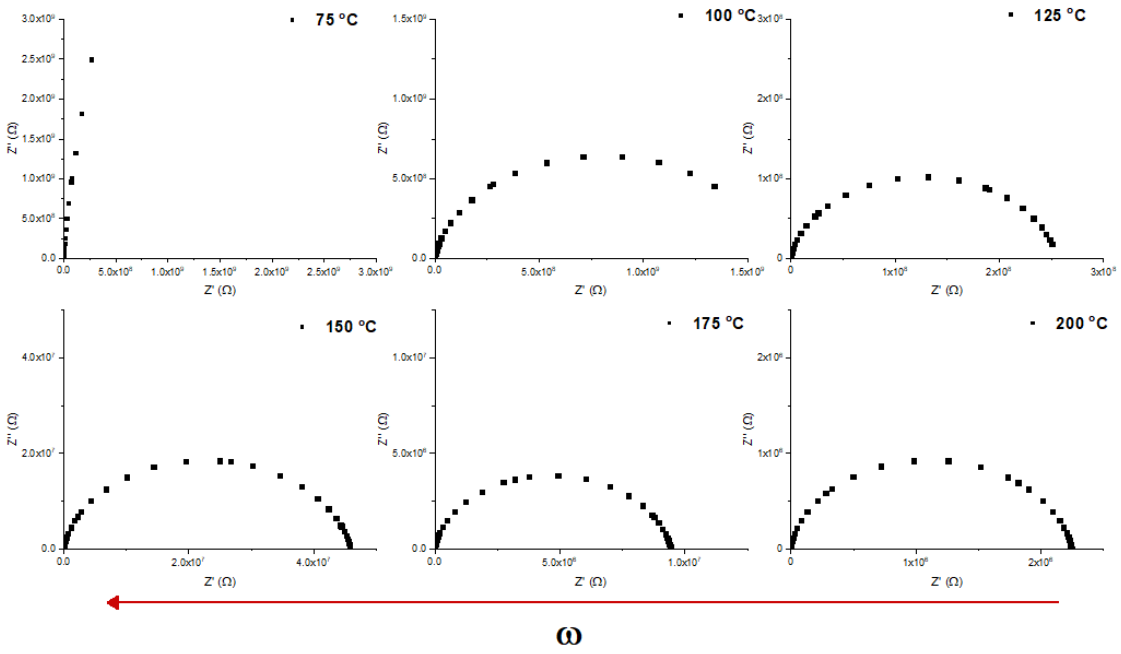
75 °C
100 °C
125 °C
150 °C
175 °C
200 °C
Z'' (Ω)
Z' (Ω)
ω

2 at% Ti

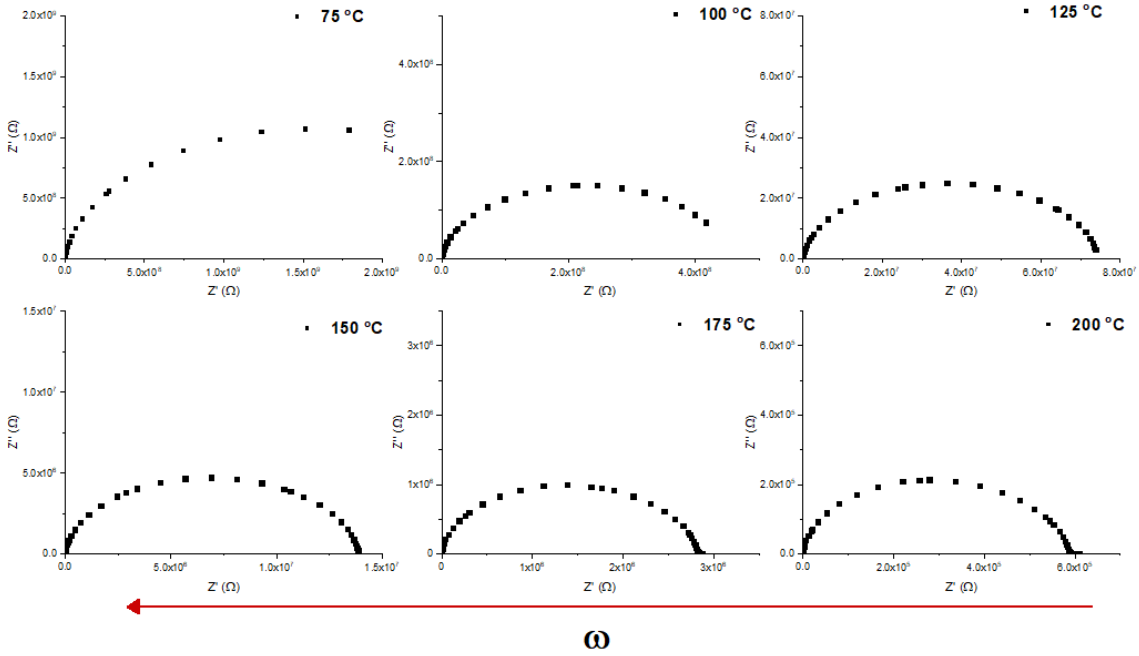
75 °C
100 °C
125 °C
150 °C
175 °C
200 °C
Z'' (Ω)
Z' (Ω)
ω

3 at% Ti

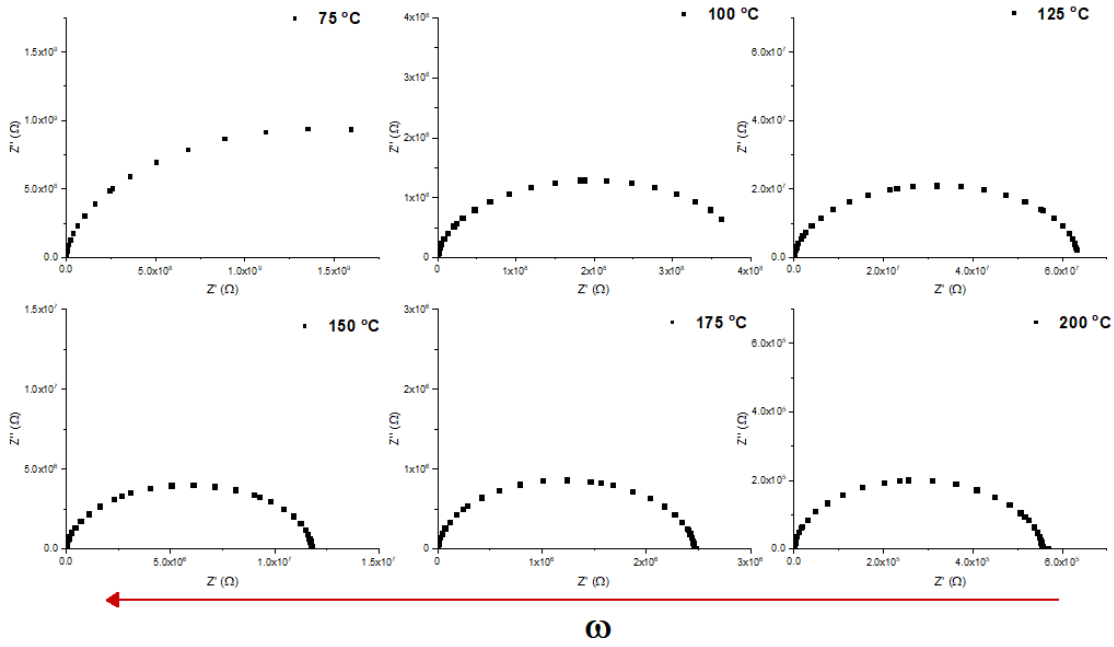

5 at% Ti

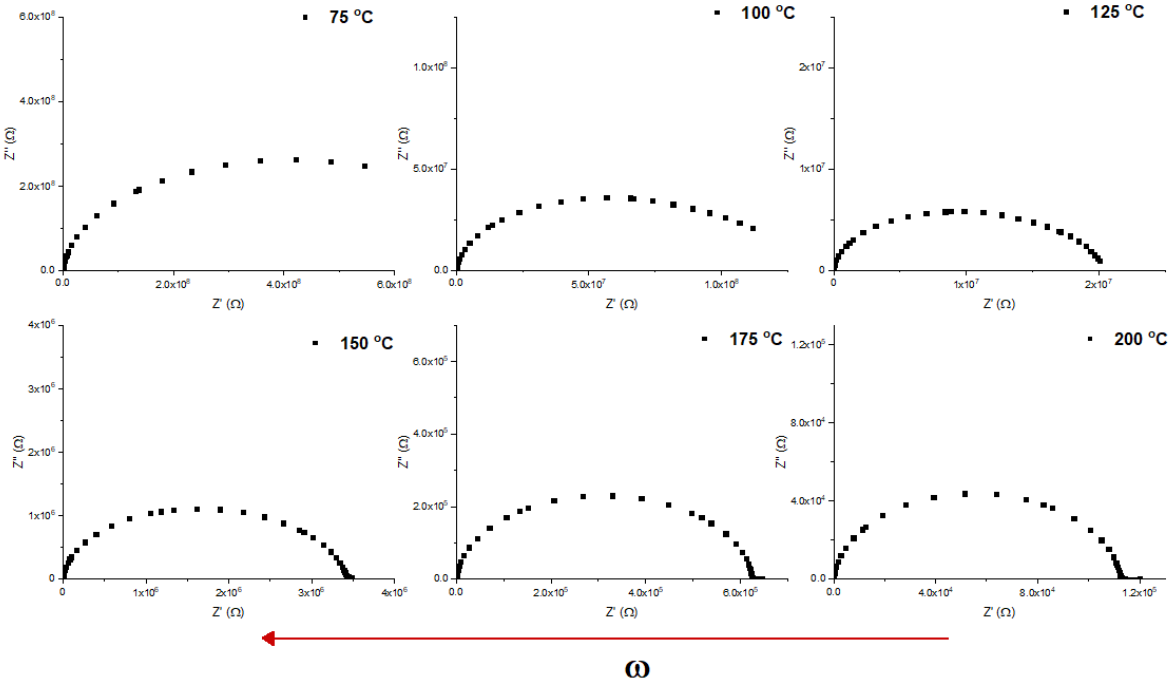

Cobalt-titanium

0.25-0.25 at% Co-Ti

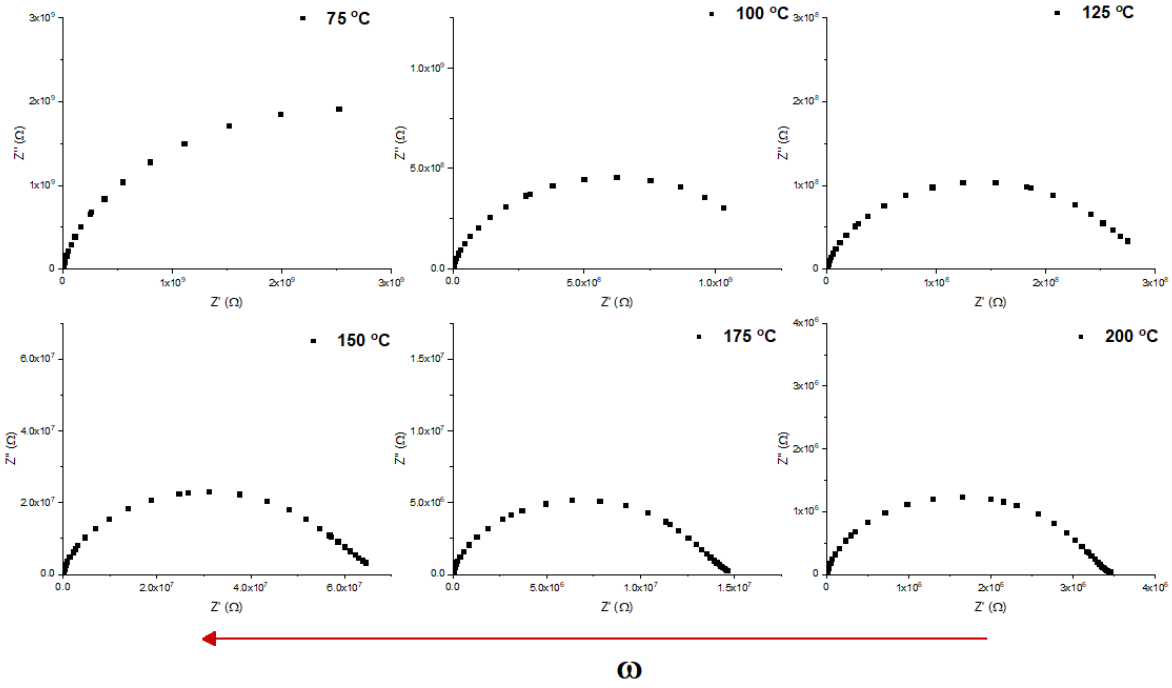

0.25-1 at% Co-Ti

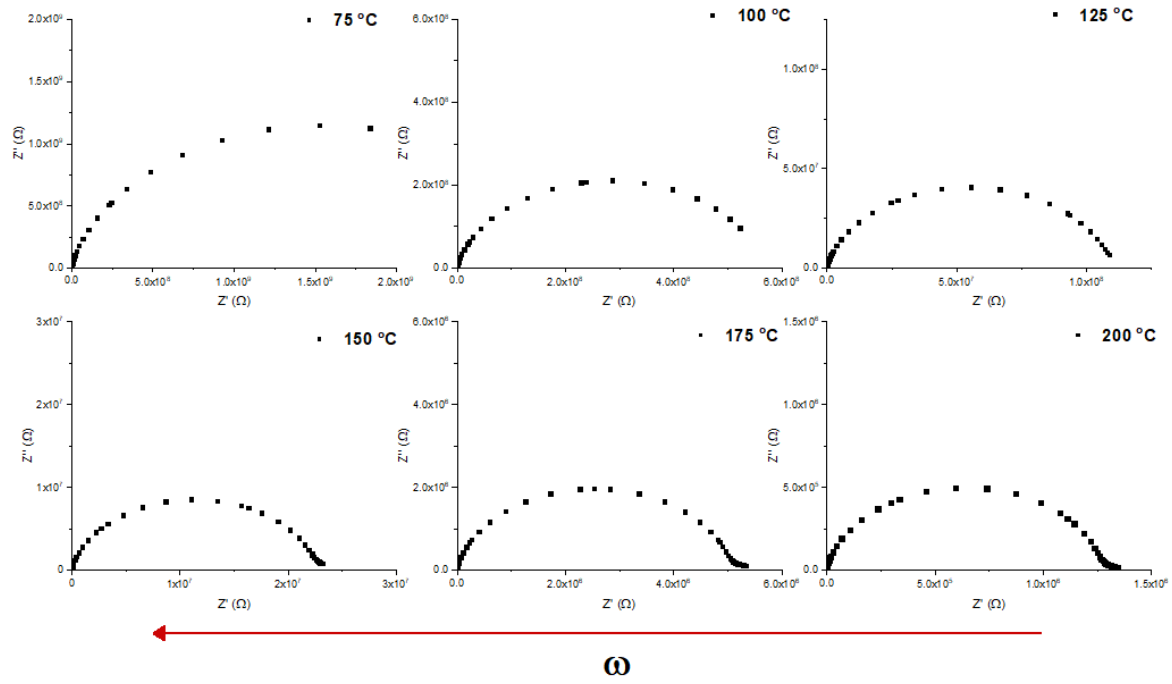

BFO-STO

30 at% STO

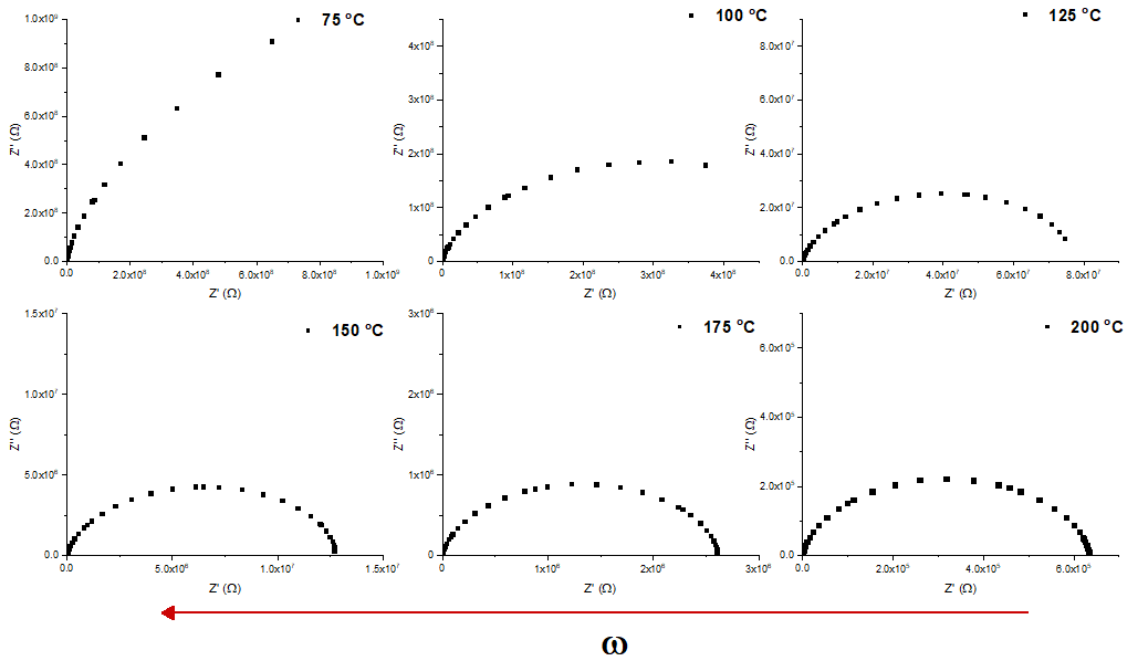

10.2.3 Complex Impedance fitting (complex impedance variation with frequency)

Function used for fitting,

complex cc = R1/(1+((1i*2*pi*f)^n1)*C1*R1)+ R2/(1+((1i*2*pi*f)^n2)*C2*R2);

Zim=cc.m_im

BFO

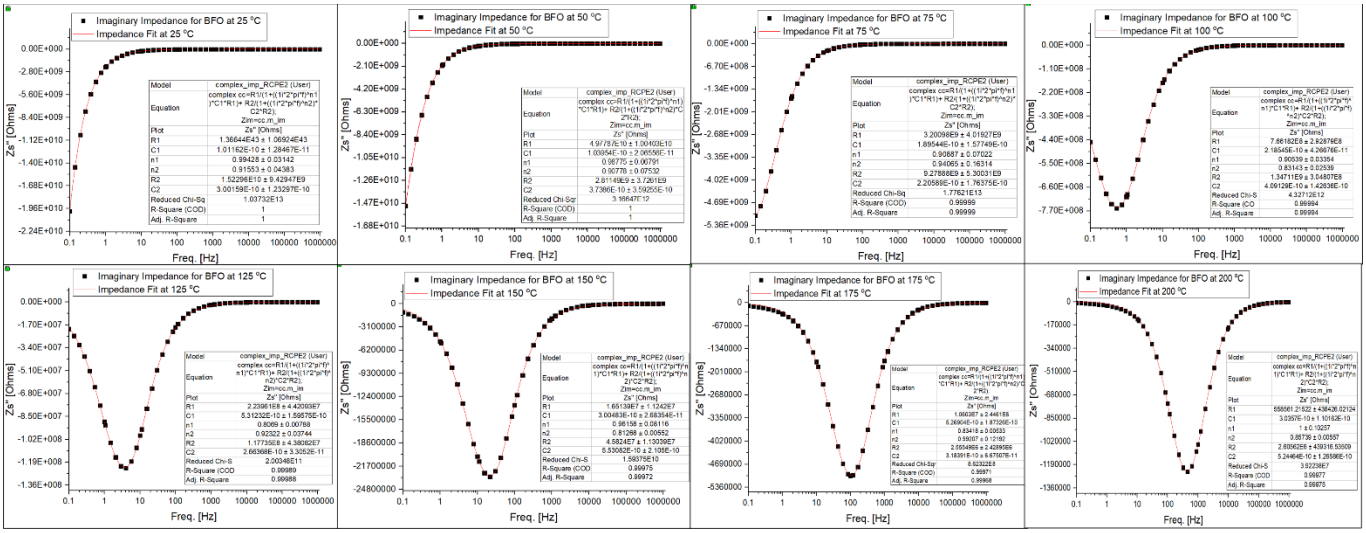

Cobalt

0.125 at% Co

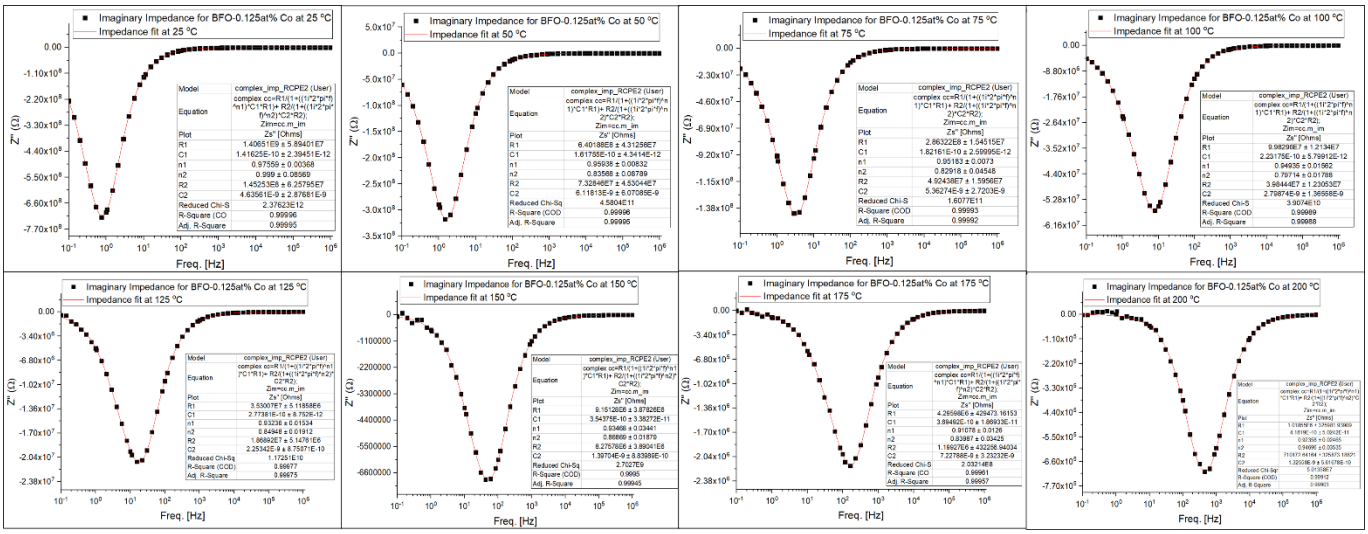

0.25 at% Co

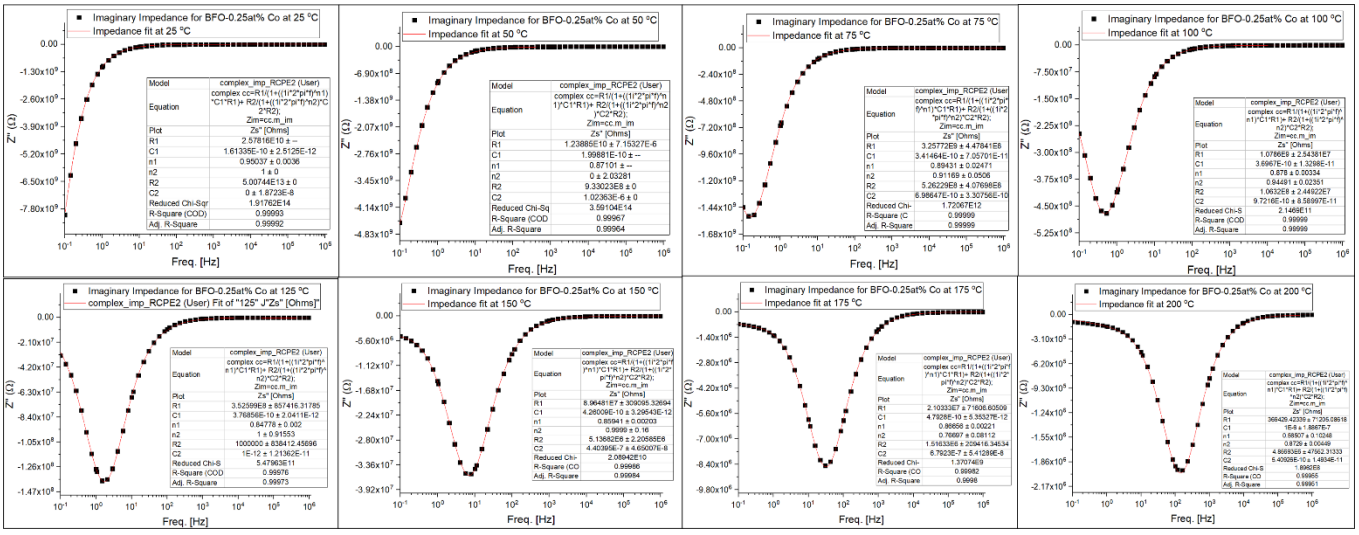

0.5 at% Co

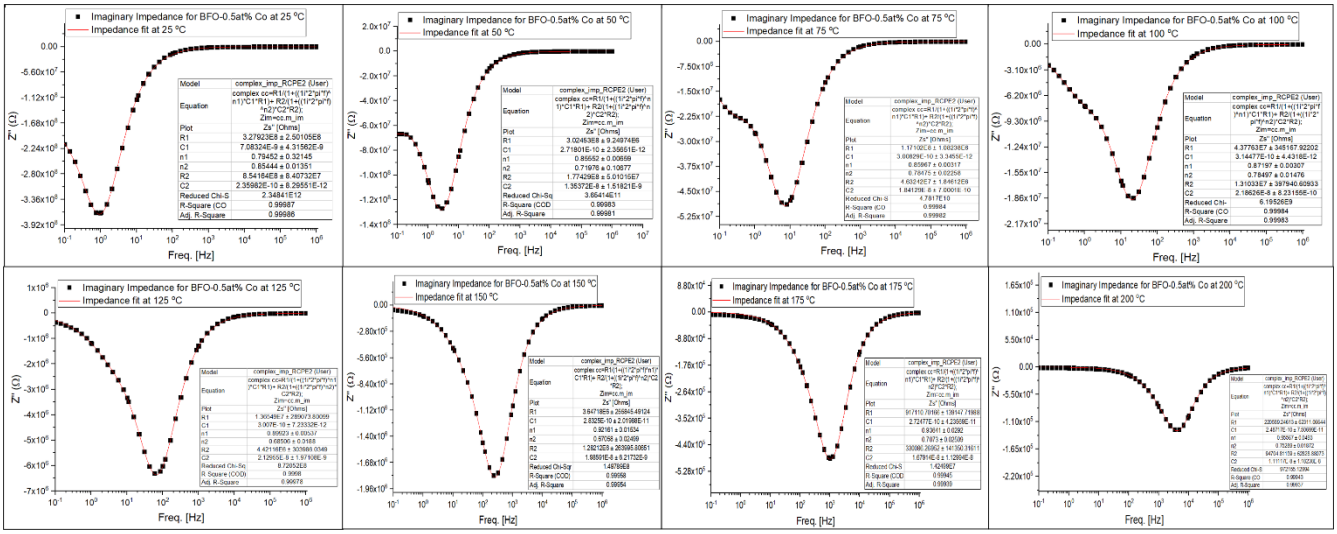

1 at% Co

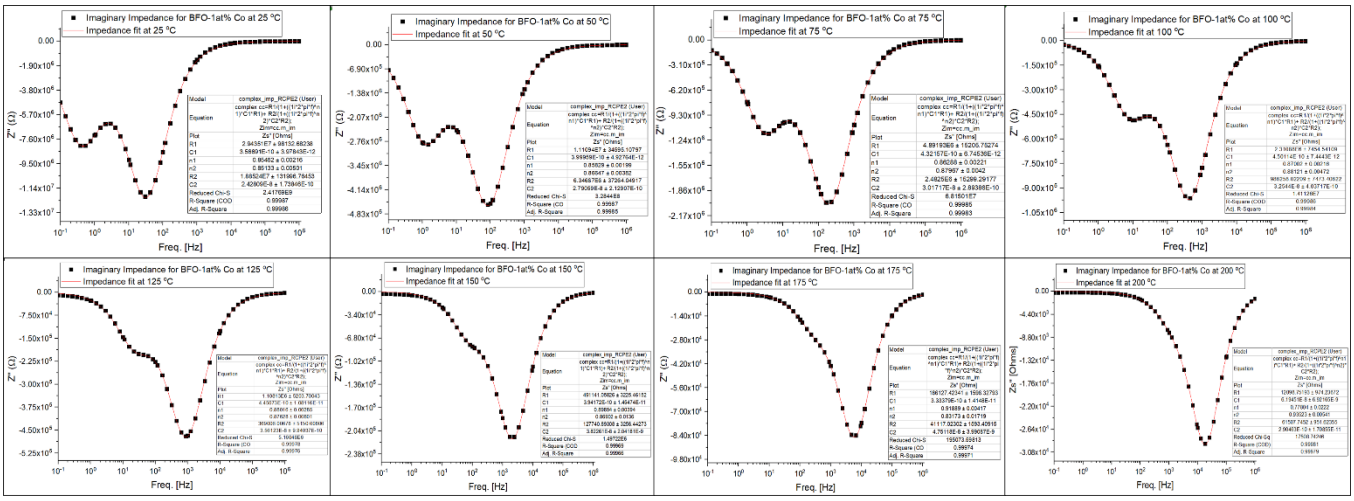

1.5 at% Co

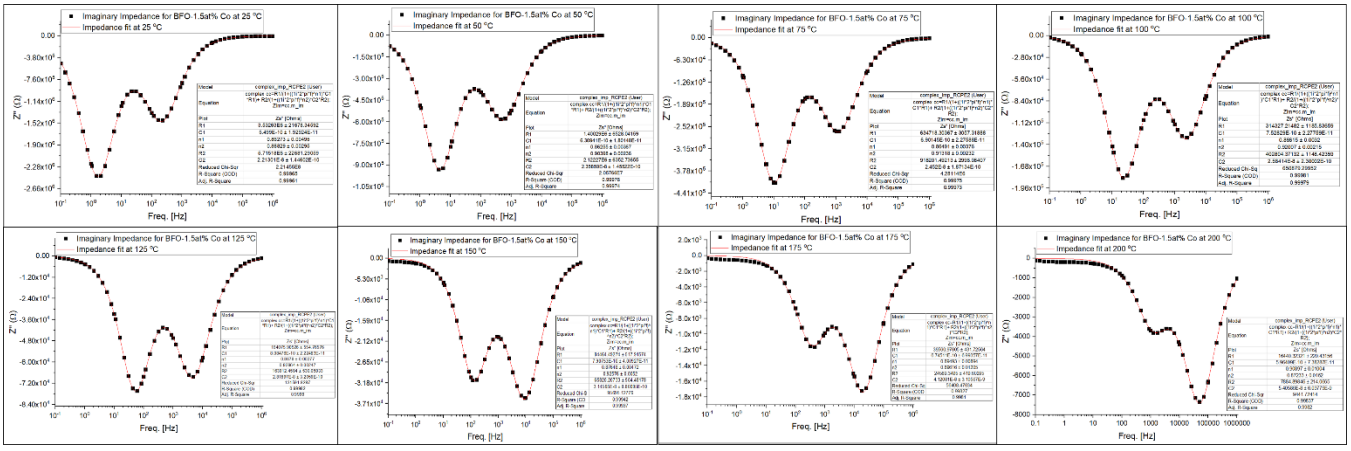

3 at% Co

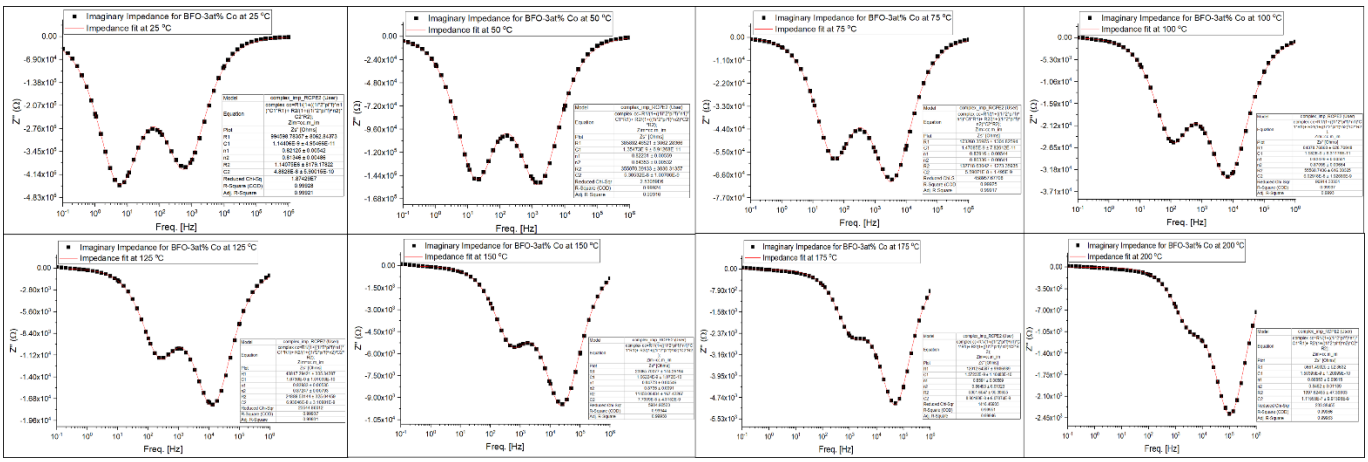

Titanium

1 at% Ti

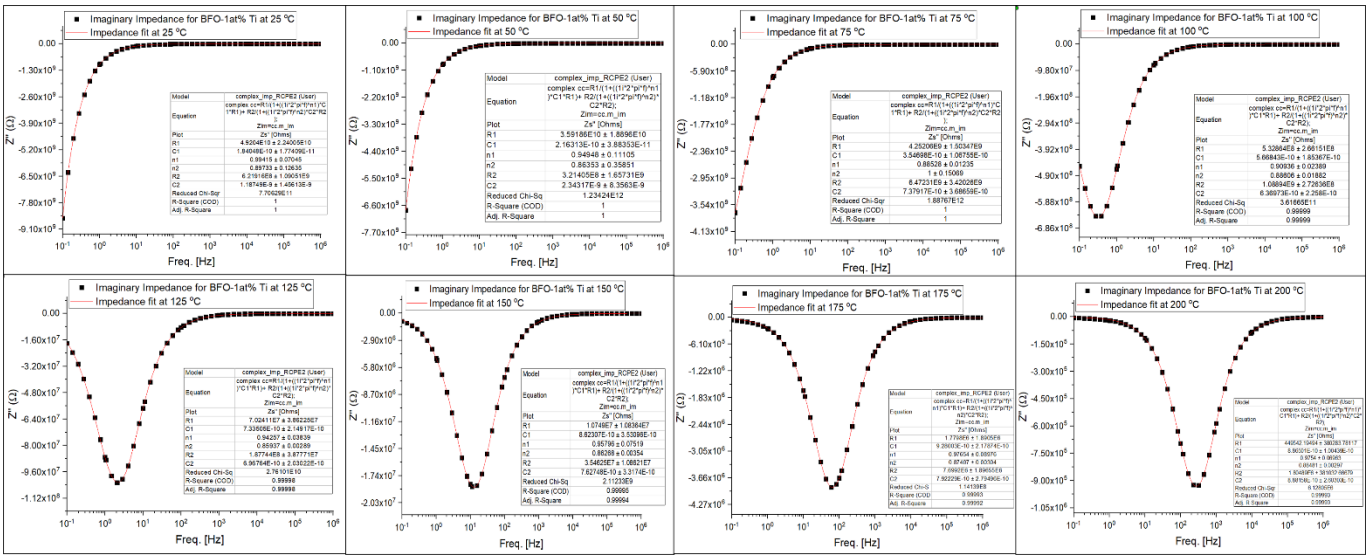

2 at% Ti

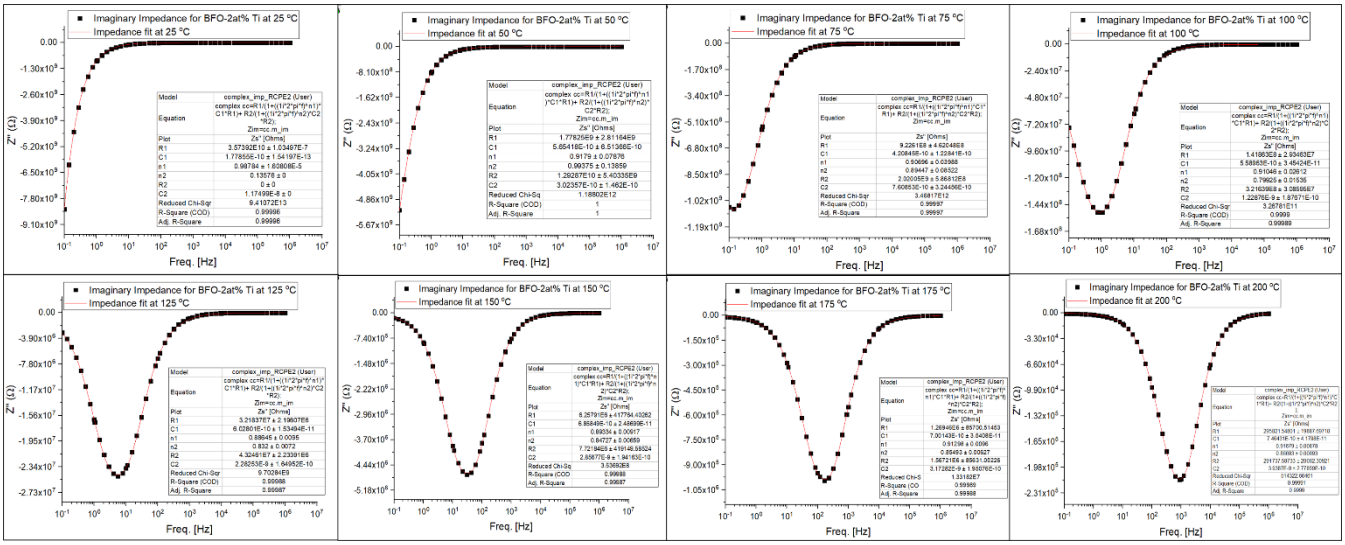

3 at% Ti

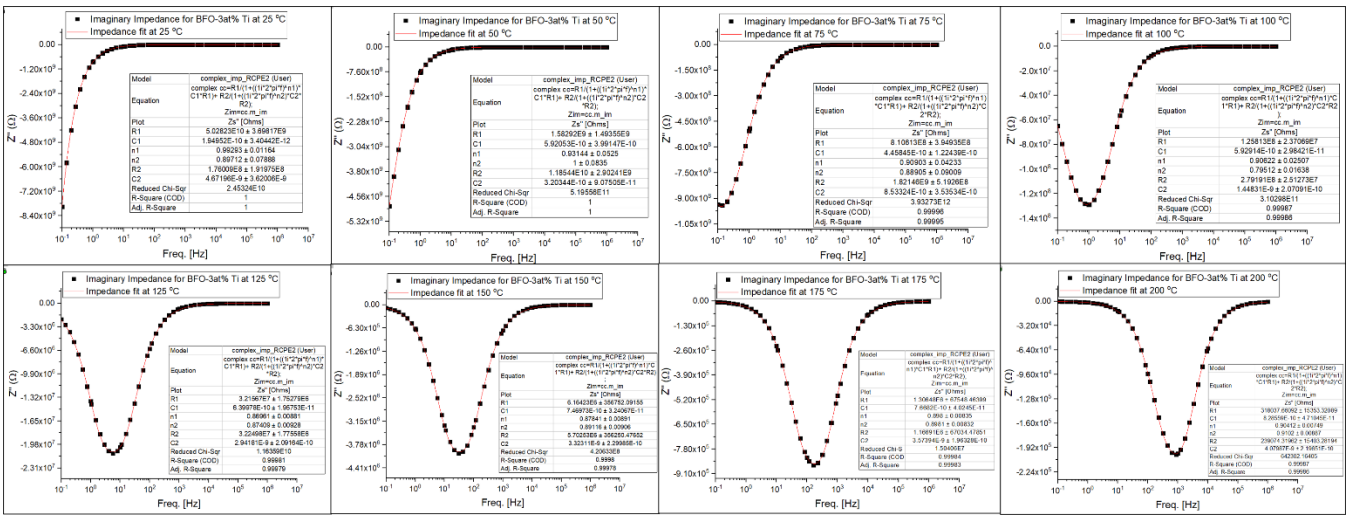

5 at% Ti

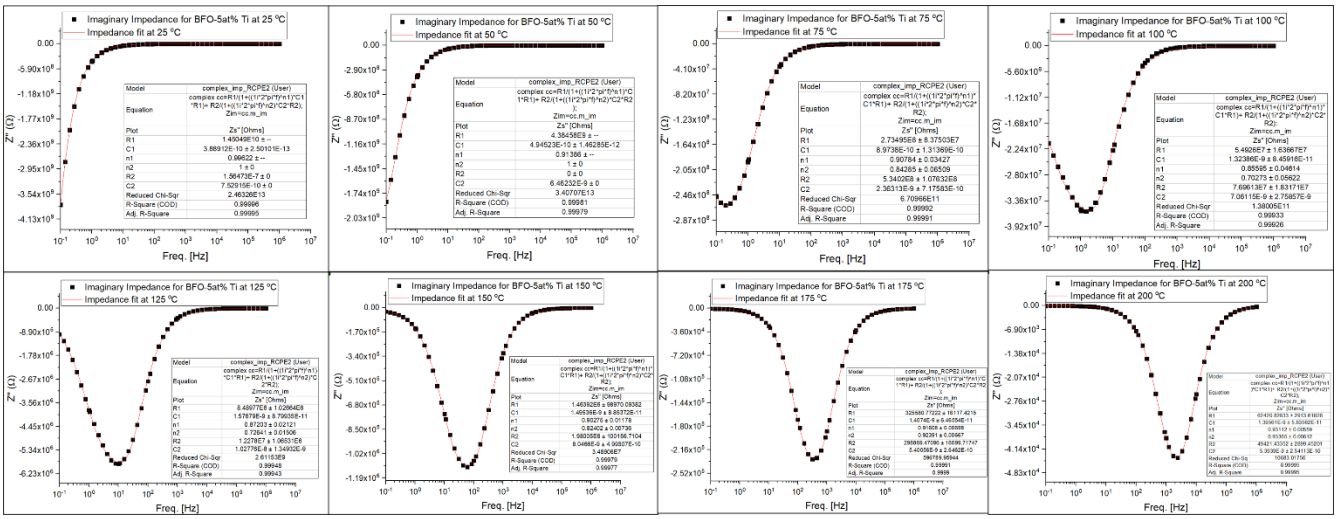

Cobalt-titanium

0.25-0.25 at% Co-Ti

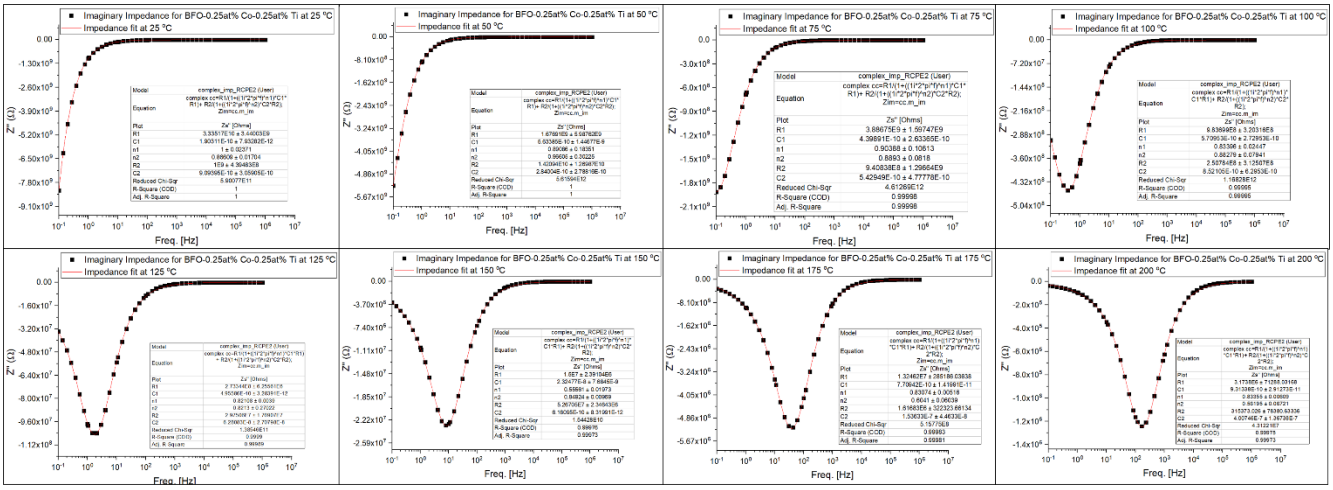

0.25-1 at% Co-Ti

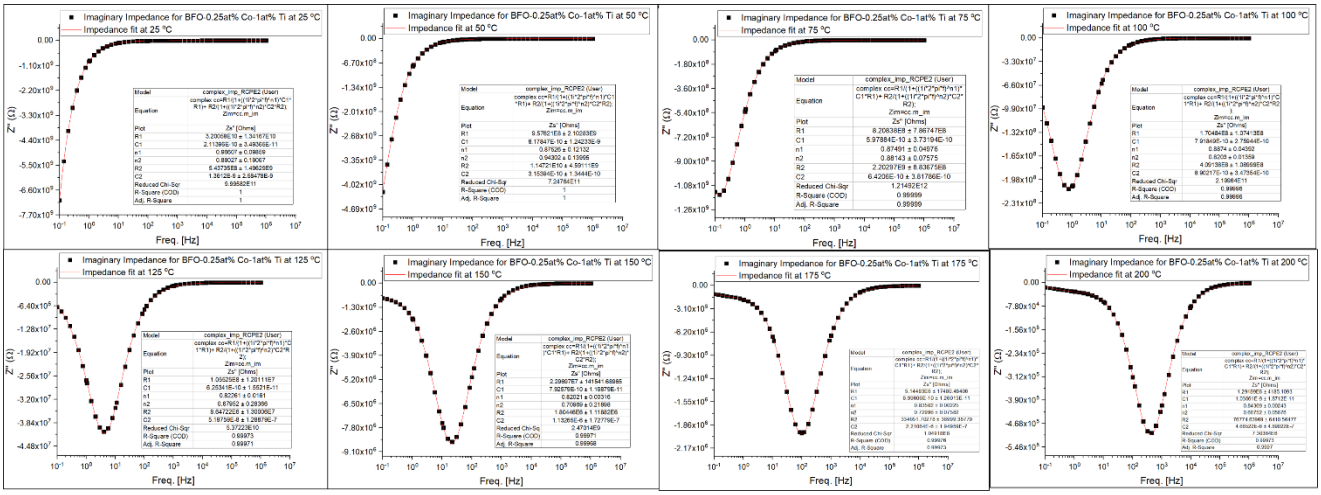

10.2.4 High-resolution EDS data

(No indication of cobalt enrichment or depletion at grain boundaries from the mapping)

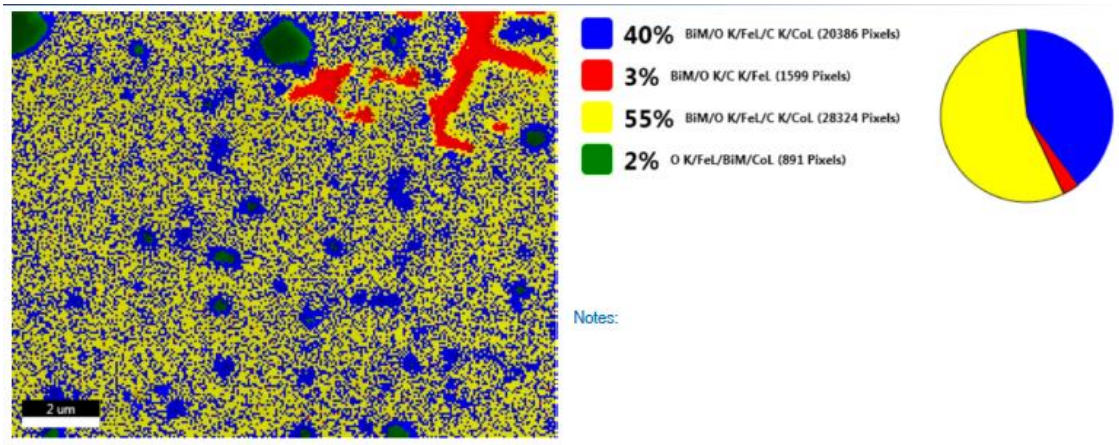

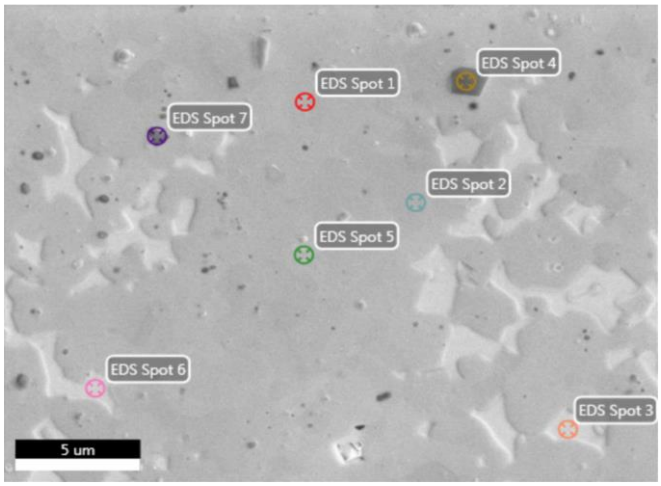

Spot 1

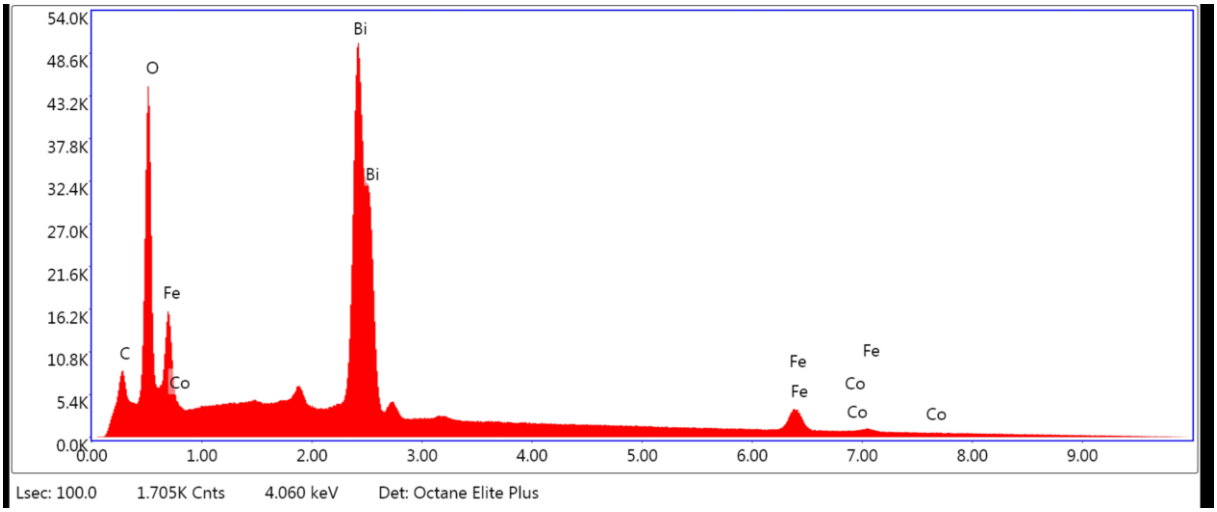

Spot 2

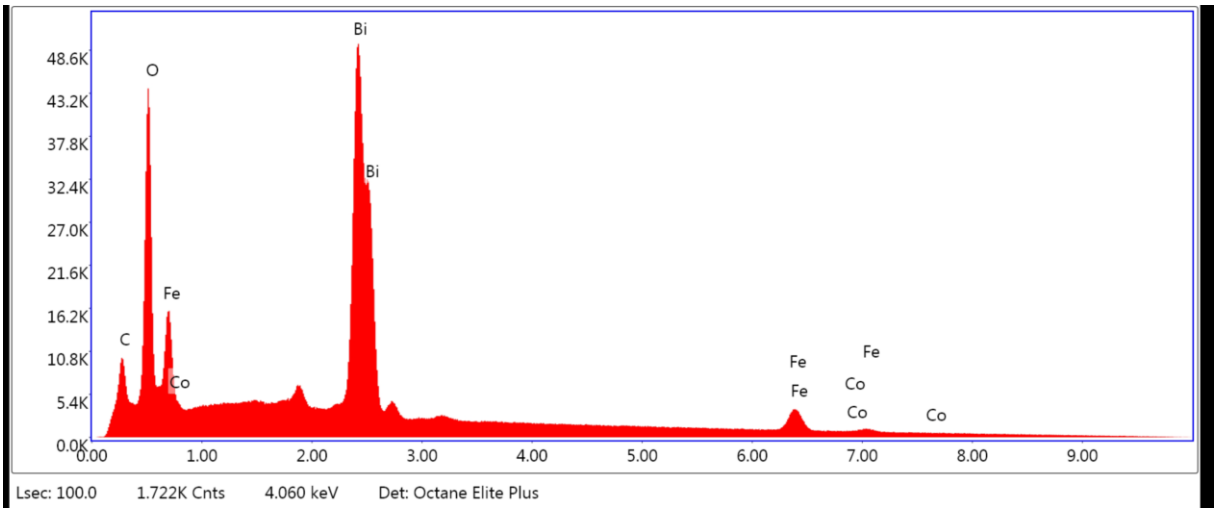

Spot 3

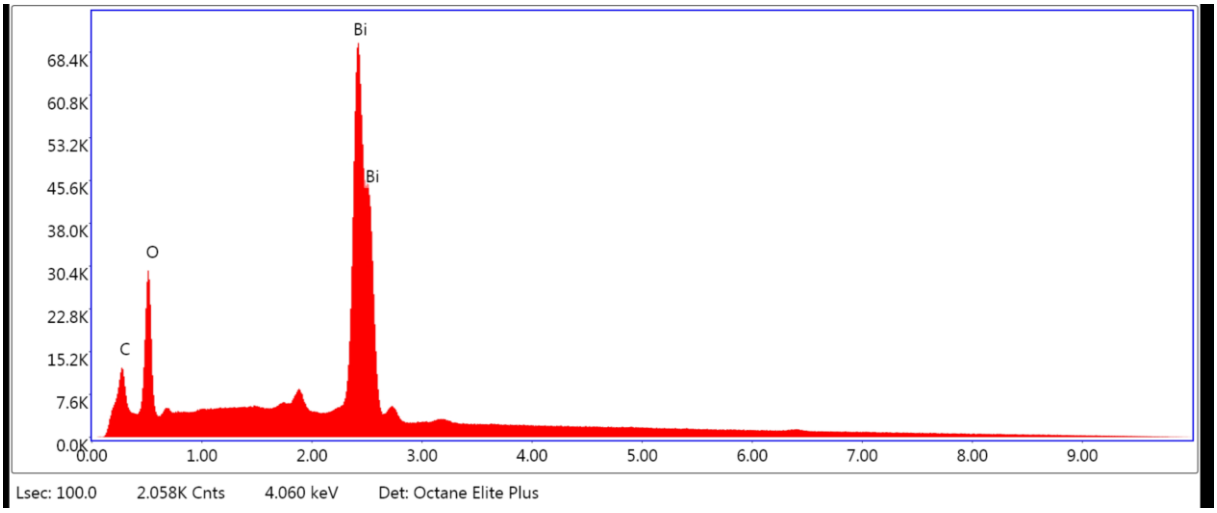

Spot 4

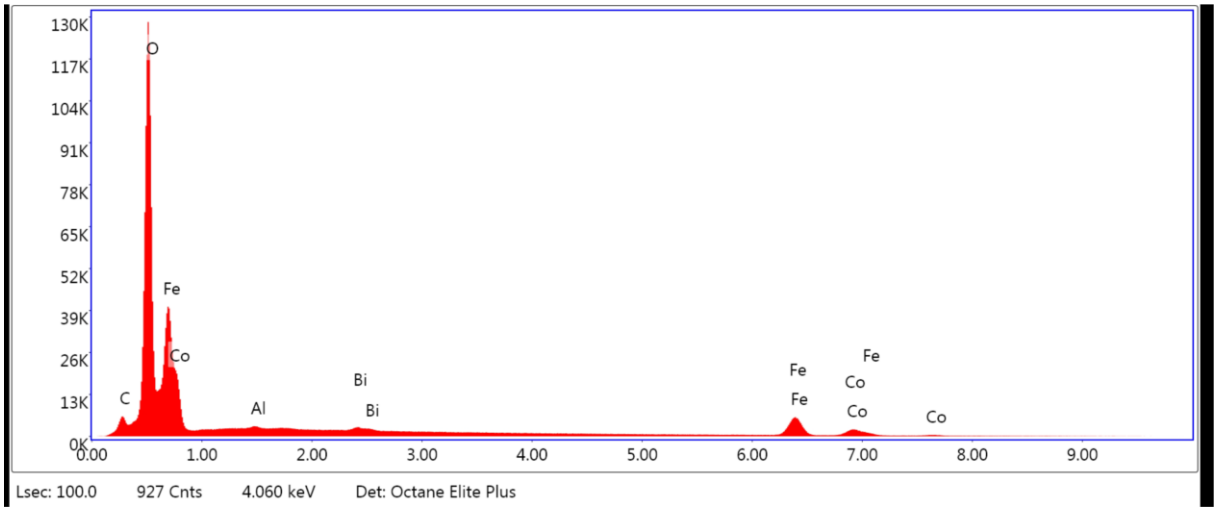

Spot 5

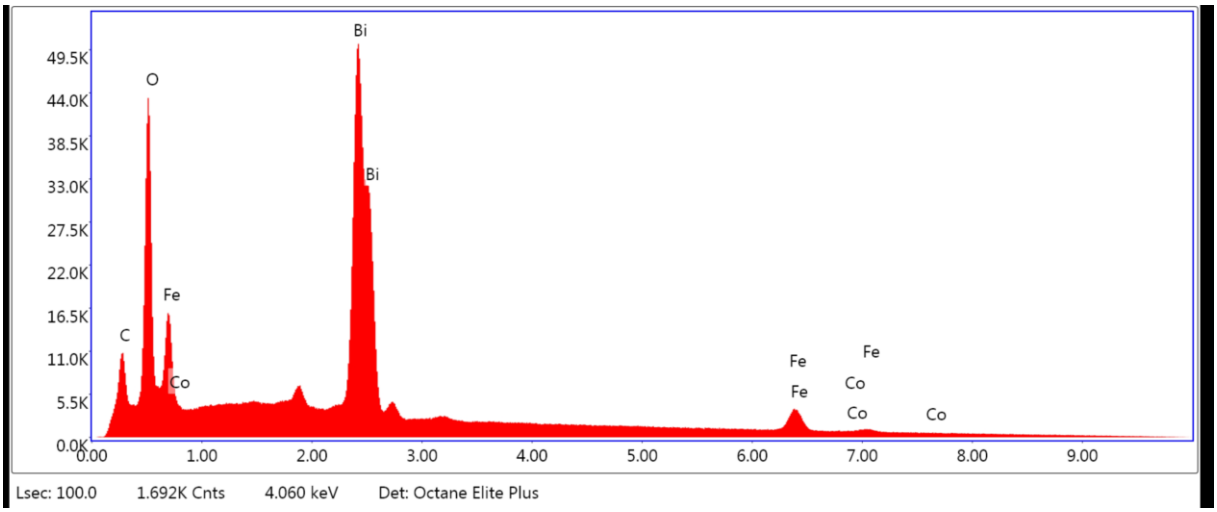
Bi
O
Bi
Fe
C
Co
Fe
Fe
Co
Co
Co
49.5K
44.0K
38.5K
33.0K
27.5K
22.0K
16.5K
11.0K
5.5K
0.0K
0.00
1.00
2.00
3.00
4.00
5.00
6.00
7.00
8.00
9.00
Lsec: 100.0
1.692K Cnts
4.060 keV
Det: Octane Elite Plus

Spot 6

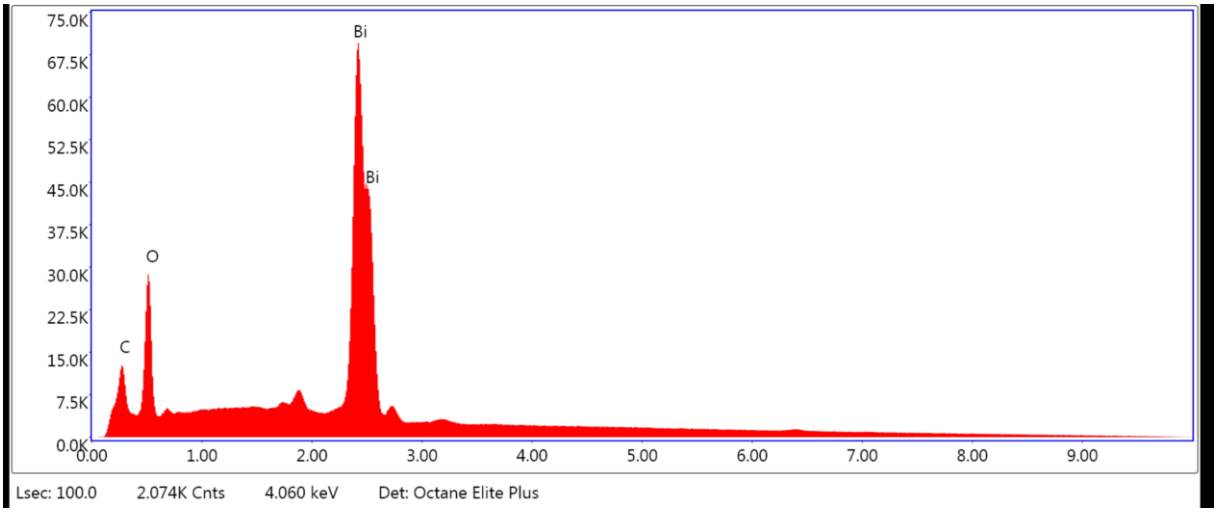
Bi
Bi
O
C
75.0K
67.5K
60.0K
52.5K
45.0K
37.5K
30.0K
22.5K
15.0K
7.5K
0.0K
0.00
1.00
2.00
3.00
4.00
5.00
6.00
7.00
8.00
9.00
Lsec: 100.0
2.074K Cnts
4.060 keV
Det: Octane Elite Plus

Spot 7

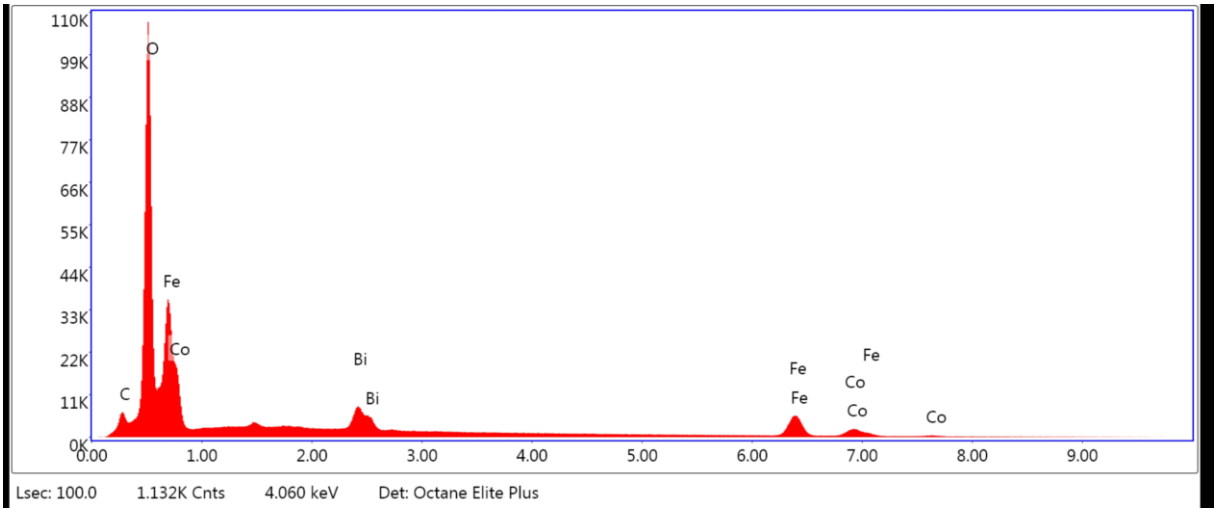
O
Fe
Co
C
Bi
Bi
Fe
Fe
Co
Co
Co
110K
99K
88K
77K
66K
55K
44K
33K
22K
11K
0K
0.00
1.00
2.00
3.00
4.00
5.00
6.00
7.00
8.00
9.00
Lsec: 100.0
1.132K Cnts
4.060 keV
Det: Octane Elite Plus

11. References

1. Groen P. An Introduction to PiezoelectricMaterials and Components An Introduction to Piezoelectric Materials and Components. 2018.
2. Aleai Z. Power Enhancement in Piezoelectric Energy Harvesting. Sch Inf Commun Technol [Internet]. 2016;18–21. Available from: http://www.diva-portal.org/smash/get/diva2:941980/FULLTEXT01.pdf
3. Xu TB. Energy harvesting using piezoelectric materials in aerospace structures. Structural Health Monitoring (SHM) in Aerospace Structures. 2016. 175–212 p.
4. Al Ahmad M, Allataifeh A. Electrical extraction of piezoelectric constants. Heliyon [Internet]. 2018;4(11):e00910. Available from: https://doi.org/10.1016/j.heliyon.2018.e00910
5. Wu J, Fan Z, Xiao D, Zhu J, Wang J. Multiferroic bismuth ferrite-based materials for multifunctional applications: Ceramic bulks, thin films and nanostructures. Prog Mater Sci [Internet]. 2016;84:335–402. Available from: http://dx.doi.org/10.1016/j.pmatsci.2016.09.001
6. Ghosh S, Dasgupta S, Sen A, Maiti HS. Low-temperature synthesis of nanosized bismuth ferrite by soft chemical route. J Am Ceram Soc. 2005;88(5):1349–52.
7. Pooladi M, Sharifi I, Behzadipour M. A review of the structure, magnetic and electrical properties of bismuth ferrite (Bi2Fe4O9). Ceram Int [Internet]. 2020;46(11):18453–63. Available from: https://doi.org/10.1016/j.ceramint.2020.04.241
8. Catalan G, Scott JF. Physics and applications of bismuth ferrite. Adv Mater. 2009;21(24):2463–85.
9. Kumari K, Chakrabarti T, Jana A, Bhattachartjee D, Gupta B, Sarkar SK. Comparative Study on Perovskite Solar Cells based on Titanium, Nickel and Cadmium doped BiFeO3 active material. Opt Mater (Amst) [Internet]. 2018;84(May):681–8. Available from: https://doi.org/10.1016/j.optmat.2018.07.071
10. Shin HW, Son JY. Characteristics of MoS2 monolayer non-volatile memory field effect transistors affected by the ferroelectric properties of BiFeO3 thin films with Pt and SrRuO3 bottom electrodes grown on glass substrates. J Alloys Compd. 2019;792:673–8.
11. Rahman MS, Ghose S, Hong L, Dhungana P, Fahami A, Gatabi JR, et al. Integration of BiFeO3/La0.7Sr0.3MnO3 heterostructures with III-V semiconductors for low-power non-volatile memory and multiferroic field effect transistors. J Mater Chem C. 2016;4(43):10386–94.
12. Palai R, Katiyar RS, Schmid H, Tissot P, Clark SJ, Robertson J, et al. β phase and γ-β metal-insulator transition in multiferroic BiFe O3. Phys Rev B - Condens Matter Mater Phys. 2008;77(1):1–11.
13. Bernardo MS, Jardiel T, Peiteado M, Caballero AC, Villegas M. Reaction pathways in the solid state synthesis of multiferroic BiFeO 3. 2011;31:3047–53.
14. Rojac T, Bencan A, Malic B, Tutuncu G, Jones JL, Daniels JE, et al. BiFeO3 ceramics: Processing, electrical, and electromechanical properties. J Am Ceram Soc.

2014;97(7):1993–2011.

15. Grieshammer S, De Souza RA. Fundamentals of electrical conduction in ceramics [Internet]. Advanced Ceramics for Energy Conversion and Storage. Elsevier Ltd.; 2020. 277–320 p. Available from: http://dx.doi.org/10.1016/B978-0-08-102726-4.00007-7

16. Cai W, Fu C, Gao R, Jiang W, Deng X, Chen G. Photovoltaic enhancement based on improvement of ferroelectric property and band gap in Ti-doped bismuth ferrite thin films. J Alloys Compd [Internet]. 2014;617:240–6. Available from: http://dx.doi.org/10.1016/j.jallcom.2014.08.011

17. Qi X, Dho J, Tomov R, Blamire MG, MacManus-Driscoll JL. Greatly reduced leakage current and conduction mechanism in aliovalent-ion-doped BiFeO3. Appl Phys Lett. 2005;86(6):1–3.

18. Kamba S, Nuzhnyy D, Savinov M, Šebek J, Petzelt J, Prokleška J, et al. Infrared and terahertz studies of polar phonons and magnetodielectric effect in multiferroic BiFe O3 ceramics. Phys Rev B - Condens Matter Mater Phys. 2007;75(2):1–7.

19. Mazumder R, Ghosh S, Mondal P, Bhattacharya D, Dasgupta S, Das N, et al. Particle size dependence of magnetization and phase transition near T N in multiferroic BiFeO3. J Appl Phys. 2006;100(3).

20. Iwamoto M. Maxwell – Wagner Effect Maxwell – Wagner Effect. 2015;1–13.

21. Jonscher AK. Dielectric relaxation in solids. 1999;

22. Kolte J, Salame PH, Daryapurkar AS, Gopalan P. Impedance and AC conductivity study of nano crystalline , fine grained multiferroic bismuth ferrite (BiFeO 3), synthesized by microwave sintering. 2015;097164. Available from: http://dx.doi.org/10.1063/1.4931818

23. Palaimiene E, Macutkevic J, Karpinsky D V, Kholkin AL, Banys J, Palaimiene E, et al. Dielectric investigations of polycrystalline samarium bismuth ferrite ceramic Dielectric investigations of polycrystalline samarium bismuth ferrite ceramic. 2015;012906:1–5.

24. Michel C, Moreau JM, Achenbach GD, Gerson R, James WJ. The atomic structure of BiFeO3. Solid State Commun. 1969;7(9):701–4.

25. Cheng GF, Huang YH, Ge JJ, Lv B, Wu XS. Effects of local structural distortion on magnetization in BiFeO 3 with Pr, Ba co-doping. J Appl Phys. 2012;111(7):93–6.

26. Yuan GL, Or SW, Liu JM, Liu ZG. Structural transformation and ferroelectromagnetic behavior in single-phase Bi1-xNdxFeO3 multiferroic ceramics. Appl Phys Lett. 2006;89(5):1–4.

27. Yuan GL, Or SW, Chan HLW. Structural transformation and ferroelectric-paraelectric phase transition in Bi1-x Lax FeO3 ($x \leq 0$-0.25) multiferroic ceramics. J Phys D Appl Phys. 2007;40(4):1196–200.

28. Lee YH, Wu JM, Lai CH. Influence of la doping in multiferroic properties of BiFe O3 thin films. Appl Phys Lett. 2006;88(4):1–3.

29. Chauhan S, Kumar M, Katyal SC. Band-gap tuning and magnetic properties of heterovalent ions (Ba, Sr and Ca) substituted BiFeO3 nanoparticles. AIP Conf Proc. 2016;1731(May):10–3.

30. Chen X, Wang Y, Yang Y, Yuan G, Yin J, Liu Z. Structure, ferroelectricity and piezoelectricity evolutions of Bi 1-xSm xFeO 3 at various temperatures. Solid State Commun [Internet]. 2012;152(6):497–500. Available from: http://dx.doi.org/10.1016/j.ssc.2011.12.044

31. Yang CH, Kan D, Takeuchi I, Nagarajan V, Seidel J. Doping BiFeO 3: Approaches and enhanced functionality. Phys Chem Chem Phys. 2012;14(46):15953–62.

32. Jun YK, Moon WT, Chang CM, Kim HS, Ryu HS, Kim JW, et al. Effects of Nb-doping on electric and magnetic properties in multi-ferroic BiFeO3 ceramics. Solid State Commun. 2005;135(1–2):133–7.

33. Jo SH, Lee SG, Lee SH. Structural and pyroelectric properties of sol-gel derived multiferroic BFO thin films. Mater Res Bull [Internet]. 2012;47(2):409–12. Available from: http://dx.doi.org/10.1016/j.materresbull.2011.11.009

34. Wang Y, Nan CW. Enhanced ferroelectricity in Ti-doped multiferroic BiFeO3 thin films. Appl Phys Lett. 2006;89(5):3–6.

35. Cheng Z, Wang X, Dou S, Kimura H, Ozawa K. Improved ferroelectric properties in multiferroic BiFe O3 thin films through La and Nb codoping. Phys Rev B - Condens Matter Mater Phys. 2008;77(9):1–4.

36. Ahlawat A, Satapathy S, Maan S, Sathe VG, Gupta PK. Correlation of structure and spin-phonon coupling in (La, Nd) doped BiFeO 3 films . J Raman Spectrosc. 2014;45(10):958–62.

37. Ahlawat A, Satapathy S, Sathe VG, Choudhary RJ, Singh MK, Kumar R, et al. Modification in structure of la and Nd co-doped epitaxial BiFeO3 thin films probed by micro Raman spectroscopy. J Raman Spectrosc. 2015;46(7):636–43.

38. Liu F, Ji F, Lin Y, Huang S, Lin X, Yang F. Ferroresistive Diode Currents in Nanometer-Thick Cobalt-Doped BiFeO 3 Films for Memory Applications . ACS Appl Nano Mater. 2020;3(9):8888–96.

39. Makarovic M, Kanas N, Zorko A, Ziberna K, Ursic H, Smabraten DR, et al. Tailoring the electrical conductivity and hardening in BiFeO3 ceramics. J Eur Ceram Soc [Internet]. 2020;40(15):5483–93. Available from: https://doi.org/10.1016/j.jeurceramsoc.2020.06.037

40. Naganuma H, Miura J, Okamura S. Ferroelectric, electrical and magnetic properties of Cr, Mn, Co, Ni, Cu added polycrystalline BiFe O3 films. Appl Phys Lett. 2008;93(5).

41. Ray J, Biswal AK, Acharya S, Ganesan V, Pradhan DK, Vishwakarma PN. Journal of Magnetism and Magnetic Materials Effect of Co substitution on the magnetic properties of BiFeO 3. 2012;324:4084–9.

42. Zhang M, Yang HJ, Li Y, Cao WQ, Fang XY, Yuan J, et al. Cobalt doping of bismuth ferrite for matched dielectric and magnetic loss. Appl Phys Lett. 2019;115(21):0–5.

43. Zhang M, Yang HJ, Li Y, Cao WQ, Fang XY, Yuan J, et al. Cobalt doping of bismuth ferrite for matched dielectric and magnetic loss. Appl Phys Lett. 2019;115(21).

44. Rojac T, Kosec M, Budic B, Setter N, Damjanovic D. Strong ferroelectric domain-wall pinning in BiFeO3 ceramics. J Appl Phys. 2010;108(7).

45. Carl K, Hardtl KH. Electrical After-Effects In Pb(Ti, Zr)O3 Ceramics. Ferroelectrics.

1977;17(1):473–86.

46. Chaodan Z, Jun Y, Duanming Z, Bin Y, Yunyi W, Longhai W, et al. Processing and ferroelectric properties of ti-doped BiFeO3 ceramics. Integr Ferroelectr. 2007;94(1):31–6.

47. Bernardo MS, Jardiel T, Peiteado M, Mompean FJ, Garcia-Hernandez M, Garcia MA, et al. Intrinsic compositional inhomogeneities in bulk Ti-doped BiFeO3: Microstructure development and multiferroic properties. Chem Mater. 2013;25(9):1533–41.

48. Kumar M, Yadav KL. Study of room temperature magnetoelectric coupling in Ti substituted bismuth ferrite system. J Appl Phys. 2006;100(7):1–5.

49. Kothari D, Raghavendra Reddy V, Sathe VG, Gupta A, Banerjee A, Awasthi AM. Raman scattering study of polycrystalline magnetoelectric BiFeO3. J Magn Magn Mater. 2008;320(3–4):548–52.

50. Dai H, Xue R, Chen Z, Li T, Chen J, Xiang H. Effect of Eu, Ti co-doping on the structural and multiferroic properties of BiFeO3 ceramics. Vol. 40, Ceramics International. 2014. p. 15617–22.

51. Rhaman MM, Matin MA, Al Mamun MA, Hussain A, Hossain MN, Das BC, et al. Enhanced electrical conductivity and multiferroic property of cobalt-doped bismuth ferrite nanoparticles. J Mater Sci Mater Electron [Internet]. 2020;31(11):8727–36. Available from: https://doi.org/10.1007/s10854-020-03407-6

52. Rhaman MM, Matin MA, Hossain MN, Khan MNI, Hakim MA, Islam MF. Ferromagnetic, electric, and ferroelectric properties of samarium and cobalt co-doped bismuth ferrite nanoparticles. Vol. 147, Journal of Physics and Chemistry of Solids. 2020.

53. Grupp DE, Goldman AM. Giant piezoelectric effect in strontium titanate at cryogenic temperatures. Science (80-). 1997;276(5311):392–4.

54. Itoh M, Wang R, Inaguma Y, Yamaguchi T, Shan YJ, Nakamura T. Ferroelectricity induced by oxygen isotope exchange in strontium titanate perovskite. Phys Rev Lett. 1999;82(17):3540–3.

55. Ioachim A, Toacsan MI, Banciu MG, Nedelcu L, Dutu A, Antohe S, et al. Transitions of barium strontium titanate ferroelectric ceramics for different strontium content. Thin Solid Films. 2007;515(16 SPEC. ISS.):6289–93.

56. JAFFE H. Piezoelectric Ceramics. J Am Ceram Soc. 1958;41(11):494–8.

57. Cheng J, Eitel R, Cross LE. Lanthanum-Modified (1 – x)(Bi0.8La0.2)(Ga0.05Fe0.95)O3_xPbTiO3 Crystalline Solutions : Novel Morphotropic Phase-Boundary. 2003;2115:2111–5.

58. Damjanovic D. A morphotropic phase boundary system based on polarization rotation and polarization extension. Appl Phys Lett. 2010;97(6):1–4.

59. Ma ZZ, Tian ZM, Li JQ, Wang CH, Huo SX, Duan HN, et al. Enhanced polarization and magnetization in multiferroic (1-x)BiFeO 3-xSrTiO3 solid solution. Solid State Sci. 2011;13(12):2196–200.

60. Ivanova TL, Gagulin V V. Dielectric properties in the microwave range of solid

solutions in the BiFeO3-SrTiO3 system. Ferroelectrics. 2002;265(1):241–6.

61. Makarovic M, Bencan A, Walker J, Malic B, Rojac T. Processing, piezoelectric and ferroelectric properties of (x)BiFeO3-(1-x)SrTiO3 ceramics. J Eur Ceram Soc. 2019;39(13):3693–702.

62. Wang QQ, Wang Z, Liu XQ, Chen XM. Improved structure stability and multiferroic characteristics in CaTiO 3-Modified BiFeO 3ceramics. J Am Ceram Soc. 2012;95(2):670–5.

63. Falguni Bhadala, Lokesh Suthar and MR. Structural , dielectric and thermal properties. 2019;020144(April):0–6.

64. Sreenu G, Alam M, Fasquelle D, Das D. High-frequency dielectric characterization of novel lead-free ferroelectrics. J Mater Sci Mater Electron [Internet]. 2020;31(21):18477–86. Available from: https://doi.org/10.1007/s10854-020-04391-7

65. Matsuo H, Noguchi Y, Miyayama M, Suzuki M, Watanabe A, Sasabe S, et al. Structural and piezoelectric properties of high-density (Bi0.5 K0.5) TiO3 - BiFeO3 ceramics. J Appl Phys. 2010;108(10):1–7.

66. Tuluk AY, Mahon TR, Van Der Zwaag S, Groen P. BiFeO3 synthesis by conventional solid-state reaction. 2019 IEEE Int Symp Appl Ferroelectr ISAF 2019 - Proc. 2019;8–11.

67. Isarakorn D, Sambri A, Janphuang P, Briand D, Gariglio S, Triscone JM, et al. Epitaxial piezoelectric MEMS on silicon. J Micromechanics Microengineering. 2010;20(5).

68. Hall DA. Ferroelectric hysteresis measurement and analysis NPL Report CMMT (A) 152 Ferroelectric Hysteresis Measurement & Analysis University of Manchester. 2014;(February).

69. Dhahri A, Dhahri E, Hlil EK. Electrical conductivity and dielectric behaviour of nanocrystalline La0.6Gd0.1Sr0.3Mn0.75Si0.25O3. RSC Adv. 2018;8(17):9103–11.

70. Lanfredi S, Rodrigues ACM. Impedance spectroscopy study of the electrical conductivity and dielectric constant of polycrystalline LiNbO3. J Appl Phys. 1999;86(4):2215–9.

71. Rhaman MM, Matin MA, Hossain MN, Mozahid FA, Hakim MA, Islam MF. Bandgap engineering of cobalt-doped bismuth ferrite nanoparticles for photovoltaic applications. Bull Mater Sci. 2019;42(4):1–6.

72. Bhushan B, Basumallick A, Vasanthacharya NY, Kumar S, Das D. Sr induced modification of structural, optical and magnetic properties in Bi1-xSrxFeO3 (x = 0, 0.01, 0.03, 0.05 and 0.07) multiferroic nanoparticles. Solid State Sci. 2010;12(7):1063–9.

73. Folcke E, Le Breton JM, Bréard Y, Maignan A. Mössbauer spectroscopic analysis of Bi1-xSr xFeO3-δ perovskites. Solid State Sci. 2010;12(8):1387–92.

74. Mukherjee A, Basu S, Manna PK, Yusuf SM, Pal M. Giant magnetodielectric and enhanced multiferroic properties of Sm doped bismuth ferrite nanoparticles. J Mater Chem C. 2014;2(29):5885–91.

75. Xu B, Paillard C, Dkhil B, Bellaiche L. Pinched hysteresis loop in defect-free

ferroelectric materials. Phys Rev B. 2016;94(14):1–5.

76. Koops CG. On the dispersion of resistivity and dielectric constant of some semiconductors at audiofrequencies. Phys Rev. 1951;83(1):121–4.

77. Kumar P, Chand P. Structural, electric transport response and electro -strain - Polarization effect in La and Ni modified bismuth ferrite nanostructures. J Alloys Compd [Internet]. 2018;748:504–14. Available from: https://doi.org/10.1016/j.jallcom.2018.03.210

78. Gupta P, Padhee R, Mahapatra PK, Choudhary RNP, Das S. Structural and electrical properties of Bi3TiVO9 ferroelectric ceramics. J Alloys Compd [Internet]. 2018;731(October):1171–80. Available from: https://doi.org/10.1016/j.jallcom.2017.10.123

79. Kumar M, Shankar S, Brijmohan, Kumar S, Thakur OP, Ghosh AK. Impedance spectroscopy and conductivity analysis of multiferroic BFO–BT solid solutions. Phys Lett Sect A Gen At Solid State Phys [Internet]. 2017;381(4):379–86. Available from: http://dx.doi.org/10.1016/j.physleta.2016.11.009